# A Study of
# High Frequency Voltage Effects in
# Medium Voltage Cable Terminations

By

Sarajit Banerjee

A thesis

presented to the University of Waterloo

in fulfillment of the

thesis requirement for the degree of

Master of Applied Science

in

Electrical and Computer Engineering

Waterloo, Ontario, Canada, 2008

I hereby declare that I am the sole author of this thesis. This is a true copy of the thesis, including any required final revisions, as accepted by my examiners.

I understand that my thesis may be made electronically available to the public.

# Abstract

High-power voltage sourced converters (VSC's) are becoming increasingly prevalent in modern transmission systems. These systems primarily use switching schemes generating kHz range harmonics, which may be magnified by one or more system resonances. Despite the high frequency harmonics, VSC systems widely use insulated equipment designed for operation at power frequencies; this includes critical substation components such as medium voltage polymeric cables and terminations. The stress grading systems of non-geometric (compact) cable terminations are susceptible to insulation degradation and eventual flashover failure, under high frequency harmonic stresses. As such, the present work studies high frequency voltage effects in cross-linked polyethylene cable terminations, and their relationship to stress grading (SG) design and material properties. Finite element modeling (FEM) has been used to analyze electric field and resistive heating in termination designs, in response to parametric variations in SG material properties. Experimental studies investigate thermal behaviour in a variety of commercial termination designs, using a high voltage, high frequency test setup developed to replicate conditions of high frequency harmonic resonance in a VSC system.

The study results show that high frequency voltage application increases the electric field, resistive heating, and surface temperature rise, in non-geometric (compact) termination designs using field-dependant stress grading materials. Geometric (stress cone) designs are insensitive to high frequency harmonics; however, they have disadvantages compared to compact designs, making them a less practical long-term solution for high frequency applications. Among non-geometric designs, the field-dependent electrical conductivity $\sigma$ (E), the permittivity $\varepsilon$, and the temperature dependencies of $\sigma$ (E) and $\varepsilon$ strongly influence the termination electrical and thermal behaviour under high frequency stress. Since thermal hotspots in cable termination SG areas may lead to material degradation and eventual failure, recommendations are made for an optimal non-geometric stress grading design, for terminations operating in environments where high frequency harmonics may be present.

# Acknowledgements

# Table of Contents

# List of Tables

# List of Figures

# Chapter 1. Introduction

Prior to the late 1990's, harmonics in the kHz range were rarely present within power transmission systems. Aside from power frequency system equipment operating at 50/60Hz, bulk high voltage direct current (HVDC) systems were entirely based on line-commutated current-sourced converters (CSC's), with either mercury arc valves or thyristors as switching devices. These line-commutated converters produce harmonics in the power frequency range, as switching or 'commutation' occurs only once per cycle [1]. Since the late 1990's, HVDC and flexible alternating current transmission systems (FACTS) have been developed using forced-commutated voltage sourced converters, which commutate using gate turn-off thyristors (GTO's) or insulated gate bipolar transistors (IGBT's). These switches can commutate multiple times in a cycle, with IGBT's using pulse width modulation (PWM) switching at frequencies typically between 1 – 2 kHz [2]. Consequently, kHz range harmonics, with amplitudes depending on system conditions, are commonly generated by these voltage sourced converter (VSC) systems.

Despite the high frequency (HF) harmonics, VSC systems commonly use insulated equipment designed for operation at power frequencies. This includes critical components such as polymeric cables, terminations, and oil-paper insulated transformers, all of which are designed for power frequency. The consequences of this can be insulation failures, either directly from converter initiated high *dv/dt* stresses, or from HF harmonic resonance amplifications. Cable terminations and transformer insulation are two examples of critical components that have failed in VSC installations [3,4].

Medium voltage (MV) underground cables and terminations are used increasingly in VSC system substations for space minimization, reliability, and aesthetic considerations. As such, the effects of HF harmonics on cross-linked polyethylene insulation (XLPE), as well as XLPE cable terminations have been investigated. Combined with field experiences, several studies are concluding that modern non-geometric cable terminations are susceptible to degradation under HF stresses, more than the polymeric insulation itself [5,6,7,8].

1

The following sections will provide an overview, literature review, and background research for this thesis study on high frequency voltage effects in MV cable terminations. The areas discussed will include MV cable terminations, stress-grading composites in cable terminations, HF harmonics in transmission systems, and HF testing techniques.

## 1.1. Medium Voltage Cable Terminations

The definition of a cable termination, according to the IEEE, is a device used for terminating alternating-current power cables, with insulation rated 2.5kV and above. Additionally, various classes of terminations are defined, with Class 1 terminations possessing the following characteristics [9]:

1. Electric stress control for the cable termination.
2. Complete external creepage distance.
3. Sealing against moisture entry.

Class 1A terminations are further classified for use on extruded dielectric insulation systems, such as cross-linked polyethylene (XLPE). Within the scope of this research, Class 1A terminations are exclusively considered, in the medium voltage class which is defined as the phase-to-phase operating voltage range of $V_{L-L} = 2.5 - 44$ kV. This range of cable terminations represents the largest application of non-geometric or 'compact' terminations, which are the focus of this thesis. For operating voltages above 44kV, terminations primarily are of the capacitively graded type.

In cable terminations, the predominant engineering considerations are: electric field control, physical and environmental protection, and creepage distance. Installation considerations are primarily termination type (heat-shrink, cold-shrink, or pre-moulded), and field workmanship. Electric field control of terminations is required since the electric stress where the cable semi-conductive screen ends is very high. Without stress grading, the steady-state electric field at the insulation shield gives rise to partial discharges, likely leading to tracking and insulation failure. Using a stress grading material the field concentration can be greatly reduced, which, assuming proper installation, would avoid partial discharge. Among stress grading methods there are a wide variety of designs used, that can generally be classified as geometric (stress-cone) or non-geometric (resistive, capacitive, or resistive-capacitive) methods. These methods are further discussed in Section 1.2.

Physical and environmental protection is provided by enclosing the termination in a material such as moulded ethylene propylene diene monomer (EPDM), ethylene vinyl acetate (EVA), or silicone rubber [10]. For outdoor designs, sheds are incorporated into the outer housing to increase the creepage distance, and reduce the probability of flashover under polluted or wet conditions. Creepage distance requirements affect the length between the cable semi-conductive screen, and the bare conductor terminal pad. This distance must be of sufficient length to minimize leakage current flow from the conductor to grounded shield, and avoid flashover at rated system basic impulse level (BIL).

Current MV termination types can be classified as either heat-shrink, cold-shrink, or pre-moulded. Prior to the 1970's terminations were mainly hand-taped, which involved building up layers of material, to create a geometric method of stress grading. The difficulties with this method were significant installation time and skill level requirements. Pre-moulded terminations using pre-fabricated capacitive stress cones were the next evolution, and these have remained in usage predominantly for HV applications (69 – 500 kV), and specialized MV applications [11]. The disadvantages of this design include larger size, expensive production, and less flexibility in applying to different conductor sizes and insulation thicknesses. However, pre-moulded slip-on type (SOT) terminations have remained for MV designs, although they are more difficult to install than heat-shrink or cold-shrink, and require void-filling compound which may dry out [8].

Heat-shrink and cold-shrink terminations first appeared in the 1970's. Heat-shrink terminations typically consist of a stress grading material applied at the end of the cable screen to control the electrical stress, and an insulating tube positioned and shrunk by heat over the mastic. Cold-shrink terminations typically consist of moulded skirts, stress grading material, and sealing mastics, loaded onto a removable core tube. The termination is installed by positioning over the prepared cable, and removing the core tube. Due to their compactness, lower manufacturing costs, and inter-changeability, heat-shrink and cold-shrink designs using non-geometric SG methods have become the predominant type for modern MV terminations.

## 1.2. Stress Grading in Cable Terminations

Stress grading (SG) material is provided in MV cable terminations to control high electric stresses, existing at the area where the conductor shield is terminated. If no stress grading were applied, partial discharges and consequently degradation of the insulation materials could occur, depending upon the stress level and discharge resistance of the primary dielectric. To illustrate the effect of SG material application, consider Figure 1-1 which shows the 60 Hz potential lines and corresponding electric field (E) plots present at a semi-conductive boundary, with and without typical compact stress grading.
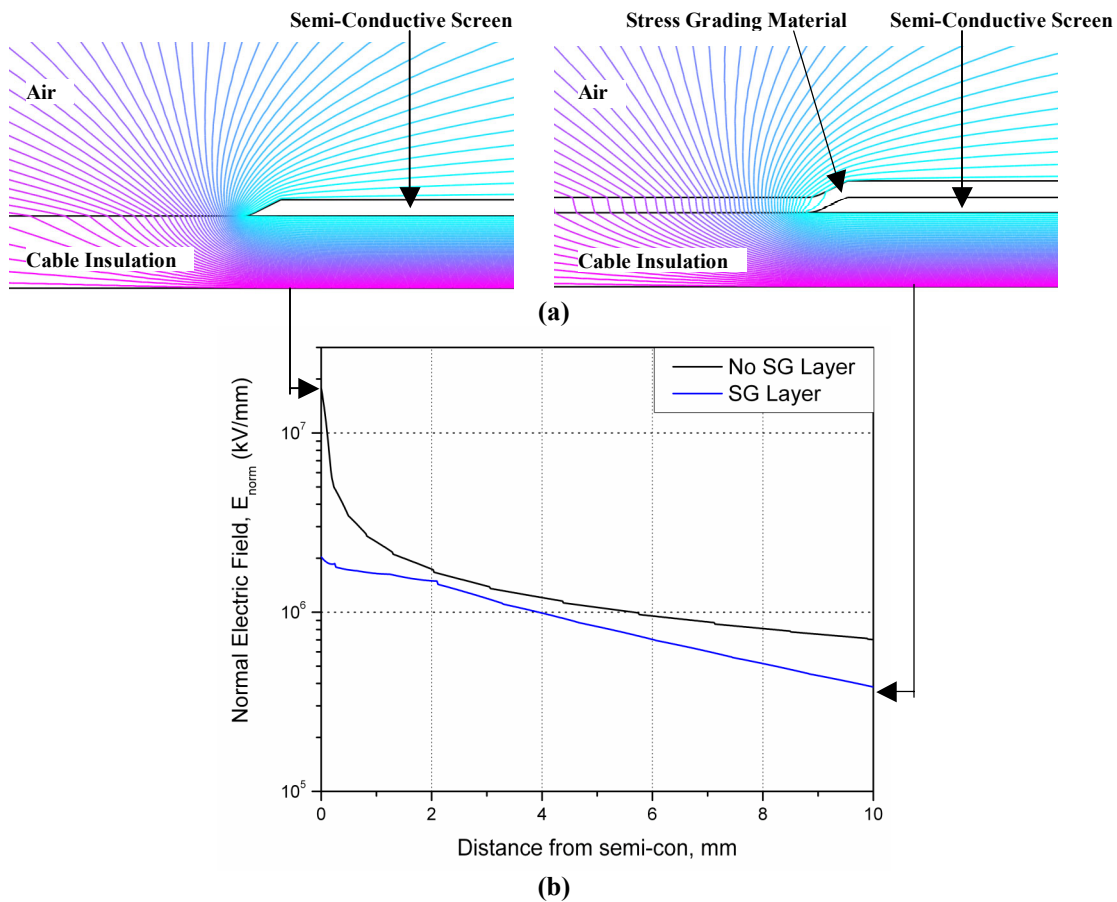


**Figure 1-1:** Example of (a) 60Hz potential lines and (b) Electric field vs. distance from termination semi-con screen, with and without typical compact stress grading.

The need for stress control at the semi-conducting interface arises from the difference in potential between the grounded screen, and the energized high voltage conductor. A schematic to help understand this configuration is shown in Figure 1-2.

4
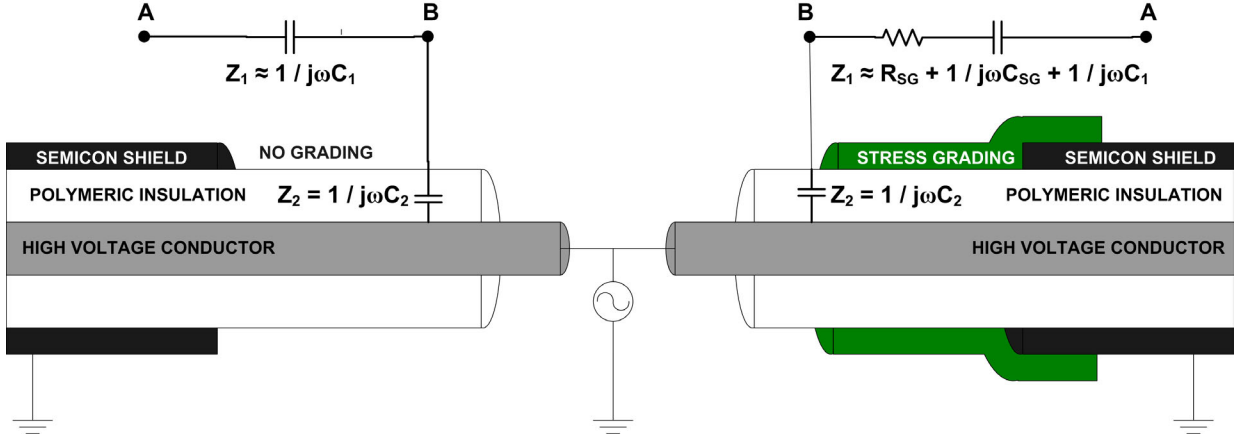
**Figure 1-2:** Illustration of cable termination impedances without and with stress grading.

The potential at point B is determined by voltage division between the impedances $Z_1$ and $Z_2$, where $Z_1$ is the impedance from grounded semi-con to point B, and $Z_2$ is the impedance from point B to the high voltage conductor. Since the cable insulation can be assumed to be purely capacitive ($\sigma = 0$), $Z_2$ can be considered as $1/j\omega C_2$. In the case where no grading material is applied, $Z_1$ can be considered as $1/j\omega C_1$. If $C_1 \ll C_2$ as usually is the case, the voltage drop between A and B, when no SG material is applied, is nearly the total voltage between the grounded semi-con and the HV conductor. This would create an unacceptably high electric field (E) in this region.

When an SG material is applied between the grounded semi-con and Point B as shown in Figure 1-2, the impedance $Z_1$ is essentially changed to an equivalent $R_{SG} + 1/j\omega C_{SG} + 1/j\omega C_1$. The values of $R_{SG}$ and $C_{SG}$ are related to the SG material conductivity $\sigma$ and permittivity $\varepsilon$, respectively. These values determine the classification of the composite, along with the behaviour of $\sigma$ and $\varepsilon$ with respect to applied E. Capacitive stress control materials have higher relative permittivity ($> 30$), whereas conductive or resistive materials have varying levels of conductivity with typically lower permittivity ($< 10$) [7]. Resistive materials are also commonly designed to exhibit linear or non-linear characteristics with respect to applied E, by varying the type of conductive fillers, concentrations, and filler dispersion method. At a minimum, SG materials are developed to control electric stress at the semi-con interface to $< 3$kV/mm, preventing partial discharges from occurring [7]. At a maximum, SG materials can be designed to exhibit 'tuned' grading properties at different frequency ranges, from power frequency to BIL levels. The following sections will provide more insight into these types of composites.

### 1.2.1. Capacitive Stress Grading Methods

Capacitive stress control methods are typically known also as geometric methods, since stress control is often achieved by geometric means. Figure 1-3 shows an example of the electric field distribution when using a geometric stress control cone. This termination design is rarely used for modern MV cable terminations, with the exception of special high-frequency applications [11]. For high voltage terminations rated 115 kV and above however, the geometric design is prevalent.
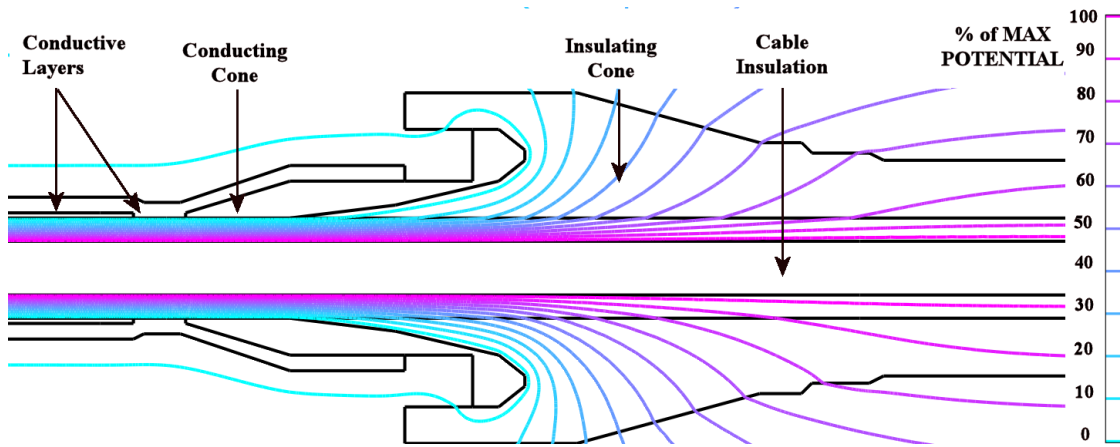


**Figure 1-3:** HV Geometric stress control cone.

Aside from geometric methods, compact capacitive SG coatings are less commonly used since high relative permittivity ($\varepsilon_r > 30$), combined with low conductivity, is difficult to obtain while maintaining necessary thermal or mechanical properties [7]. More commonly, SG composites commercially marketed as 'high-$\varepsilon$' designs derive their high permittivities from the addition of carbon-based powders or metal fillers [12], creating a resistive-capacitive stress grading material.

### 1.2.2. Constant Conductivity Stress Grading Materials

Carbon black (CB) filler is commonly used for creating constant conductivity SG materials. By varying the CB filler content in a host polymer matrix, the conductivity can be modified to control the electrical stress distribution. Composites with CB fillers must however be percolated, in order for the conductivity to remain reasonably constant with electric field [7]. Percolation theory is related to the statistical distribution of the conductive filler in its host polymer matrix. It states that there is a threshold or critical filler concentration beyond which

6

the mixture is electrically conductive, and is said to be percolated. In this case σ is typically high due to ohmic conduction between CB 'pearl chains,' which refers to random clusters of conductive CB particles separated by the insulating matrix [13].

### 1.2.3. Field-Dependent Stress Grading Materials

Field-dependent composites are most often created using particles such as silicon carbide (SiC) or zinc oxide (ZnO) varistor. These materials intrinsically exhibit non-linear behaviour. If the electrical field is lower than a certain threshold, the conductivity is low and behaves linearly; however, when the field increases beyond the threshold, the conductivity increases exponentially. Carbon black composites can also exhibit non-linear field-dependent behaviour, near the percolation threshold. However, this behaviour in CB composites is highly susceptible to compounding and manufacturing processes used, and the non-linearity is often weak and not very reproducible [13,14].

SiC and ZnO varistor powders have fundamental differences. In SiC composites, the conduction mechanisms are dependent only on the particle-to-particle contact properties. Conductivity and switching threshold voltage can thus be modified by changing SiC particle size; however, there is a corresponding increase of low-field conductivity, reducing the insulating ability of the material in these regions. In ZnO composites, the centre of the particle is electrically conductive, but the thin boundaries at particle interfaces are highly insulating. Additionally, these boundary layers behave as micro-varistors, becoming conductive above a defined threshold voltage. These properties allow the stress switching threshold to be adjusted according to requirements, without increasing the low field conductivity of the material. ZnO varistor materials can thus effectively be 'tuned' to compensate for power frequency over-voltages as well as BIL stresses in systems [13].

To analyze some examples of ZnO varistor and SiC powder characteristics, Figure 1-4 from [7] is shown. Figure 1-4 plots the measured electric field versus current density (E-J) characteristics of various composites formed using ZnO varistor, SiC, or combinations of the two. The characteristic curves can be classified according to the expression $J = kE^y$, where k is a constant proportional to the conductivity, and y is a measure of non-linearity. The powders all have ranging non-linearity exponents y, from values less than 5 for powders a to d, to values between 13 and 17 for powders e to h. The values show that composites with

ZnO varistor materials exhibit higher non-linearity than those with SiC. Additionally, the range of curve characteristics in Figure 1-4 shows that both the conductivity and non-linearity of SG materials using ZnO varistor or SiC composites can be modified, by mixing or using different filler concentrations of individual powders. The effects of these characteristics on overall stress grading behaviour are further discussed in Chapters 4 and 5, and selected SG parameters from Figure 1-4 have been used in the thesis simulation studies.
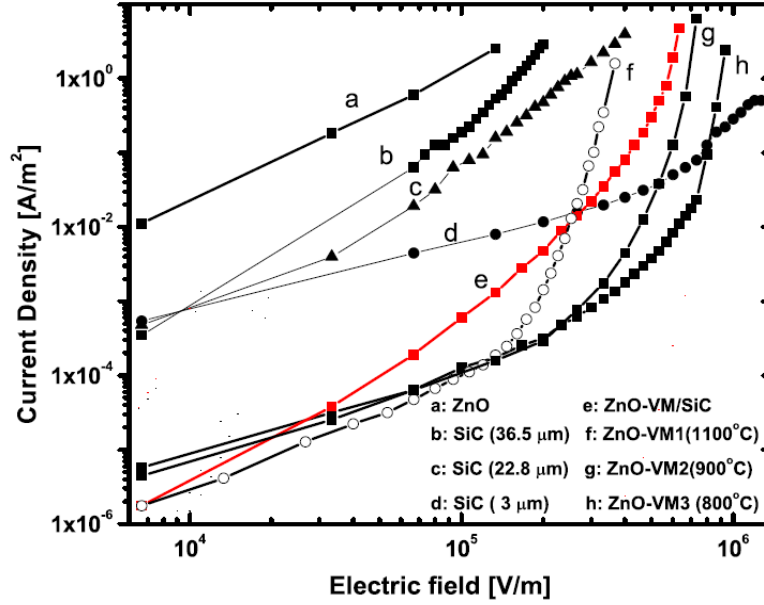


**Figure 1-4:** Measured electric field versus current density (E-J) characteristics for various semi-conductive base powders, used in preparation of stress grading composites [7].

## 1.3. High Frequency Harmonics in Transmission Systems

The following three sections aim to provide an overview of high frequency harmonic generation and their effects on modern transmission systems. Firstly, an overview of VSC's is given, including applications and predominant topologies. Secondly, the problem of high frequency harmonic resonance is discussed; a condition which leads to the most severe harmonic amplitudes in VSC-based transmission systems. Lastly, the effects of HF harmonics on electrical insulation, particularly cable terminations, are reported from a review of existing literature.

### 1.3.1. Voltage Sourced Converters in Transmission Systems

The commercial availability of high-power and high-voltage GTO and IGBT switches has allowed for the operation of VSC's in power transmission schemes. These VSC technology schemes are currently applicable towards low to medium power (less than 400MW) HVDC transmission, and FACTS. HVDC-VSC transmission solutions are commercially known as HVDC Light™ (ABB) or HVDC Plus™ (Siemens), whereas FACTS VSC solutions are known as SVC Light™ (ABB), SVC Plus™ (Siemens), or STATCOM. A primary feature of a VSC in a transmission system is its ability to generate and absorb reactive power using power electronics, thus functioning in an analogous way to a synchronous machine without inertia. In a back-to-back configuration, active power control is possible in addition to reactive power support. Additional benefits include smaller installation sizes compared to building new power frequency or CSC-based bulk HVDC systems, and the ability to connect to weak power frequency networks [15]. For these reasons among others, VSC-based transmission systems are being increasingly implemented, particularly using high frequency IGBT switching. A listing of worldwide VSC-based transmission installations is provided in Appendix A.

For a given DC converter voltage, the stresses upon the system insulation components will vary with the switching frequency of the converter, and the number of intermediate steps (if any) between the two DC terminal voltages. The switching frequency is dependent on the type of switching scheme used to generate the VSC output voltage; these schemes can be classified generally as either square-wave or pulse width modulation (PWM). The number of intermediate steps determines the VSC topology, which can be 2-Level, 3-Level, or multi-level.

Square wave control schemes were prevalent in earlier VSC installations such as Tennessee Valley Authority's STATCOM in 1996 and American Electric Power's UPFC in 1997. In most square-wave control schemes, only one turn-on, turn off operation occurs each device cycle. To obtain a near-sinusoidal output, elaborate waveform summing schemes using phase-shifting transformers or 'interface magnetics' are necessary, creating 12, 24, or 48 pulse output waveforms [2]. Figure 1-5 (a) shows an example of square-wave switched phase-ground outputs following transformer summation, and prior to at the VSC output. VSC's using square-wave control generate lower direct switching harmonics, losses, and

EMI noise than using PWM; however both the DC bus voltage and the width of the pulses must be varied to control the ac output voltage, and the magnetic summation circuitry is large and expensive for high-power transmission.

In PWM control schemes, a carrier-switched waveform is generated, which contains the fundamental frequency component as well as HF harmonics [2]. Multiple pulses are generated per half-cycle, with variable widths controlling the amplitude of the ac output voltage. This allows for improved VSC output amplitude control and reduced lower-order harmonics, at the expense of higher converter losses, HF harmonics, and EMI noise. In PWM the use of HF harmonic filters is also necessary, to reduce the content of kHz range harmonics in the output waveform. Despite these drawbacks, the advantages of improved amplitude control, reduced lower-order harmonics, and elimination of expensive interface magnetics have exclusively favoured PWM over square wave control schemes, in all recent VSC installations by the leading manufacturer [15]. Figure 1-5 (b) shows an example of a PWM switched phase-ground output following high frequency filtering, and prior to at the VSC output.



(a)                                                    (b)
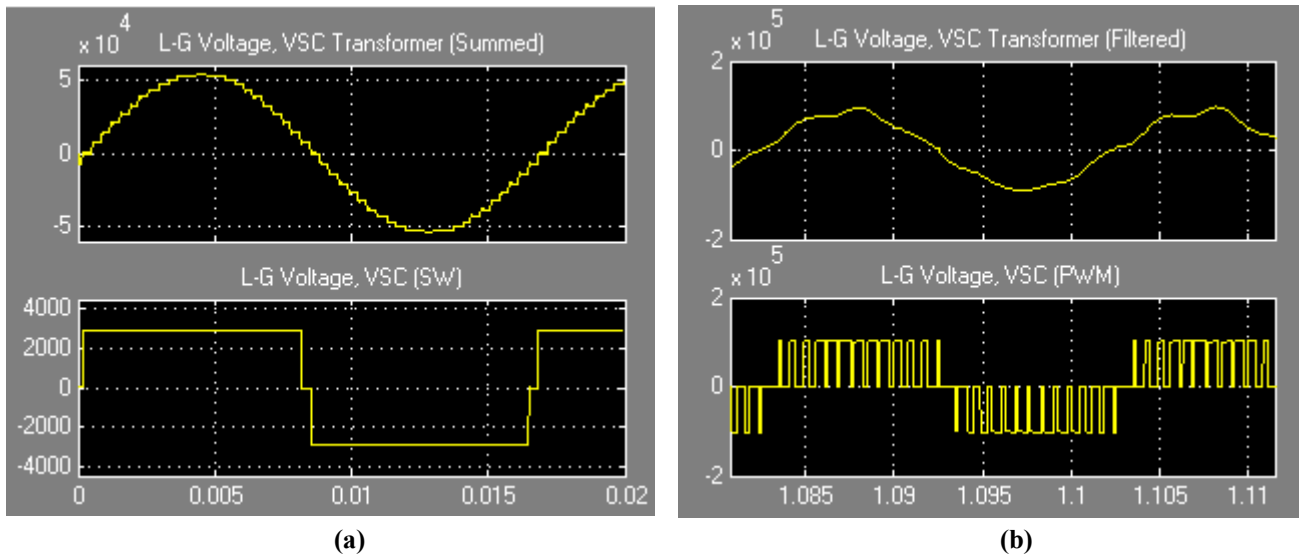
**Figure 1-5:** Typical phase-ground voltage waveforms for: (a) 3-Level VSC using square-wave control, and (b) 3-Level VSC using pulse width modulation (PWM).

The converter topology for a VSC scheme is another critical design factor. A 2-Level VSC is composed of a three-phase six-pulse converter bridge, with each phase leg comprised of two GTO or IGBT switches (either individual or series-built from lower rated switches) [2]. A 3-Level VSC is developed from a three-phase twelve-pulse converter bridge, with

each phase leg comprised of four switches [2]. Figure 1-5 shows VSC output waveforms produced from a 3-Level bridge; the waveforms have three distinctive levels switched from the input DC voltage, with the width of the zero level referred to as the variable conduction angle α. From a harmonic standpoint, the 3-Level has the advantages of lower *dv/dt* rise times than the 2-Level scheme, and also the added control variable α allows for selective harmonic elimination. However, 3-Level systems are more complex and expensive, due the added switching and control requirements over 2-Level systems. 2 or 3-Level topologies have been adopted for the majority of transmission VSC installations listed in Appendix A.

Higher multi-level topologies have been proposed for application in VSC transmission systems, including neutral-point clamped, flying capacitor, and modular multi-level converters [16,17]. To date however, only one VSC transmission project using multi-level converters is currently in development, the Trans Bay Cable listed in Table A-1. The slow adoption is due to higher cost, complexity in valve switching coordination, and DC capacitor voltage balancing considerations [16]. However, the output voltage from a multi-level converter can be designed with lower HF harmonic content and *dv/dt* stresses than all topologies using PWM. In the 'HVDC Plus' modular multi-level converter for example, manufacturer specifications show the output from the VSC as near-sinusoidal, without any magnetic summation or HF filtering.

## 1.3.2. High Frequency Harmonic Resonance

In power system installations using VSC's, it is generally assumed that the output sinusoidal waveforms contain low harmonic distortion, either due to the use of harmonic filters (as when using PWM control), or implementing high-pulse operation (as when using square wave control). However in real systems, it is being recognized that this notion is not always met. Recent experiences from commissioned VSC installations, as well as laboratory results, have shown that harmonic frequencies generated by the VSC's can interact with system resonant points. These resonances due to connected cables, transmission lines, converter transformers, and various other inductive or capacitive components can interact, amplifying harmonic frequency amplitudes to levels much greater than expected. This section analyzes these harmonic resonance phenomena through a review of pertinent literature, as well some preliminary simulation results.

The Eagle Pass Back-to-Back (B2B) VSC installation is a prime example of harmonic resonance occurrence in VSC transmission systems. The Eagle Pass B2B, a joint venture between ABB, EPRI, and AEP, is designed to provide voltage control on its U.S. and Mexican grid sides through reactive power control, as well as control of active power transferred between the grids. The B2B consists of two separate 36-MVA 3-Level VSC's using PWM control, connected to a common DC capacitor link [3]. The schematic of Eagle Pass is shown in Figure 1-6. The MV XLPE cables shown were the focus of insulation failures within the VSC station, due to high frequency stresses.
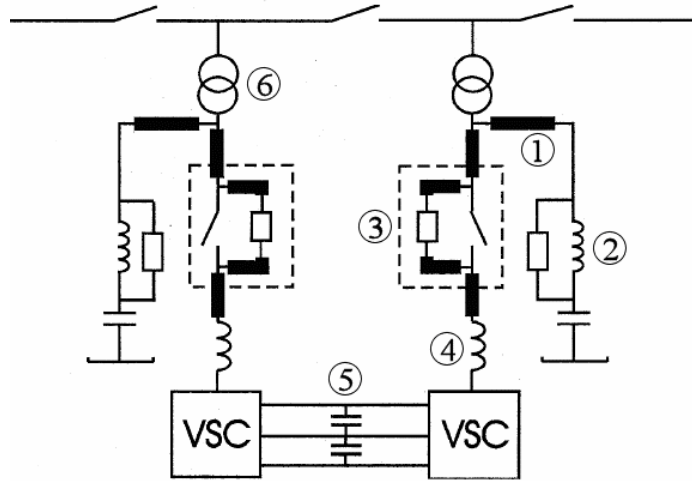


**Figure 1-6:** Schematic for Eagle Pass VSC B2B, showing: 1) MV XLPE cables (bold), 2) HF filters, 3) switchgear with charging resistors, 4) smoothing reactors, 5) DC capacitors, 6) step-up transformers [3].

At Eagle Pass, the on/off switching of the VSC PWM control created harmonics of an order proportional to the switching frequency, 1.26 kHz. In addition to the main harmonics, there was also a spectrum of very high frequency harmonics, resulting from the high *dv/dt* of the 3-Level PWM switching. These HF harmonics were expected, however with low energy and voltage amplitude. Actual measurements during B2B operation were in contrast to this; Figure 1-7 shows a measured distorted phase-ground voltage waveform, and its corresponding Fast Fourier Transform (FFT) spectra at Eagle Pass.
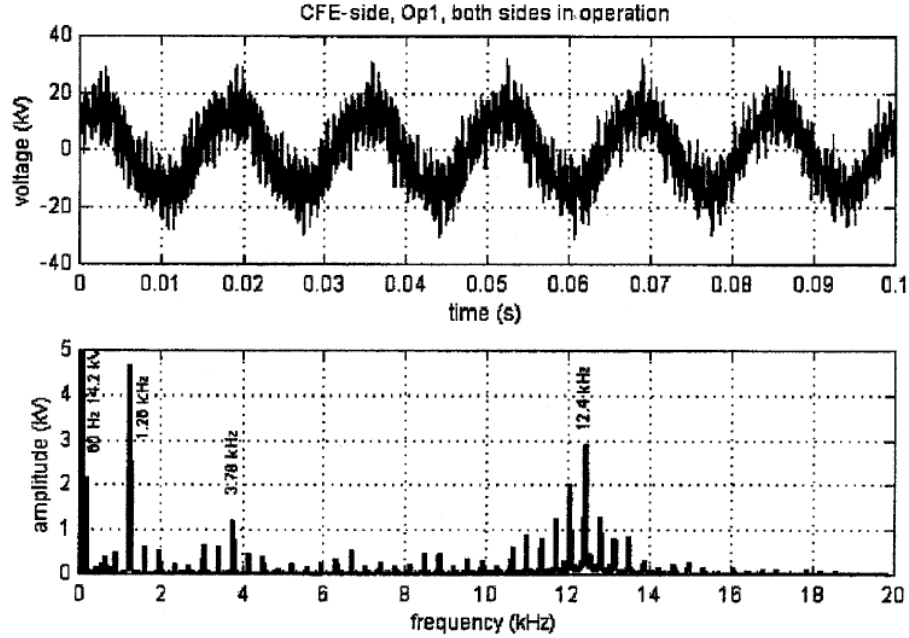
**Figure 1-7:** Phase-ground voltage measured at Eagle Pass during B2B operation, and corresponding FFT [3].

The dominant harmonics at Eagle Pass were 1.26 kHz (21st, IGBT switching frequency), and 12.4 kHz (207th, approximately 10 times IGBT switching frequency). The most unexpected and critical harmonic was the 12.4 kHz, which varied between 13% and 40% of the power frequency voltage, depending on system conditions and B2B operating mode. The designers proposed that the 12.4 kHz harmonic was caused by a system resonance at this point, which was excited by the IGBT switching frequency harmonics in the same range. Their solution was to place active harmonic filters tuned near 12.4 kHz, and replace failing resistive terminations with geometric capacitive designs; these designs were laboratory tested and found to be insensitive to HF harmonics. HF effects on cable terminations used in the Eagle Pass installation will be further discussed in Section 1.3.3.

Temma et al. and the current study analyzed HF harmonic resonance in a VSC-STATCOM, using the sample circuit in Figure 1-8 [18,19]. The 3-Level VSC converter and transformer were connected to the tertiary of a power frequency step-up transformer, with a variable length of HV underground cable. VSC harmonics were reduced by using 'multiple' or phase-shifting transformers, as previously discussed.

13
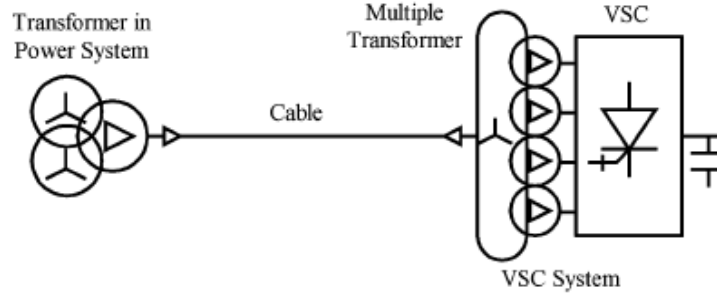
**Figure 1-8:** Sample resonance circuit used for studying VSC-STATCOM harmonic resonance [19].

The studies predicted that when the VSC is connected to a power system that has resonant characteristics, the harmonics it generates could be magnified and have an adverse effect on the power system. Simulated results verified this; for example, Temma calculated phase-ground voltages showing HF harmonics of the 135th order, magnified by nearly 24 times versus normal magnitudes. Results from [19] also showed magnification of harmonic voltages in the 100th order, when the VSC is connected to the system.

If frequency versus impedance (f-Z) behaviour is analyzed from the secondary and primary side of the multiple transformer shown in Figure 1-8, series and parallel resonances of the system can be determined. The f-Z results from [19] are shown in Figure 1-9; a series resonance in the sample circuit is seen at the 108th harmonic when measured from the secondary side, and a parallel resonance at the 90th harmonic when measured from the primary side.



**(a)**                                                   **(b)**
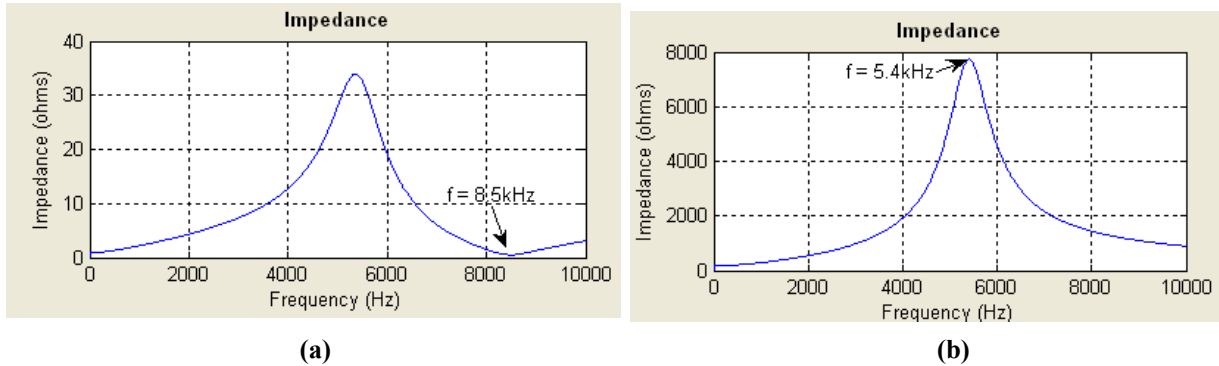
**Figure 1-9:** a) Series resonance point as measured from VSC transformer secondary, with 100m cable, and b) Parallel resonance point as measured from VSC transformer primary, with 100m cable [**19**].

To understand the mechanism of HF harmonic resonance, Figure 1-8 must be interpreted in its resonant circuit form: the delta winding reactance of the power transformer, the leakage inductances of the converter transformer, and the capacitance of the cable. When a small harmonic current is generated from the VSC due to high-frequency operation, an existing

series resonance at this point magnifies the harmonic current by orders of magnitude. Flowing through the converter transformer reactance, this magnified current can create harmonic high voltage across both the power transformer reactance and cable capacitance, if a parallel resonance exists close to the series resonance. This was the case for the 108th and 90th harmonics shown in Figure 1-9, resulting in significant output harmonic distortion.

The results above suggest that if harmonic resonance system studies are conducted prior to installation, VSC schemes could be designed to avoid producing any converter harmonics near resonance points. However, changing system conditions and unpredictable stray capacitances make this idealized approach difficult to achieve [19,20]. Meier's studies on off-shore wind farm VSC systems found that resonance frequencies change depending on altering configurations of the MV collection grid, which vary at minimum during start-up, fault conditions, and maintenance. Additionally, system resonance frequencies were found to decrease with increasing numbers of connected MV grid cables. Similar results were also found in this study, shown in Figure 11 and explained below.
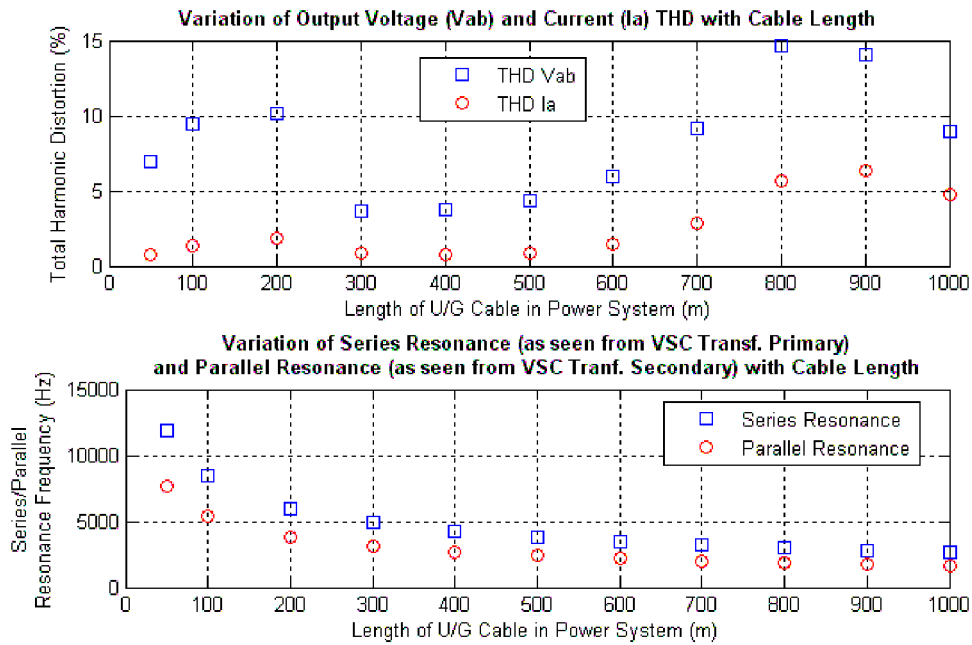


**Figure 1-10:** Variation of VSC output voltage total harmonic distortion (THD), current THD, and system series and parallel resonances with underground cable length [19].

The results above show that increasing the cable length, in a VSC system similar to Figure 1-8, moves the system series and parallel frequencies to lower orders. However, the total harmonic distortion (THD) of the VSC system output depends entirely on whether the

15

VSC produces a harmonic in the vicinity of a system series/parallel resonance frequency. Thus lower order resonances do not necessarily translate to lower output voltage harmonic voltages, and altering system impedances such as cable capacitance is not a viable solution to avoiding harmonic resonances. These results show the difficulties of predicting and designing VSC installations for system resonances. Manufacturers such as ABB are thus researching insulation system modifications within the VSC environment, to withstand the presence of high frequency harmonic amplifications.

### 1.3.3. Effects of High Frequency Harmonics on Cable Terminations

High frequency voltages from VSC's have been shown to have negative effects on power equipment insulation. These adverse effects have been studied mostly for MV motor insulation and stress grading [21,22,23,24]. In light of recent field and laboratory results showing the negative effects of harmonic resonance in VSC systems, research has extended into the stress grading of cable terminations [8,25,26]. This section reviews some of the current research specific to cable terminations.

The first published studies acknowledge the negative effects of HF harmonics on cable terminations, in response to the Eagle Pass failures discussed in Section 1.3.2. Following verification that HF harmonic resonance around 12 kHz was responsible for failures at Eagle Pass, the study authors conducted accelerated ageing tests with resistively graded termination designs used in the installation. When stressed with a high frequency voltage superimposed on power frequency, as the terminations were subject to in the field, the resistive terminations all failed within 470 hours. Geometric type terminations used on the alternate end of the test samples were unaffected. From these tests, it was concluded that the resistively graded terminations were susceptible to failure from the frequency and amplitude of the harmonics [3].

Following the ageing tests, further studies were conducted to determine the fundamental causes of accelerated degradation in failing resistive terminations [8,25]. Ming et al. experimentally analyzed the thermal behaviour of the resistive terminations, using voltage frequencies between $5 - 20$ kHz and amplitudes between $0 - 20$ kV$_{rms}$. Additionally, electrical and thermal field studies using finite element methods (FEM) were also conducted.

Figure 1-11 shows the measured and calculated maximum surface temperatures, with varying applied voltage and frequencies, on a tested resistively-graded non-geometric termination.
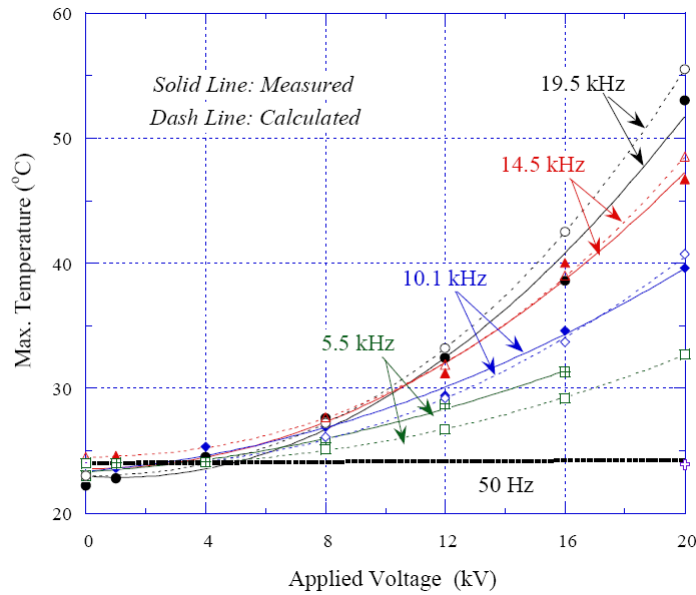


**Figure 1-11:** Maximum surface temperatures on ABB SOT resistive terminations, under power frequency and high frequency voltages [**25**].

The results from Figure 1-11 show the severity of the resistive terminations' surface temperature rise under HF voltages, as opposed to satisfactory performance when subjected to power frequency stress. Ming et al. reasoned that the cause was high ohmic loss in the resistive grading layers, due to increasing SG conductivity with electric field, and increasing leakage current with frequency. The combined effects of higher conductivity and leakage current in the SG material would create local temperature rise, potentially leading to degradation, PD, and failure as was the case for the Eagle Pass resistive terminations.

The most recent study in the area focused on the effect of fast rise-time PWM pulses on termination stress grading [26]. The frequency range studied is much higher than by other researchers or in this thesis, since PWM converter pulse rise-times are in the range of 100ns [22]. A sectionalized SG system was proposed by Espino-Cortés et al. for 'filtering' fast rise-time PWM stresses, with equivalent frequencies in the range of 250 kHz. Although this SG system is highly suitable for variable speed drive systems, it has limitations thus far in withstanding harmonic stresses in the 2 – 20 kHz range, characteristic to VSC transmission resonances. In these situations the separation between HF and PF frequencies is too small, to allow for effective separate grading of the transient and power frequency stresses [7].

17

## 1.4. Review of High Frequency Testing Techniques

In order to investigate the behaviour of electrical insulation under high frequency conditions, it is vital to generate the appropriate experimental test signals. High frequency, high voltage signal generation involves many unconventional principles. Generating high frequency waveforms superimposed on power frequency waveforms, at high voltage, has additional complexities which are rarely described in literature. In this section, a background on both of these applications is provided.

### 1.4.1. High Frequency, High Voltage Signal Generation

To generate a high frequency, high voltage signal, three principles mainly have been applied in the past – these can be classified as the transformer, tesla transformer, and resonance transformer principles. In theory, the easiest method is the transformer principle; in this case, a low voltage HF signal is converted to a high voltage, HF signal before application to a test sample. The main problem however is that an impractically high power is required to supply a capacitive test sample, and the high power HV transformer has to be designed with a HF ferrite core, which has limitations in magnetic flux density for reasonable core sizes [27].

Tesla transformers can be used for the generation of up to 1 million volts, avoid saturation effects by using air coupled cores, and allow resonance frequency ranges between a few kHz to a few MHz [28]. In its original design, the tesla transformer was a doubly tuned resonant circuit with spark gap triggering switches. The disadvantages of using spark gaps were in mechanical wear and lower switching frequencies, resulting in non-constant damped amplitudes in the output voltage [28]. As a substitute, semi-conducting switching elements such as MOSFET's have been used for primary triggering [29]. Further improving on this design, Nagel et al. replaced the three-phase voltage source with a current source, using a variable frequency inverter to excite the secondary resonance circuit [27].

Resonance transformer testing has been used extensively for HV power frequency generation. Although problems exist when applying it to high frequency generation, it can still be a viable, economical alternative when compared to designing a costly tesla transformer. The principle of resonance transformers for HF generation is similar to that for power frequency; under resonance conditions where the inductive reactance is equal to the capacitive reactance, the voltage source has only to deliver the active power to compensate

resistive losses from the transformer and connections. The quality factor 'Q' of the circuit determines the magnitude of voltage multiplication across the test object, in resonance. High frequency resonant transformers require ferrite-cores, but can be designed much smaller than tesla transformers. Disadvantages however include transformer oscillations at specific resonance frequencies due to higher coil capacitances, and also non-linear core effects [29].

## 1.4.2. Power Frequency Superimposed with High Frequency, at High Voltage

Experimenting with power frequency superimposed with high frequency (PF + HF) voltages is fairly recent, stimulated by research into the effects of power electronics switched voltages on insulation. The first reported method involves summing HF and PF waveforms electronically within a low voltage (LV) signal generator, then transforming to the high voltage side. This method has been used to study HF harmonic voltage ageing in XLPE, with small sliced XLPE specimens [5,30]. This test has limitations in application to real capacitive specimens, such as MV cables. Firstly, summing HF and PF signals at low voltages requires rarely available high power LV signal generators, due to the low impedance of the capacitive specimen at high frequencies. Secondly, higher power HV transformers are rarely designed for operation at both power and high frequencies, due to the significant differences between ferrite and iron core designs.

A second reported method for creating PF + HF high voltages is to generate each at low voltage, transform individually to high voltage, and apply them simultaneously to the test object through a network of filtering capacitors and inductors. This method has been applied in high frequency research on cable insulation and terminations [3,6]. Figure 1-12 shows such a circuit, used to investigate terminations failures at the Eagle Pass VSC [3].
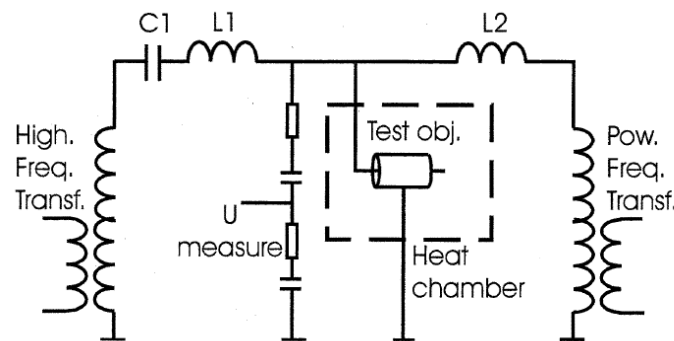


**Figure 1-12:** Example circuit for HF voltage testing of cable terminations; C1 is for low-frequency filtering, L2 is for HF filtering, and L1 is for providing HF resonance [3].

By using separate supplies for the high frequency and power frequency waveforms, it is possible to use HF ferrite core transformers, and standard PF iron core transformers. Additionally, the voltage generation source can be independently chosen for HF and PF waveforms; for example, the HF waveform can be generated using the tesla principle, variable speed generators, or standard HF amplifiers, as in this study. The range of high frequency is limited however, as was the case in [3] where the supply could be varied between 7.5 and 10.6 kHz. The filtering components such as $C_1$, $L_1$, and $L_2$ in Figure 1-12 must also be designed to withstand both HF and PF voltages and currents.

## 1.5. Research Objectives

The discussions above review the knowledge to date on high frequency harmonics in VSC systems, MV cable terminations and their susceptibility to HF harmonics, and testing techniques to replicate HF resonance field conditions. The review shows that although VSC related harmonic problems are being recognized, research in the area of high frequency effects on insulation is still quite limited. This is concerning, especially since the usage of VSC systems for active and reactive control in transmission systems is growing. Furthermore, reports of failures due to HF insulation stresses are rising, with CIGRE reporting recent transformer failures due to HF resonances between HVDC systems and $SF_6$ switchgear [4].

With regards to cable terminations, the solutions proposed thus far have limitations in their applicability. For example, the geometric designs proposed to replace resistively-graded terminations at Eagle Pass are nearly three times costlier, bulkier, more difficult to manufacture, and less interchangeable than the resistively graded types, according to their manufacturer. The manufacturer also considers the geometric designs as a temporary solution until a compact stress grading design is developed, which can withstand HF stresses without failure. Although applicable to motor systems, the sectionalized SG system proposed by Espino-Cortés et al. is also not appropriate for cable terminations operating under VSC harmonic resonance conditions, as discussed in Section 1.3.3.

Ming et al.'s experimental and simulation results showed HF ohmic heating effects on a resistively-graded termination, as well as the HF insusceptibility of a geometric design. However, their simulation studies did not analyze the sensitivity of electric field and resistive

heating to varying SG material properties, to enable optimized non-geometric (compact) termination design for HF applications. Further, experimental studies have not considered variations among alternate termination designs, thermal behaviour under superimposed PF + HF stresses, or heating effects from current circulation. Studying the HF voltage effects on alternative termination designs is vital, since this provides insight into the performance of other available SG materials under HF stresses. This may show that an existing non-geometric solution can avoid HF termination failures, eliminating the need for a geometric design with its previously discussed disadvantages. Current circulation and stress superposition are also important test parameters for investigating cable termination performance in transmission VSC systems, as they are practical field conditions.

Considering the above, the research objectives of this work are as follows:

- Simulate and design an experimental setup to generate PF, HF, and PF + HF voltages for testing MV cable terminations, incorporating effects of current circulation. Setup should also be designed to allow for future long-term accelerated ageing tests, thus with safety and protection provisions for unsupervised ageing.

- Prepare a variety of commercial MV cable terminations for short-term voltage application, current circulation, leakage current, and partial discharge tests. Test terminations under PF, HF, and PF + HF stresses with and without current circulation, to analyze experimental thermal behaviour in stress grading areas under pseudo-field conditions.

- Conduct finite-element simulations using sample SG parameters from [7], to understand basic HF effects in MV cable terminations. Analyze electric field (E), resistive heating (Q), and maximum surface temperature rise ($T_{max}$) in model terminations, designed to match selected commercial designs. Conduct parametric variations in SG material properties, to study corresponding effects on E, Q, and $T_{max.}$

- Compare and analyze experimental and simulation results, and suggest optimal termination stress grading characteristics for application in HF harmonic conditions.

## 1.6. Thesis Outline

The thesis is organized as follows:

- Chapter 1 reviews knowledge to date on high frequency harmonics in VSC systems, cable terminations and their susceptibility to HF harmonics, and testing techniques to replicate HF resonance field conditions.

- Chapter 2 covers preparation of the test samples. This includes six commercial MV terminations, and Haefley$^{TM}$ oil-test terminations which are modified to allow for current circulation tests.

- Chapter 3 discusses the design and development of the experimental resonance setup used for PF, HF, and PF + HF testing with and without current circulation. It also includes results from MATLAB Simulink used to design the experiment, and predict its resonance behaviour.

- Chapter 4 presents results from COMSOL Multiphysics $^{TM}$ field computations, and experimental thermal analyses on test terminations.

- Chapter 5 discusses the experimental and simulation results, and its implications to cable termination design for high frequency harmonic conditions.

- Chapter 6 gives a summary of the research, conclusions, and suggestions for future work in the area of high frequency effects on cable terminations.

# Chapter 2. Materials

Test samples were prepared using a 1m length of $15kV_{L-L}$ XLPE cable, with a dry test termination on one end and a modified Haefely KEV-50 oil-filled termination on the other. This chapter presents characteristics of the XLPE cable, descriptions of the commercial test termination designs T-1 to T-6, and the modified KEV-50 oil termination. Further, to verify installation quality of the test samples, initial PD measurements were conducted on completed test samples according to IEC 61442, for accessories with $V_{L-N} = 8.7kV$ [31].

## 2.1. Sample $15kV_{L-L}$ XLPE Cable

All termination designs in this study, dry or oil type used a suitably sized $15kV_{L-L}$ XLPE cable, typically applied in underground distribution networks. A length of 1m was chosen to limit the capacitance of the test sample under HF stress, and thus the power rating of the experimental setup. Table 2-1 lists the characteristics of the XLPE cable.

**Table 2-1:** Characteristics of $15kV_{L-L}$ XLPE Cable used in preparation of commercial terminations.

| Cable Component | Material/Description | Thickness (mm) | Outer Diameter (mm) |
|---|---|---|---|
| *Conductor* | Stranded Copper, #2/0 AWG | 5.15 | 10.3 |
| *Conductor Shield* | Semi-conducting polymeric layer | 0.6 | 11.5 |
| *Insulation* | Tree-Retardant XLPE | 4.45 | 20.4 |
| *Insulation Shield* | Semi-conducting polymeric layer | 0.7 | 21.8 |
| *Concentric Neutral* | Copper Wires, 20 x #12 AWG | 2 | 25.8 |
| *Outer Jacket* | Polyethylene (PE) | 1.8 | 29.4 |

Prior to installing each termination design on an XLPE cable sample, the cable ends were suitably prepared. The required final dimensions varied depending on termination design, and are shown in Sections 2.2 and 2.3. In all cases, the first step of cable preparation was stripping off the cable outer jacket, and pulling back the concentric neutral wires to form a ground connection. Next a 'semi-con scoring' tool was used to helically cut and remove the

23

insulation semi-conductive shield, without damaging the XLPE insulation. An insulation stripping tool was then used to helically cut the XLPE and conductor shield from the copper conductor. Lastly, the prepared sample was cleaned with isopropyl alcohol to ensure no semi-conductive particles remained on the insulation surface.

## 2.2. Dry Test Terminations

Six different types of commercial MV terminations were tested in this study, representing a vast range of designs; this includes: geometric capacitive (T-2), slip-over (T-1), cold-shrink (T-3 to T-5), and heat-shrink (T-6) termination types. Capacitive, resistive, and resistive-capacitive SG methods were represented among the designs, however exact conductivity and permittivity material characteristics were not known in most cases. The number, thickness, and length of SG layers also varied among the designs, as visible from Figures 2-1 to 2-6. Table 2-2 summarizes some of the characteristics of termination designs T-1 to T-6.

**Table 2-2:** Summary of applicable characteristics, for commercial dry test terminations.

| Termination | Installation Type | Voltage Class $V_{L-G}/V_{L-L}$ $(V_{L-L,MAX})$ | Test Qualifications | Stress Grading Characteristics |
|---|---|---|---|---|
| T-1 | Slipover | 12/20 (24) | CENELEC HD 628.1, 629.1 | Non-linear resistive, high-permittivity (resistive-capacitive). |
| T-2 | Stress Cone | 12/20 (24) | CENELEC HD 629.1, IEEE-48 | Capacitive geometric stress cone, same permittivity as XLPE ($\varepsilon_r \approx 2.3$). |
| T-3 | Cold-Shrink | 9.5/15 (16) | HN-CC-650, IEEE-48 | High-permittivity, conductivity not known. |
| T-4 | Cold-Shrink | 9.5/15 (16) | IEEE-48 | 2- Layer - Outer: high permittivity stress control tube ($\varepsilon_r = 22$), Inner: high-permittivity stress control compound ($\varepsilon_r = 25$). |
| T-5 | Cold-Shrink | 9.5/15 (16) | CENELEC HD 629.1, IEEE-48 | Non-linear resistive metal-oxide, permittivity $\varepsilon_r = 7$ to 10. |
| T-6 | Heat-Shrink | 9.5/15 (16) | CENELEC HD 629.1, IEEE-48 | 2-Layer - Outer: Non-linear resistive metal-oxide, permittivity $\varepsilon_r = 7 - 10$, Inner: Unknown stress control material. |

### 2.2.1. Design T-1

A cross-section of termination design T-1 is shown in Figure 2-1. This design is installed by applying silicone compound to the insulation surface, and then sliding the pre-moulded termination over the prepared XLPE cable. Additional void-filling silicone compound is applied at the semi-con screen cutback. The SG material within termination T-1 is pre-moulded within the slipover termination, and is specified by the manufacturer as having high-permittivity and non-linear conductivity. As such, the SG method can be classified as resistive-capacitive.

### 2.2.2. Design T-2

Termination T-2 is shown in Figure 2-2. This termination uses a pre-fabricated capacitive stress cone, slid over the XLPE cable using silicone compound. The stress cone has a dielectric constant of the same magnitude as the cable insulation, in the range of $\varepsilon_r = 2.3$. The semi-conductive grounded screen of the cable is extended to the base of the stress cone, through the application of an external conductive pad. Conductive material pre-moulded into the stress cone base further extends the grounded pad, geometrically 'deflecting' the equipotential lines of the XLPE cable as shown in Figure 1-3. T-2 is the only design that is recommended specifically for conditions where high voltage, kHz range harmonics are present [11].

### 2.2.3. Design T-3

Figure 2-3 shows termination design T-3. This termination is of cold-shrink design, with the SG layer and outer housing pre-assembled onto a support tube. The termination is installed by positioning the support tube over the XLPE insulation, then pulling out the core and shrinking the termination onto the cable. Similar to T-1, void-filling compound is used at the semi-con cutback to avoid formation of cavities in this high stress region. The SG material for T-3 is specified as high-permittivity; however, the conductivity characteristics are not known.

## 2.2.4. Design T-4

A cross-section of the cold-shrink termination design T-4 is shown in Figure 2-4. Unlike in design T-3, two concentric SG layers are mounted onto the support tube, along with the silicone rubber outer housing. Both inner and outer SG layers shown in Figure 2-4 are reported as having permittivities of 25 and 22, respectively. The material can thus be classified as high-permittivity. However, the conductivity characteristics are not available.

## 2.2.5. Design T-5

Design T-5 shown in Figure 2-5 is a cold-shrink termination similar to T-4. However, T-5 uniquely has its SG layer separately applied to the semi-con cutback. The support tube contains only the outer rubber housing, which is positioned and installed onto the cable following the application of the SG layer. The SG layer in T-5 is specified by its manufacturer as having non-linear conductivity, and permittivity in the range of $\varepsilon_r = 7$ to 10. Additionally, the SG material is known to obtain its non-linear characteristics from the inclusion of metal-oxide varistor (MOV) fillers [32].

## 2.2.6. Design T-6

Figure 2-6 shows termination T-6, the only heat-shrink design used in this study. T-6 has two concentric SG layers, one of which is pre-moulded into the heat-shrinkable outer housing, and the other a strip which is separately applied to the semi-con cutback. The heat-shrink tubing is installed by positioning the tube over the XLPE insulation, and then applying air heated to approximately 400°C. The outer SG layer used in T-6 has similar characteristics to the SG layer in T-5, with $\varepsilon_r$ reported between $7 - 10$ and non-linear conductivity from MOV fillers. The characteristics of the inner SG layer are not known.
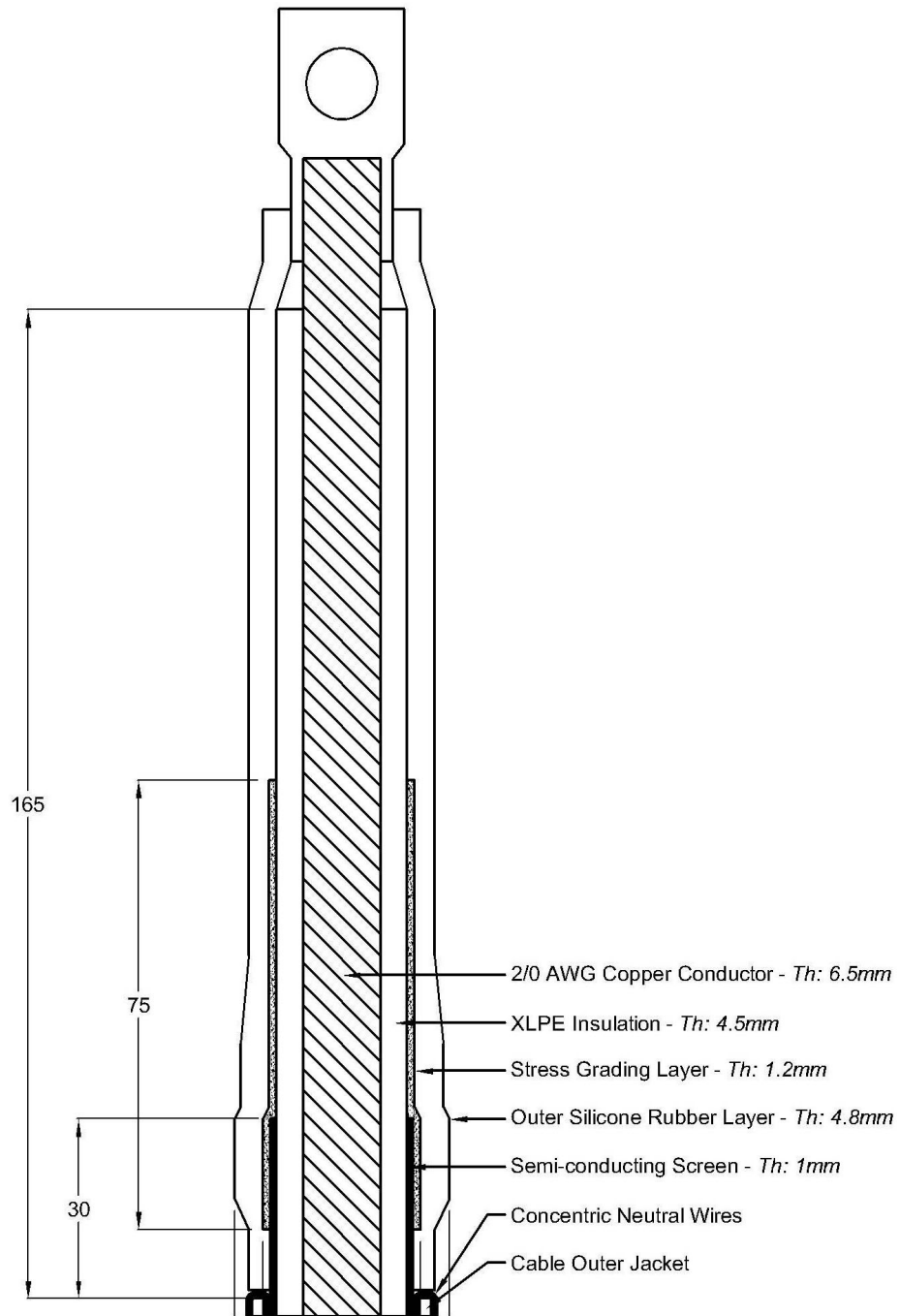
**Figure 2-1:** Cross-sectional view of slip-over type Termination Design T-1, with typical layer thickness (Th).

Labels in figure:
- 2/0 AWG Copper Conductor - *Th: 6.5mm*
- XLPE Insulation - *Th: 4.5mm*
- Stress Grading Layer - *Th: 1.2mm*
- Outer Silicone Rubber Layer - *Th: 4.8mm*
- Semi-conducting Screen - *Th: 1mm*
- Concentric Neutral Wires
- Cable Outer Jacket

Dimensions: 165, 75, 30

220

180

30

Stress Cone - *Min Th: 11mm, Max Th: 24mm*

2/0 AWG Copper Conductor - *Th: 6.5mm*

Conductive Deflector Shield

XLPE Insulation - *Th: 4.5mm*

Conductive Pad - *Th: 3mm*

Semi-conducting Screen - *Th: 1mm*

Concentric Neutral Wires

Cable Outer Jacket

**Figure 2-2** Cross-sectional view of geometric type Termination Design T-2, with typical layer thickness (Th).
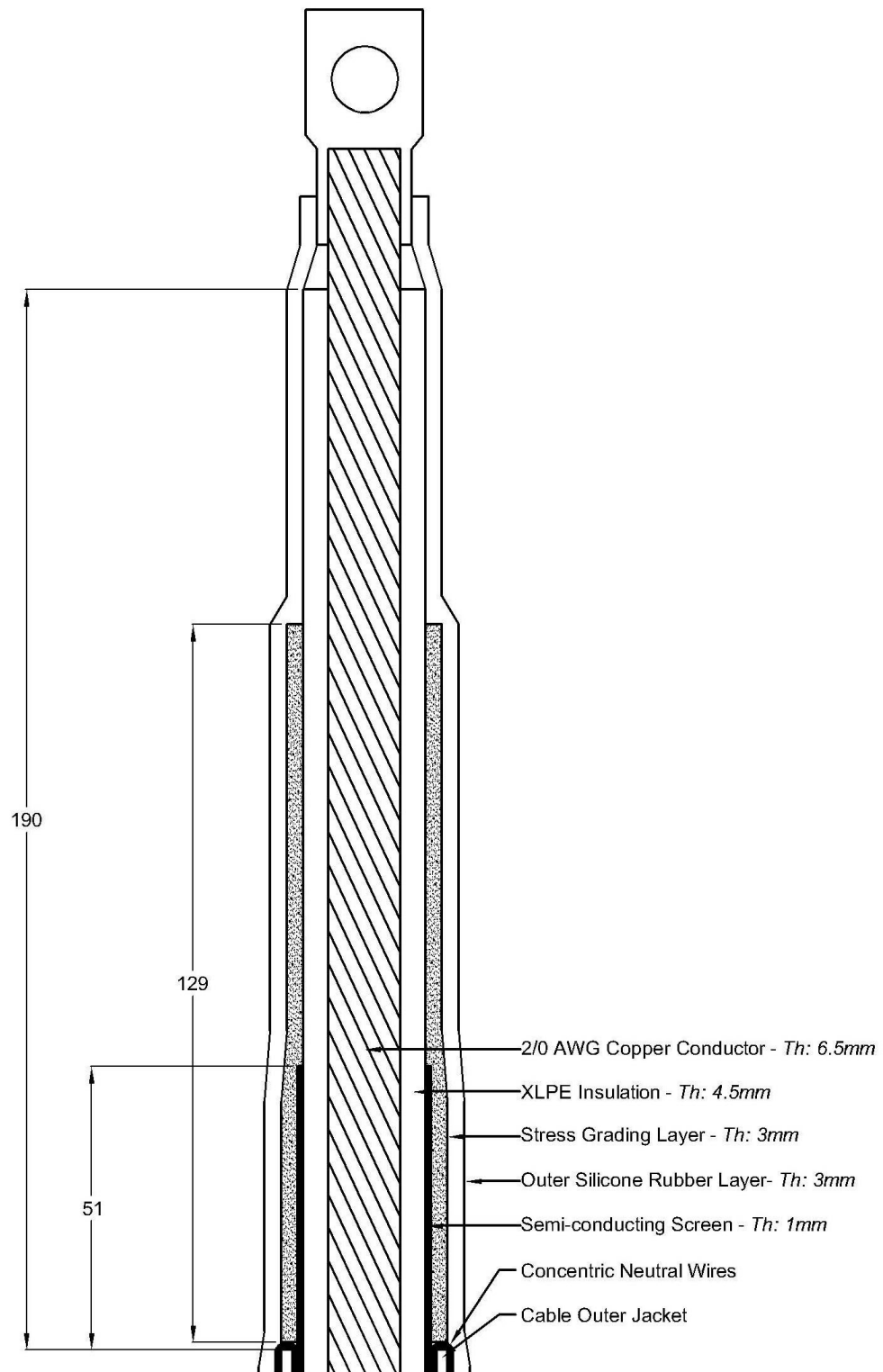
**Figure 2-3** Cross-sectional view of cold-shrink type Termination Design T-3, with typical layer thickness (Th).
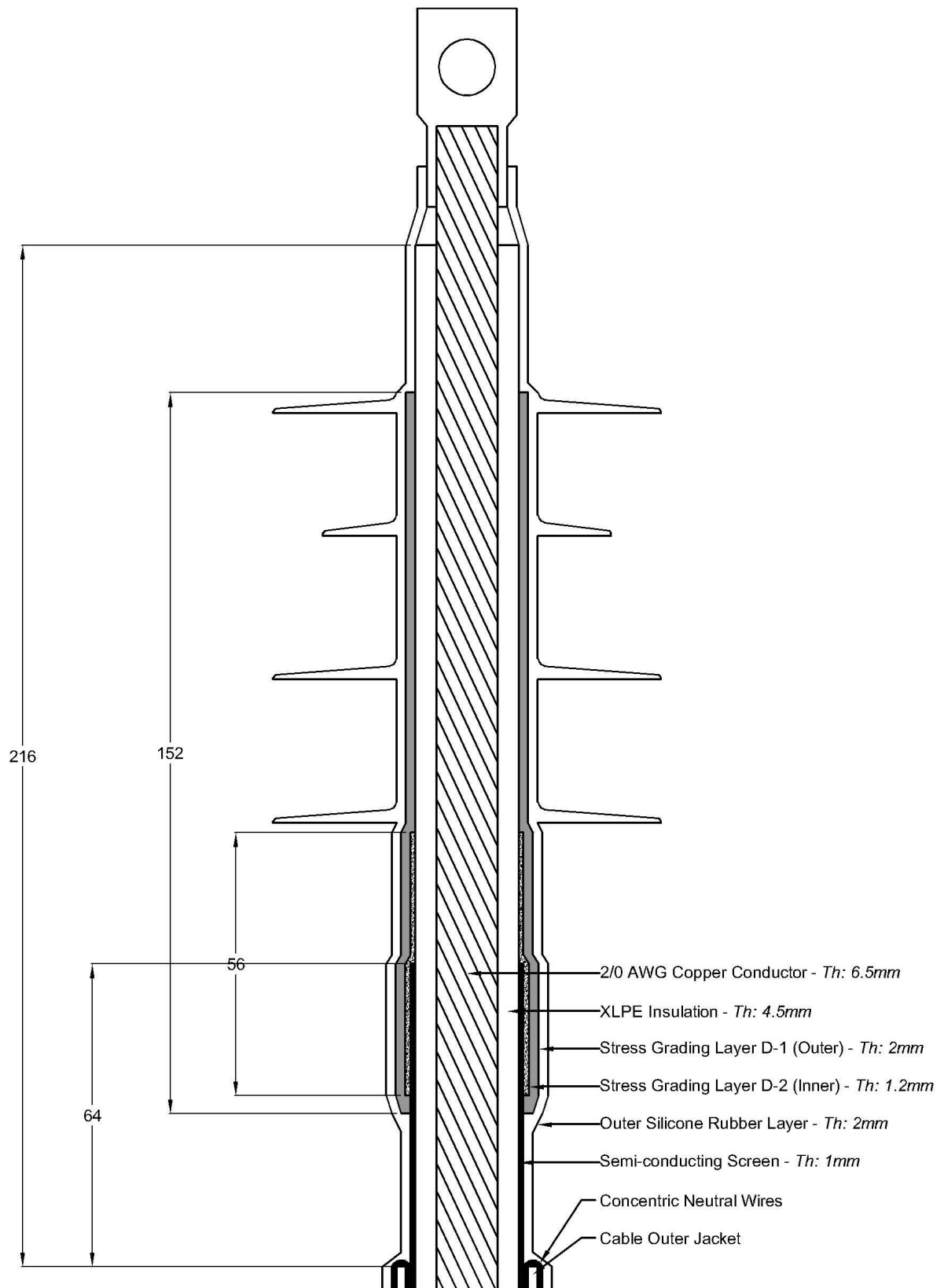
**Figure 2-4** Cross-sectional view of cold shrink type Termination Design T-4, with typical layer thickness (Th).

30
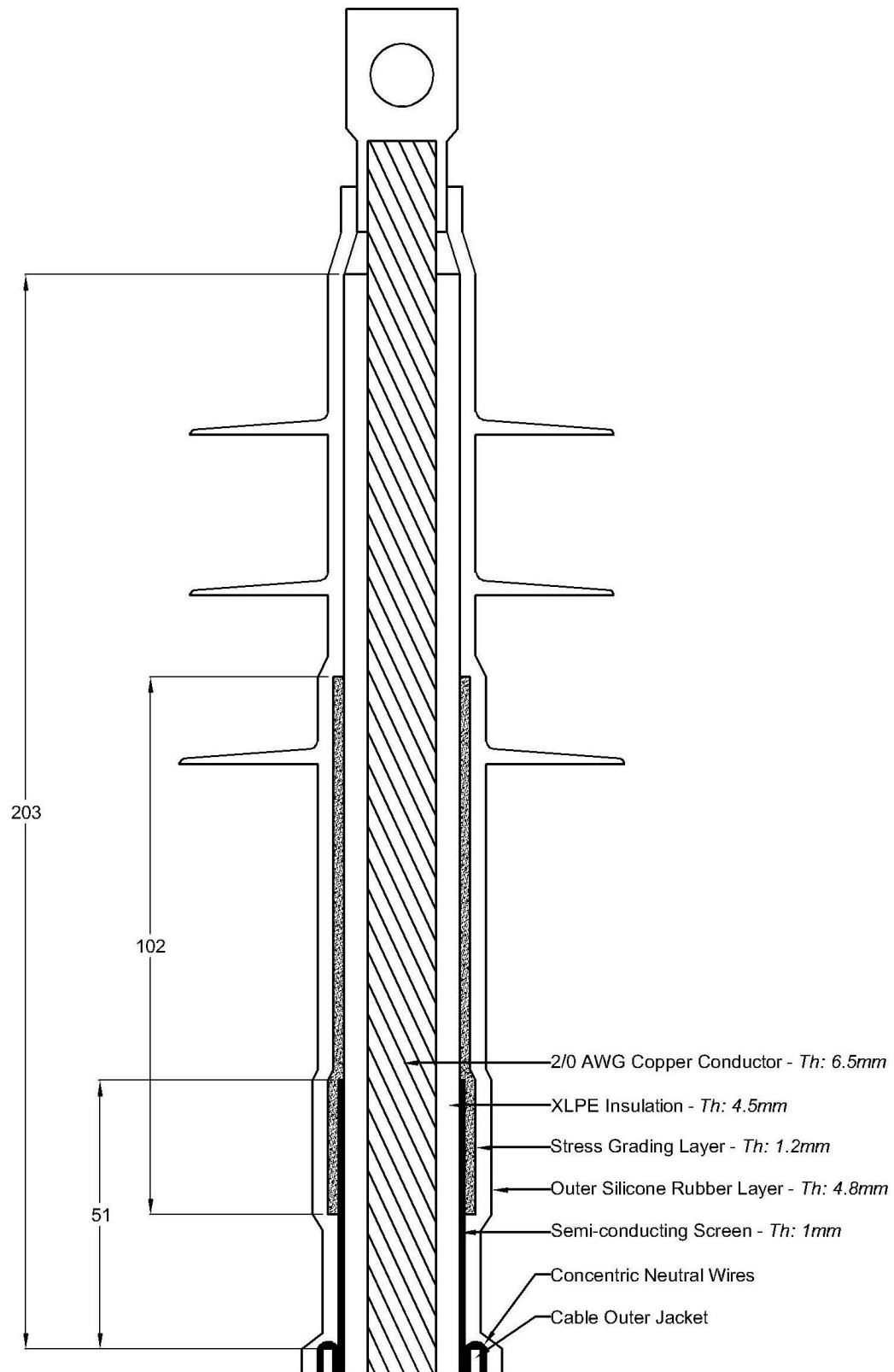
**Figure 2-5:** Cross-sectional view of cold-shrink type Termination Design T-5, with typical layer thickness (Th).

The figure contains the following dimension labels: 203, 102, 51.

The figure contains the following component labels:
- 2/0 AWG Copper Conductor - *Th: 6.5mm*
- XLPE Insulation - *Th: 4.5mm*
- Stress Grading Layer - *Th: 1.2mm*
- Outer Silicone Rubber Layer - *Th: 4.8mm*
- Semi-conducting Screen - *Th: 1mm*
- Concentric Neutral Wires
- Cable Outer Jacket
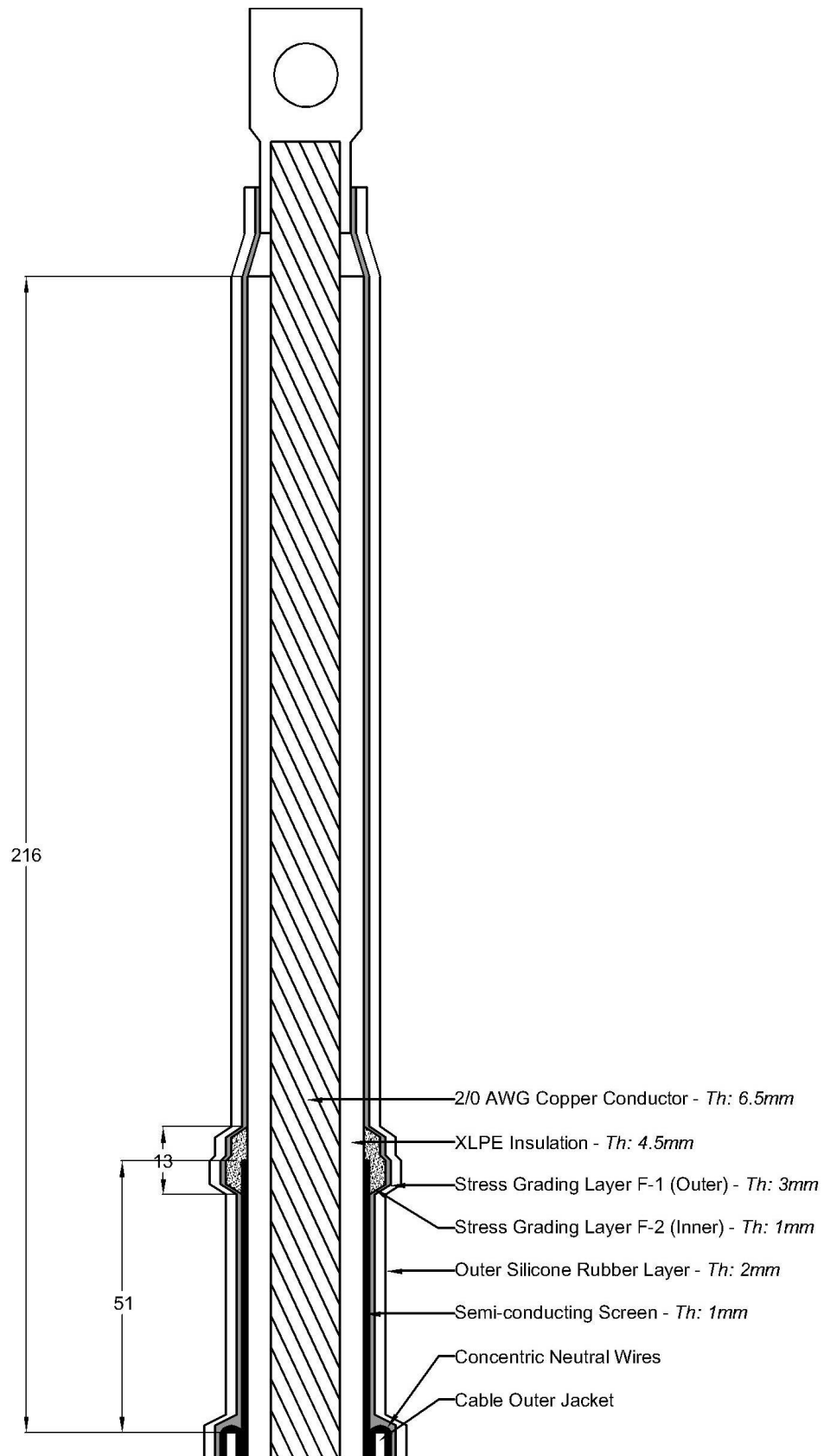
**Figure 2-6** Cross-sectional view of heat-shrink type Termination Design T-6, with typical layer thickness (Th).

32

## 2.3. Oil Terminations

Oil-filled terminations were used as the 'control' termination in each test sample since they have PD levels ≤ 1pC up to $50kV_{rms}$, and are insensitive to HF voltages in the tested frequency range. The HF insensitivity of the KEV-50 allows for long-term accelerated ageing tests on the dry test terminations. When the KEV-50 is used on one end of the test sample, any insulation degradation occurring under HF stress would be localized to the test termination. The ≤1pC levels of the KEV-50 ensured that any PD detected during the initial quality test would be localized to the test termination.

Table 2-3 lists the main characteristics of the KEV-50 oil terminations [33], and Figure 2-7 shows a cross-sectional view of the completed termination with steel supporting structure. Installing the oil termination first required preparation of the $15kV_{L-L}$ XLPE cable, to dimensions specified by its manufacturer. A grounded aluminum electrode was then fitted over the cable semi-con screen, and an aluminum male contact piece was fitted to the cable copper conductor. The prepared cable was finally inserted into the oil-filled insulating tube. The oil supplied with the termination was Shell Diala AX, however Esso's Voltesso 35 was also used as an alternative. The physical and chemical characteristics of both oils are similar, and the main electrical characteristics are as shown in Table 2-4 [34,35].

**Table 2-3:** Relevant characteristics of KEV 50$^{TM}$ oil test termination [33].

| | |
|---|---|
| Rated voltage at 50 / 60Hz (kV) | 50 |
| PD level at rated voltage (pC) | <1 |
| 1 minute withstand test voltage, 50Hz (kV) | 60 |
| Volume of insulating oil per termination (L) | 8 |
| Max. cable diameter over outer screen (mm) | 35 |
| Max. conductor diameter (mm) | 30 |
| Length (mm) | 660 |
| Height (mm) | 595 |
| Width (mm) | 220 |
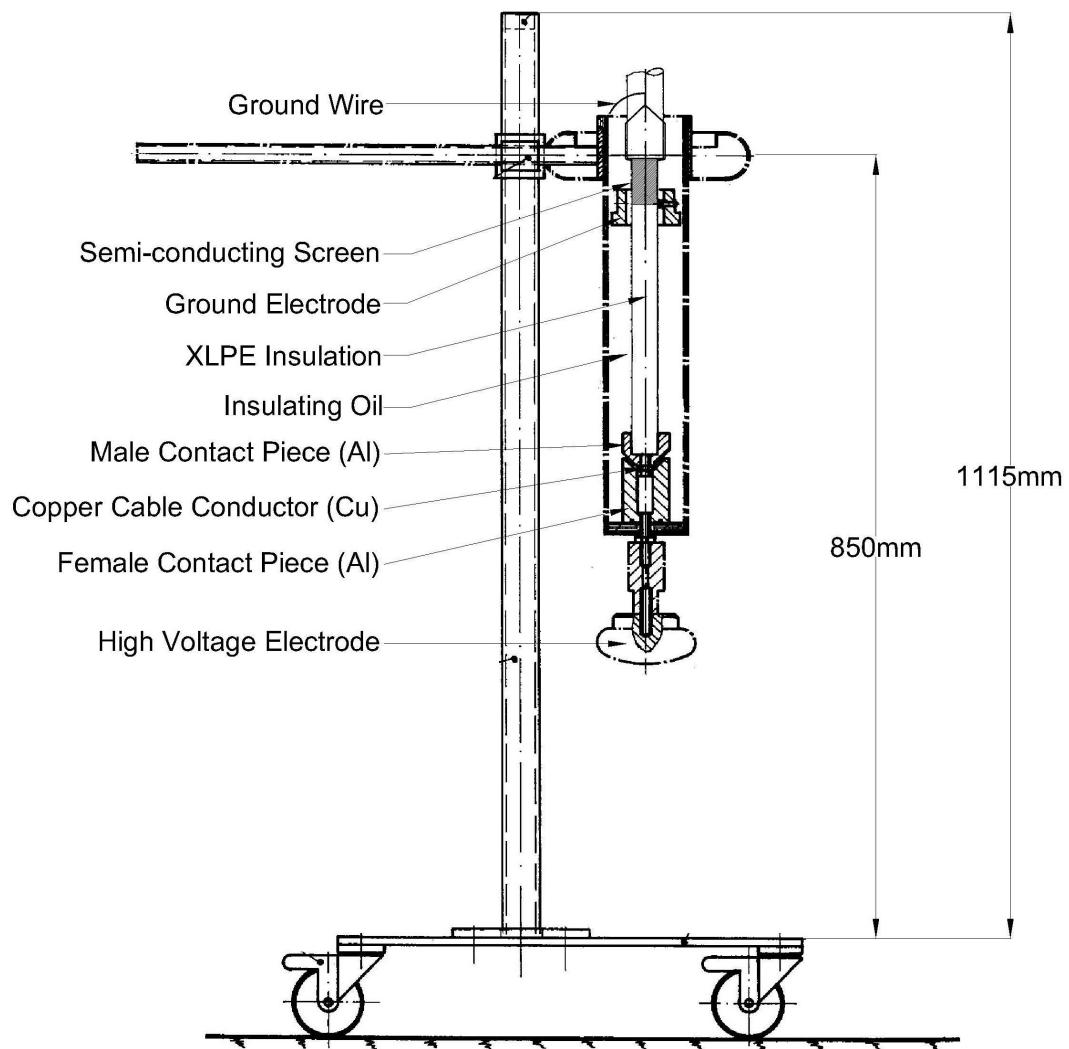
**Figure 2-7:** Cross-section showing main components and dimensions of KEV 50[1M] Oil Test Termination.

**Table 2-4:** Electrical characteristics of insulating liquids used in oil test termination [34,35].

| Electrical Characteristic | Test Standard | Product | |
| --- | --- | --- | --- |
| | | ESSO Voltesso 35 | Shell Diala AX |
| Dielectric Strength, kV, 60 Hz | D1816 (2mm) | 50 | 56 |
| Impulse Strength, kV | D3300 | 225 | 226 |
| Power Factor, 60Hz, % @ 100°C | D924 | 0.07 | 0.04 |
| Gassing Tendency, μl / min | D2300B | +17 | +12 |

34

To study the combined effects of HF stress and elevated conductor temperature, the KEV-50 oil terminations were required to withstand 250 – 300 amps of 60 Hz circulation current. Using the standard design of the KEV-50 however, current circulation through the terminations was not possible to achieve without over-heating the aluminum contact pieces. The cause of over-heating is the contact resistance between the # 2/0 AWG copper conductor and the KEV-50 aluminum contact pieces. Zinc set screws shown in Figure 2-8 (a) form the main surface contacts between the conductor and contact piece, versus typical low-resistance bolted or crimped copper conductor connections. These contacts are sufficient for carrying milliamp leakage currents under voltage testing, but insufficient for 250 – 300 A circulation.

To solve this problem, copper contact pieces were fabricated to increase surface contact between the conductor and the KEV-50 contact piece. The pieces were fitted by first slipping onto the conductor, and then inserting into the KEV-50 contact piece. Additionally, the surface of the copper conductor was filed smooth, to maximize surface contact area at the conductor end. Figure 2-8 (a) shows the original KEV-50 aluminum contact piece, and 2-8 (b) the copper conductor and fabricated contact piece.



(a)                                                         (b)
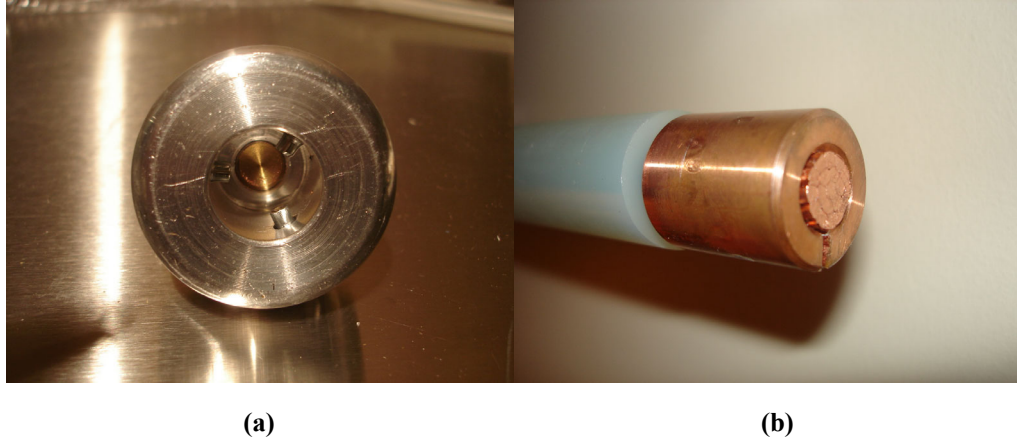
**Figure 2-8:** Images of (a) custom copper contact piece used for eliminating localized heating during current circulation through oil test termination, and (b) standard female contact piece for KEV 50 termination, designed for voltage testing only.

# Chapter 3. Simulations and Experimental Setup

This chapter presents the methodology of finite element modeling (FEM) simulations and high voltage experiments conducted within the scope of this thesis work. The design and development of the experimental setup generating power frequency, high frequency, and superimposed PF + HF voltages for testing MV cable terminations, with circulation current, is also discussed. Finally, an overview of thermal imaging and partial discharge diagnostic measurements is given, as applicable to the high voltage, high frequency experiments.

## 3.1. Simulation Studies of Cable Terminations

### 3.1.1. Problem Formulation

In this study, COMSOL Multiphysics$^{TM}$ was used to compute the electric field, resistive heating, and temperature distributions for model terminations that utilize a variety of field-dependent and field-independent SG materials. The COMSOL FEM method has been applied in previous studies of cable terminations with field-dependent SG materials [7,8]. Furthermore, the FEM application modes, boundary settings, and meshing techniques in this study are based upon experimentally validated simulations by Espino-Cortés et al. [7].

Electromagnetic simulations using FEM solve partial differential equations in discretized domains, based upon Maxwell's unified electromagnetic theory [36]. The cable termination geometry in this FEM model is represented as subdomains of conductor, dielectrics (air, termination housing, and XLPE), semi-conductive screen, and stress grading material layer. Electrical conductivity and relative permittivity are assigned as subdomain properties. The SG material conductivity is dependent on the electric field E, as defined by:

$$\sigma(E) = \sigma_0 \exp(\kappa * E) \qquad [3.1]$$

where $\sigma_0$ and $\kappa$ are positive constants obtained from fitting experimental data. Five unique combinations of constants $\sigma_0$ and $\kappa$ from [7] are adopted for this research. Temperature dependencies are not considered, and permittivities are field-independent within each subdomain, in accordance with [7]. SG material permittivities are varied between the range for test termination T-1 to T-6 reported in Table 2-2, at 60 Hz.

Surface temperature distribution in the modeled cable termination is computed in FEM by solving the thermal diffusion equation below, for each subdomain geometry:

$$\Delta \cdot [k\Delta T] + Q = \rho C \frac{\partial T}{\partial t}$$ [3.2]

The heat source Q can be considered as the resistive heat (ohmic loss) under applied sinusoidal voltage, obtained from the electric field computations. The remaining parameters k, C, and ρ are the thermal conductivity, heat capacity, and mass density of the subdomain material, respectively. Within this study, the values of k, C, and ρ are based on measurements from field-dependent SG materials reported in [7].

## 3.1.2. Simulation Procedure

All FEM studies, except simulations on the influence of termination geometry, were conducted on a model using the dimensions of test termination T-4. Sensitivity analysis was conducted for surface electric field, resistive heating, and maximum temperature rise in the model termination, in response to variations in the following parameters:

1. Applied sinusoidal voltage frequency and amplitude.
2. SG material electrical conductivity and permittivity.
3. SG material thermal conductivity.

The conductor voltage was varied between $0.25V_{L-G}$ to $1.5V_{L-G}$, where $V_{L-G} = 8.7kV_{rms}$. The frequency of the applied voltage was set at 60 Hz or 7 kHz, simulating the effects of power frequency and high frequency test voltages, respectively. The voltage and frequency parameters were selected to correspond with experimental test conditions, discussed in Section 3.2.4. Table 3-1 summarizes the range of conductivity constants ($\sigma_0$ and $\kappa$), relative permittivities ($\varepsilon_r$), and thermal conductivities (k) used in the simulations. The five unique combinations of $\sigma_0$ and $\kappa$ selected from [7], along with corresponding $\varepsilon_r$ and k ranges, are herein referred to as simulated SG layers A to E.

**Table 3-1** Electrical conductivity, permittivity, and thermal conductivities of simulated SG materials A to E.

| SG Layer Designation | Conductivity vs. Electric Field Behaviour | Conductivity Parameters | | Relative Permittivity $\varepsilon_r$ | Thermal Conductivity (W/m.K) |
|---|---|---|---|---|---|
| | | $\sigma 0$ [S/m] | $\kappa$ [m/V] | | |
| SG - A | Field-Dependent | 2.7E-11 | 7.54E-06 | 8 and 23 | 0.6 - 1.3 |
| SG - B | Field-Dependent | 1.75E-14 | 1.07E-05 | 8 and 23 | 0.9 |
| SG - C | Field-Dependent | 1.2E-10 | 8.50E-06 | 8 and 23 | 0.9 |
| SG - D | Field-Dependent | 3.00E-11 | 5.00E-06 | 8 and 23 | 0.9 |
| SG - E | Constant | 1.00E-06 | ----- | 8 and 23 | 0.9 |

FEM simulations were also used to evaluate the influence of termination geometry on surface electric field and resistive heating. Three geometry models were used for these studies, representing geometric (stress cone) termination T-2, and non-geometric terminations T-3 and T-4. Figures 3-1 (a), (b), and (c) show the meshed FEM models representing terminations T-2, T-3, and T-4, respectively.
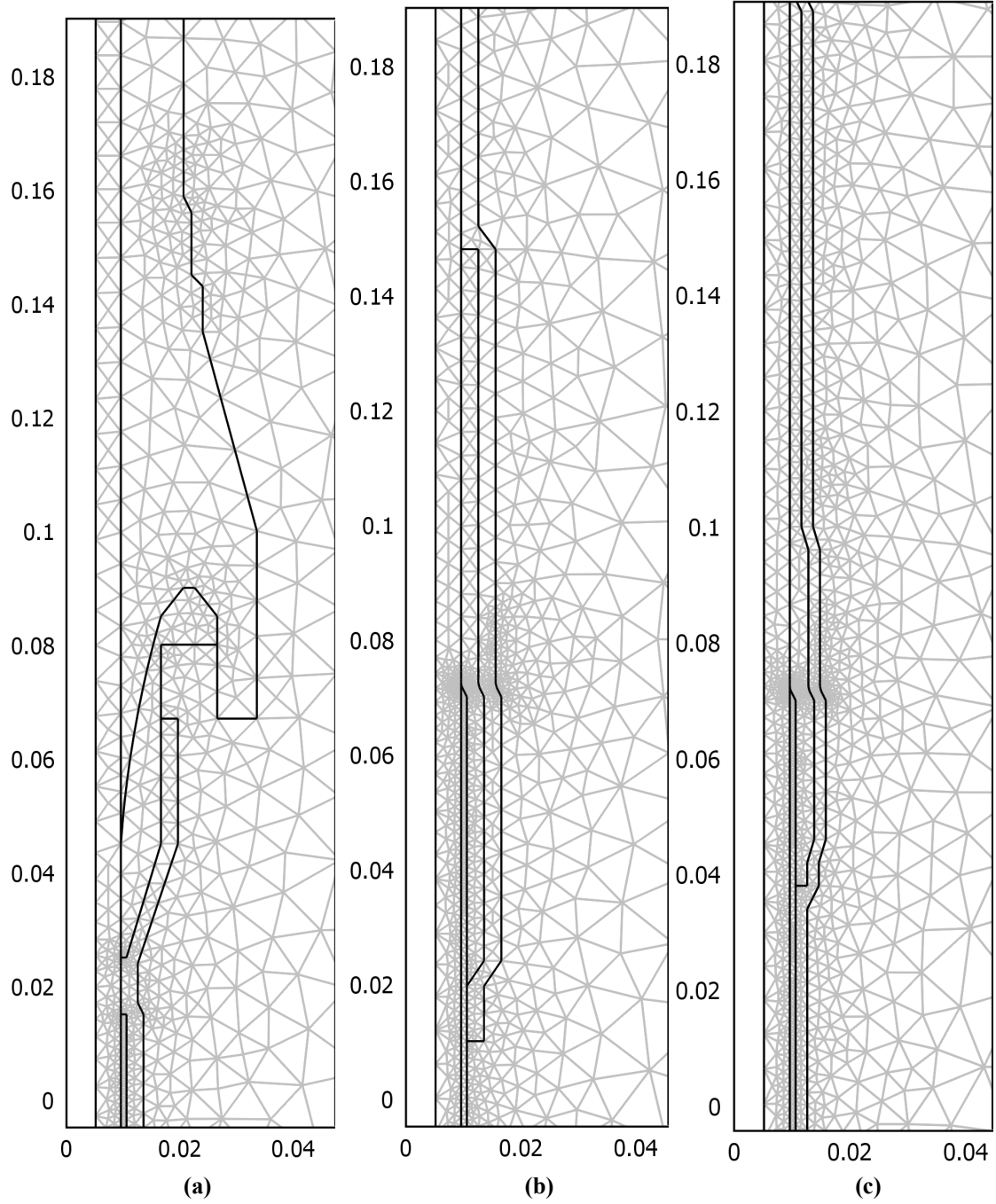
**Figure 3-1:** Meshed FEM models used in study representing test terminations (a) T-2, (b) T-3, and (c) T-4. Dimensions are in millimetres.

## 3.2. Experimental Setup and Procedure

### 3.2.1. Designing Power Frequency and High Frequency Superposition Circuit

To develop the high voltage, experimental power frequency with high frequency superposition circuit, the following primary design goals were first established:

1. Producing PF, HF, and HF + PF superimposed voltage output waveforms, to test termination samples T-1 to T-6 under normal system conditions and those representative of HF harmonic resonance.

2. Creating superimposed waveform with HF component frequency between 5 – 10 kHz, and maximum amplitude reaching 40% of PF peak voltage - these conditions would be similar to field observations described in Section 1.3.2.

3. Maintaining HF voltage harmonics at PF source, and PF voltage harmonics at HF source, below 5% of fundamental values. This would avoid adverse effects on insulation of transformers and power sources.

4. During circuit operation under PF, HF, and PF + HF voltages and currents, keeping circuit components within their design power ratings.

5. Using standard laboratory PF and HF sources and circuit components wherever possible, for economic and practical purposes.

The MATLAB Simulink$^{TM}$ simulation model in Figure 3-2 was developed to analyze the behaviour of the superposition circuit, and select optimized parameter values to satisfy the above design goals. The circuit is fed from two constant sources, one operating at power frequency and the other at variable HF. The modeling parameters for the PF and HF step-up transformers were based upon typical laboratory equipment. The capacitance C represents two paralleled test terminations each with a capacitance of 250pF, as calculated for a 1m section of 15kV$_{L-L}$ XLPE cable. Capacitance $C_1$ was included to block the PF voltages from the HF transformer HV terminal. Inductance L and capacitance $C_2$ constitute a second-order filter, to minimize damaging HF harmonics at the PF transformer HV terminal. Table 3-2 lists the constant and variable parameter values used in the MATLAB simulation model.

**Figure 3-2:** MATLAB Simulink model used for designing power frequency and high frequency superposition (PF + HF) circuit.

41

**Table 3-2:** Circuit parameters used for MATLAB Simulink modeling of PF + HF superposition circuit.

| Circuit Component | Parameter | Value(s) | Variance for Simulations |
|---|---|---|---|
| **PF Transformer**<br><br>*LV Winding Parameters*<br><br><br>*HV Winding Parameters* | Nominal Power (VA)<br>Nominal Frequency (Hz)<br>Voltage (rms)<br>Resistance (p.u.)<br>Inductance (p.u.)<br>Voltage V2 (rms)<br>Resistance (p.u.)<br>Inductance (p.u.) | 1000<br>60<br>208<br>0.037<br>0.01<br>16000<br>0.037<br>0.01 | Fixed |
| **HF Transformer**<br><br>*LV Winding Parameters*<br><br><br>*HV Winding Parameters* | Nominal Power (VA)<br>Nominal Frequency (Hz)<br>Voltage (rms)<br>Resistance (p.u.)<br>Inductance (p.u.)<br>Voltage V2 (rms)<br>Resistance (p.u.)<br>Inductance (p.u.) | 15000<br>20000<br>100<br>0.002<br>1.34E-04<br>15000<br>0.002<br>1.34E-04 | Fixed |
| **Test Terminations** | Capacitance C (pF) | 500 | Fixed |
| **PF Filter Capacitance** | Capacitance $C_1$ (nF) | 0.05, 0.25, 1.4, 7, 35<br>Base $C_1$ = 1.4 nF | Variable |
| **HF Filter Capacitance** | Capacitance $C_2$ (nF) | 1.25, 2.5, 5, 10, 20<br>Base $C_2$ = 5 nF | Variable |
| **HF Filter Inductance** | Inductance L (H) | 0.25, 0.5, 1, 2, 4<br>Base L = 1 H | Variable |

The capacitive impedance of the test sample C is orders of magnitude lower as seen by the HF source, as opposed to the PF source. The HF source power requirements are thus prohibitively high, if the source is required to supply both capacitive and resistive loads. Instead, operating the circuit at a kHz range series resonance as seen by the HF source, the HF source supplies only the circuits' high frequency resistive losses, and an amplitude gain is achieved between the output voltage $V_C$ and the high frequency output voltage $V_{HF}$. Furthermore, the series resonance frequency can be tuned by altering circuit parameters L, $C_2$, and $C_1$, to allow for a HF testing frequency as high as practically possible. Figure 3-3 shows the series resonance behaviour of the simulated superposition circuit, when L, $C_2$, and $C_1$ were independently varied. Additionally, the voltage boost $V_C/V_{HF}$, commonly known as the 'Quality' or Q factor, is shown for the same parameter variations. For the Q factor simulations $V_{HF}$ was maintained at a constant value, and the PF source set to null.
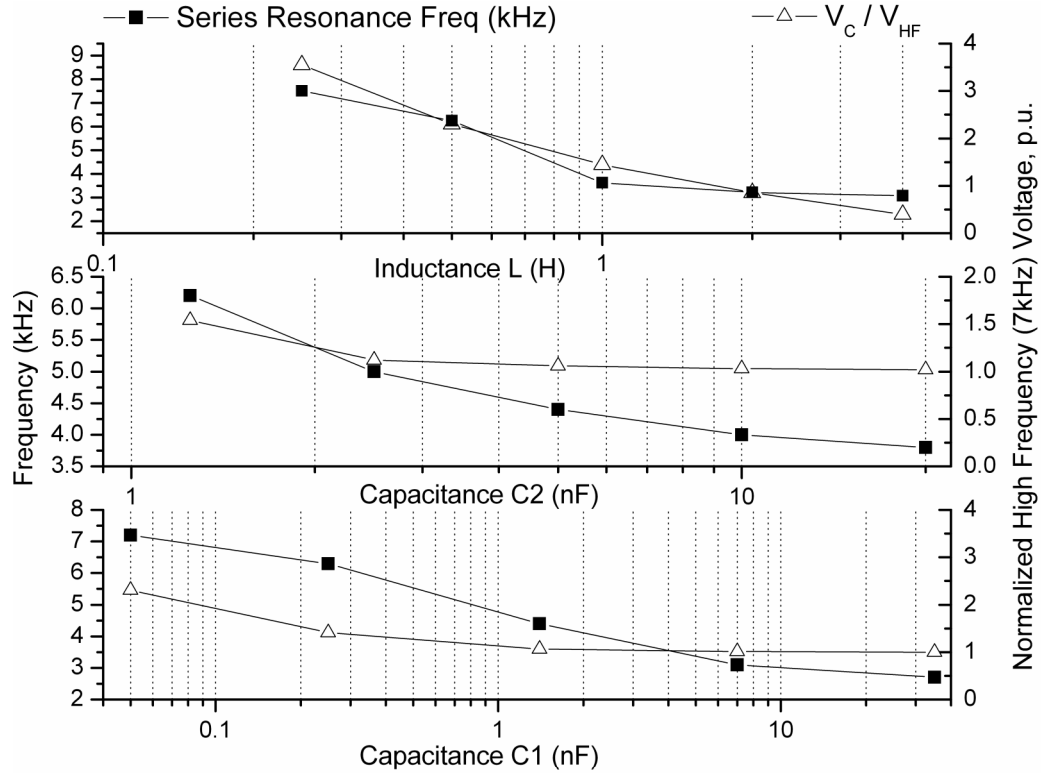
**Figure 3-3:** Series resonance frequency and $V_C/V_{HF}$ quality factor ratio, versus variation in superposition circuit parameters L, $C_1$, and $C_3$. Base values of $C_1 = 1.4$ nF, $C_2 = 5$ nF, and $L = 1$ H used for parameter variations.

Figure 3-3 shows that lower values of $C_1$ are desirable, to attain higher HF series resonance and circuit Q factor. For example, selecting $C_1 = 50$pF while maintaining $C_2$ and L at their base values, the series resonance frequency in the superposition model is 7.2 kHz, and a $V_C/V_{HF}$ boost of nearly 100% is attainable. Lower $C_1$ values also provide higher impedance to PF currents entering the HF transformer, rather than to HF currents flowing through $C_1$ to the test capacitance C. At 7.2 kHz for example, the impedance $1 / j\omega C_1$ is 120x less than the 60Hz impedance.

The choice of optimal parameter values for L and $C_2$ is more complex than shown in Figure 3-3. Although L and $C_2$ are both inversely related to series resonance frequency and Q factor, the same relationship does not apply to their HF filtering function. At 7.2 kHz for example, L has an impedance $j\omega L$ 120x greater than at 60Hz, and $1 / j\omega C_2$ is 120x less than at 60Hz. L and $C_2$ thus form a second-order HF filter, where L ideally absorbs the HF voltage at $V_C$, and $C_2$ shunts the HF current prior to entering the PF transformer. The HF filter requirements are thus in favour of higher L and $C_2$ values.

43

To compromise between the design goals of higher testing frequency, PF and HF filtering, and practical availability of components, parameter values of $C_1 = 250pF$, $C_2 = 5nF$, and $L = 1H$ were chosen for the superposition circuit. Figure 3-4 shows the final simulation results for the optimized circuit, with the source frequencies set to 7 kHz and 60 Hz, and HF amplitude adjusted to meet 40% of PF source peak voltage. These settings resulted in a $V_C/V_{HF}$ voltage gain of 1.5, HF harmonic distortion < 5% at the PF source, and 0.1% PF harmonic distortion at the HF source. The outputs also show that L and $C_1$ filter the HF and PF voltages respectively, as designed. Although $V_{C1}$ contains high frequency ripple, L, $C_1$, and $C_3$ in the experimental superposition circuit could be selected to withstand both PF and HF stresses.
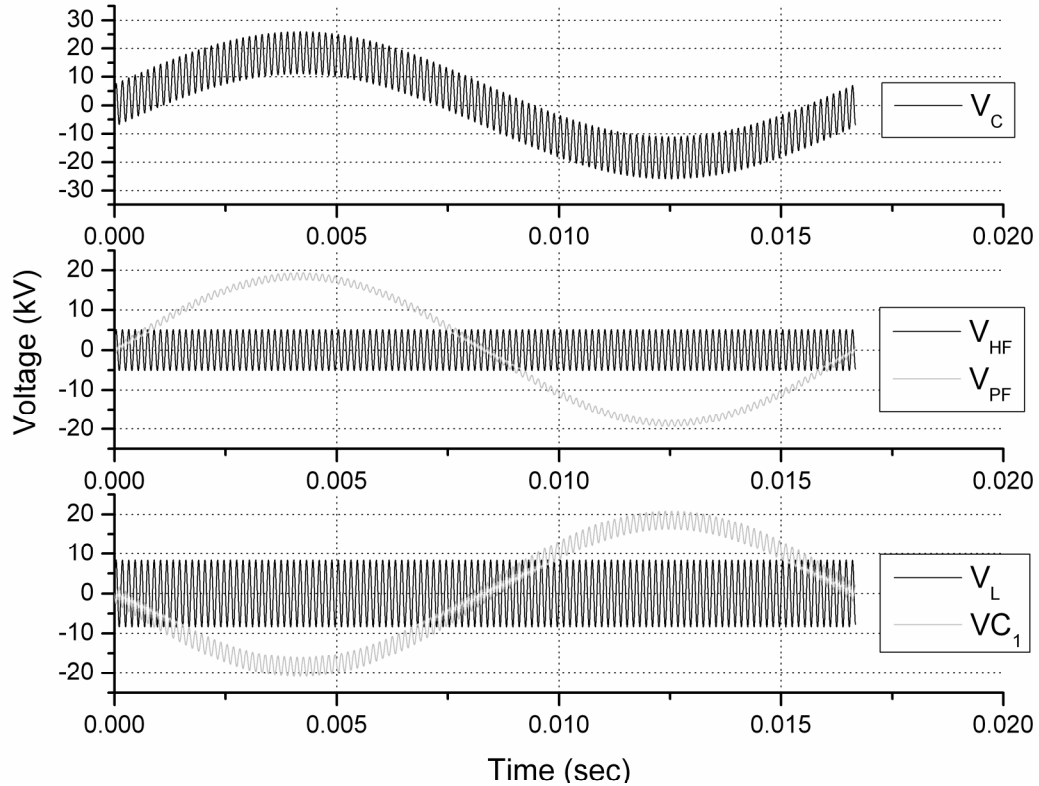


**Figure 3-4:** Simulated output voltage $V_C$, and corresponding voltage $V_{HF}$, $V_{PF}$, $V_L$, and $V_{C1}$, under combined 60Hz and 7kHz voltage application in MATLAB circuit shown in Figure 3-2.

## 3.2.2. Experimental Setup for High Voltage, PF and HF Superposition

Based on the simulation results and design goals discussed in Section 3.2.1, an experimental setup was designed to test commercial terminations T-1 to T-6 with power frequency, high frequency, and superimposed PF + HF voltages. Current circulation capabilities were also incorporated into the experimental setup, to test the terminations under simultaneous voltage application and elevated conductor temperature. Figure 3-5 shows the schematic of the experimental setup, and images of the corresponding circuit components. $V_C$ and $V_{HF}$ were measured at the locations shown in Figure 3-5, using Tektronix P6015A 20kV oscilloscope probes. $V_{PF}$ was measured at the PF transformer output, using a 200kV, 100pF Hipotronics capacitive divider. These dividers are omitted from Figure 3.4 for clarity. The circuit components and experimental outputs are discussed in Sections 3.2.2.1 – 3.2.2.5.

In addition to the features described in this section, the experimental setup also incorporated protection systems, HV safety interlock systems, and leakage current measuring shunt resistors. These features were designed primarily to enable long-term HF insulation ageing experiments, and also for safety in the short-term experiments conducted within this study. Descriptions of these auxiliary systems are included in Appendices B and C.

Power Freq. Source

AC Regulator

Power Freq. Transf.

TEST TERMINATIONS/
15kV$_{L-L}$ XLPE CABLE

$V_{PF}$ ③

C2

L

$V_C$ ②

Shunt Resistor

Shunt Resistor

AC Variac

C1

$V_{HF}$ ①

Shunt Resistor

High Freq. Transf.

High Freq. Amplifier

C3

Function Generator

High Freq. Source

Test Terminations

PF Transformer

Current Transformer

Shunt Resistors

C2 (HF Filter Capacitance)

HF Transformer

L (HF Filter Inductor)

C1 (PF Filter Capacitance)

**Figure 3-5:** Circuit schematic and actual corresponding components, for superimposed power frequency and high frequency (PF + HF) experimental setup.

46

### 3.2.2.1. High Frequency Generation and Transformation

The high frequency waveform in the superposition circuit was formed by combining a function waveform generator, commercial power amplifier, and HF ferrite-core transformer. An Agilent 33220A was used for function generation, with a frequency range between 1μHz to 20MHz. The function generator output was supplied into a Crown T8000 power amplifier, with a frequency range of 20Hz – 20 kHz. Although designed for audio applications, the rated power output for the T8000 was sufficient for powering the superposition circuit, as long as the HF testing frequency remained at or near series resonance. Outside of this range, the thermal limits of the amplifier were exceeded. Although this limited the HF test frequency range to the natural series resonance frequency of the setup, use of the T8000 avoided the purchase of significantly more expensive HF variable speed generators or tesla transformers, as used in other high frequency, high voltage testing research [3,27].

The variable capacitance $C_3$ shown in Figure 3-5 was used to protect the HF power amplifier. Since the T8000 is meant for audio speaker outputs, amplifier loads are expected to be above 4 Ω. When connected to the superposition circuit however, the amplifier load under HF operation dropped below 1 Ω, increasing the amplifier temperature toward its thermal limits. Connecting a capacitance around 1μF to the T8000 output increased the output HF impedance to > 20Ω at 7 kHz, allowing operation of the amplifier well within thermal limits.

HF transformation was provided by a custom-designed MagCap ferrite-core transformer, with a transformation ratio of 15000/100V and 15kVA rating. The frequency range for the HF transformer was 1 kHz – 20 kHz. The transformer output voltage was significantly distorted for frequencies less than 1 kHz; as such, no attempts were made to subject the transformer to dual PF and HF voltages.

### 3.2.2.2. Power Frequency Generation and Transformation

For PF transformation a Hipotronics test transformer was used, with a ratio of 150kV/600V and 20kVA rating. The PF voltage source for the Hipotronics transformer was a 600V isolated regulator. In an earlier version of the experimental setup, a pole-type distribution transformer was used, with a 16000/208V transformation ratio and 1600VA rating. The parameters for this transformer were used in the MATLAB model described in Section 3.2.1.

### 3.2.2.3. Superposition Circuitry

The circuit components $C_1$, $C_2$, and L were selected based upon the simulations results in Section 3.2.1, availability, and cost. Table 3-3 lists the component characteristics of $C_1$, $C_2$, and L, as applied in the experimental setup.

**Table 3-3:** Characteristics of PF filter capacitance $C_1$, HF filter capacitance $C_2$, and HF filter inductance L.

| Component | Unit Features | Actual/Maximum Component Value in Circuit | Actual/Maximum Withstand Voltage in Circuit | Manufacturer |
|---|---|---|---|---|
| $C_2$ (HF Filter Capacitor) | C = 0.01uF $V_{PF} = 15kV_{rms}$ Dissipation Factor = 0.1% Insulation: Polypropylene Laminate (PPP) | C = 0.005uF (2 units in series) $C_{MAX}$ = 0.01uF | V = $V_{MAX}$ = 30kV$_{rms}$ (2 units in series) | Plastic Capacitors |
| $C_1$ (PF Filter Capacitor) | C = 680pF $V_{PF/HF} = 10kV_{rms}$ Dissipation Factor = 0.2% Insulation: Epoxy | C = 227pF (3 units in series) $C_{MAX}$ = 6.1uF (9 units in parallel) | V = 30kV$_{rms}$ (3 units in series) $V_{MAX}$ = 90kV$_{rms}$ (9 units in series) | Vishay |
| L (HF Filter Inductance | L = 1H Frequency Range = 60Hz - 20kHz $V_{PF/HF} = 15kV_{rms}$ Pmax = 15kVA | L = $L_{MAX}$ = 1H | V = $V_{MAX}$ = 15kV$_{rms}$ | MagCap Engineering |

In addition to meeting the required design values, $C_1$ and $C_2$ were selected with low dissipation factors to withstand both power frequency and high frequency stresses in the superposition circuit. The HF inductor was custom-ordered, since the dual operation under PF and HF voltages required unique core design. An air core reactor could have met this dual withstand requirement, but the number and diameter of turns required for a 15kV$_{rms}$, 1 H air core design was significantly large.

### 3.2.2.4. Current Circulation

As shown in Figure 3-5, the superposition circuit includes a current transformer (CT), used to induce 60 Hz current in the parallel termination loop. The CT insulation rating is 5kV$_{rms}$, which is sufficient due to the 8.7kV$_{L-G}$ insulation level of the XLPE cable through the core. By back-feeding the 400:5 CT from a 120V, 20A rated voltage regulator, a PF current up to 350A could be induced in the conductor loop. This 350A level however was only possible following the modifications described in Section 2.3, which reduced burden on the CT.

### 3.2.2.5. Measured Superposition Outputs

Figure 3-6 shows typical PF + HF, filtered PF, and filtered HF voltage waveforms from the superposition test circuit. In Figure 3-6, PF transformer output voltage $V_{PF}$ is $13.1kV_{rms}$ (Ch1), and the HF transformer output voltage $V_{HF}$ is $4.51kV_{rms}$ at 7 kHz (Ch2). A voltage boost $V_C/V_{HF}$ of approximately 2.2 occurs across capacitance $C_1$, since the 7 kHz component in output voltage $V_C$ is $10kV_{rms}$ (Ch3). This is highly desirable, as a Q factor of 2.2 reduces the power requirements from the HF amplifier. PF and HF filtering functions are highly effective, and as predicted by MATLAB simulations. Second-order HF filtering by L and $C_3$ result in < 5% HF harmonic distortion at the PF transformer, at $13kV_{rms}$ PF output voltage. PF filtering by $C_2$ results in < 0.1% PF harmonic distortion at the HF transformer, at $4.51kV_{rms}$ HF output voltage.
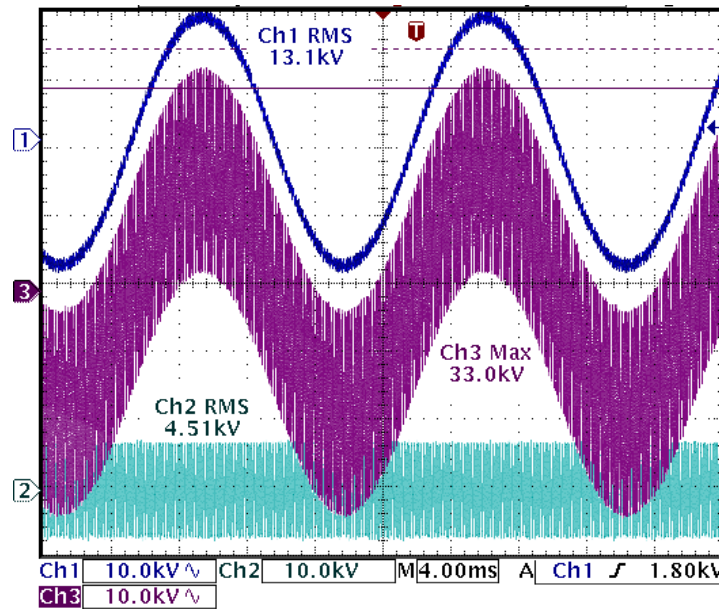


**Figure 3-6:** Sample output waveforms from circuit shown in Figure 3-5. Ch1, Ch2, and Ch3 waveforms correspond to $V_{PF}$, $V_{HF}$, and $V_C$ in Figure 3-5, respectively. Ch3 output voltage = $13kV_{rms}$ (60 Hz) + $10kV_{rms}$ (7 kHz).

For the chosen circuit parameters, the natural HF series resonance of the circuit is at 7 kHz; this value was thus chosen as the HF test frequency. By altering the values of $C_1$, $C_3$, and L within the ranges described in Table 3-3, the HF testing frequency can be varied between 6.5 – 7.5 kHz. These values also coincide with those predicted in MATLAB simulations. The maximum testing voltage $V_C$ is $30kV_{rms}$ for PF voltage application, and $15kV_{rms}$ for HF voltage application. For PF + HF testing, the peak voltage is ≈ $40kV_{peak}$.

From this discussion, the superposition circuit design goals established in Section 3.2.1 are achieved with the realized experimental circuit. Further, the measurement outputs meet or exceed the results predicted by MATLAB simulations.

### 3.2.3. Diagnostic Measurements

### 3.2.3.1. Thermal Camera

Cable termination surface temperatures were measured using a FLIR-SC500 infrared camera. The emissivity spectra of the camera is between 7.5 and 13μm, and the measurement accuracy 2K over the range 273 to 773K. The emissivity used for terminations T-1 to T-5 was 0.95, to account for the dark grey rubber housings [7,37]. For termination T-6 with red rubber housing, an emissivity value of 0.92 was used. Using the ThermaCAM$^{TM}$ Researcher software, maximum surface temperatures were continuously acquired. Figure 3-7 shows the acquisition screen, with a thermal image and time plot of termination T-1 under increasing high frequency voltage application.
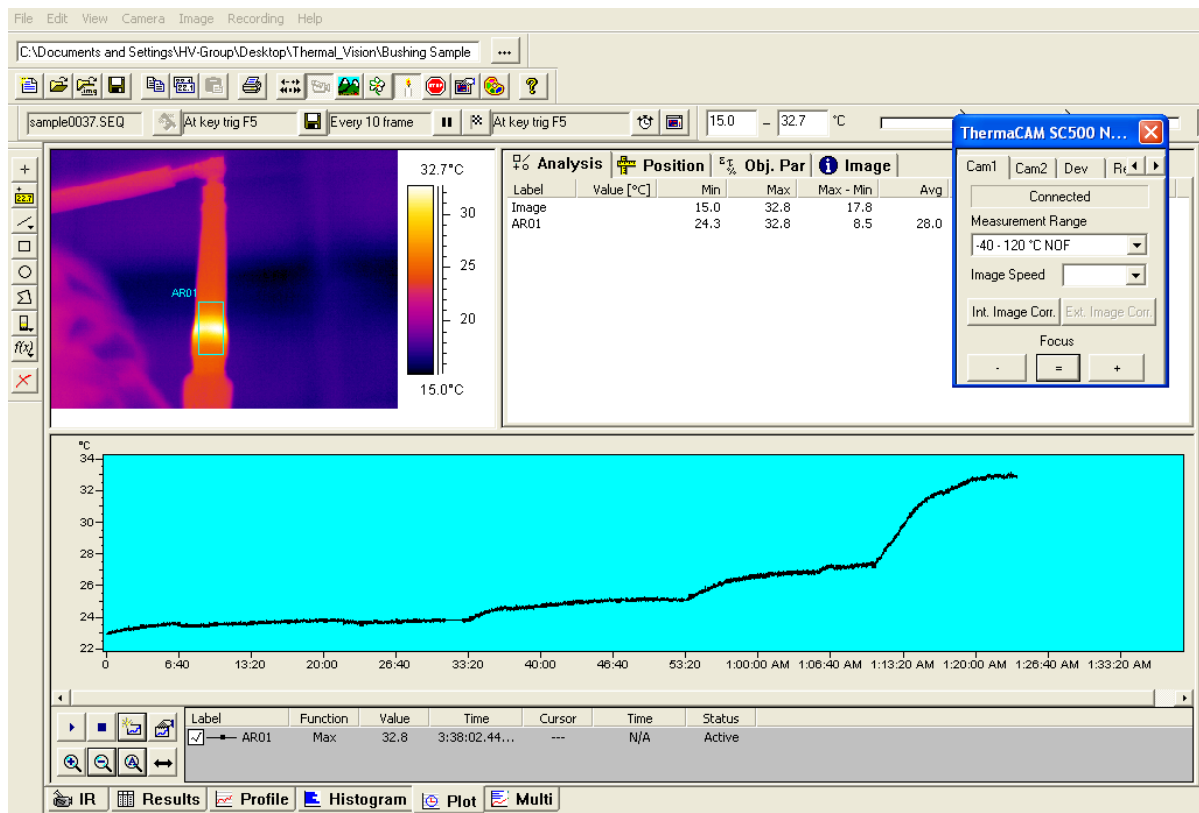


**Figure 3-7:** FLIR SC-500 thermal image and surface temperature plot for T-1, under increasing HF voltage.

### 3.2.3.2. Partial Discharge Measurements

Partial discharge tests were performed on all new termination samples, prior to subjecting them to PF, HF, or PF + HF testing. By confirming that each installation was PD-free, any surface temperature rise observed under HF stress could be attributed to resistive heating, rather than PD activity in the test termination.

The PD measurement system used was a Tettex Instruments DDX-9101, meeting the requirements of IEC 60270 [38]. The PF source for the setup was a Hipotronics 150kV, 20kVA test transformer, also used as the superposition circuit PF source. This transformer was specially designed with PD < 1pC at $150kV_{rms}$. Despite the low transformer PD, initial tests showed extremely high background PD levels between 120 – 140pC at $150kV_{rms}$. The problem was determined to be noise from the utility laboratory power supply, feeding through the $600V_{rms}$ PD unit regulator and the interconnected laboratory grounding system. Following application of a laboratory isolation transformer, the PD sensitivity levels increased to 3pC at $150kV_{rms.}$

The PD measurement procedure for the test terminations was adopted from IEC 61442 and IEC 60502-4, for accessories with $V_{L-N}$ = $8.7kV_{rms}$ [31,39]. The applied voltage was raised 25% above the testing voltage level $V_t$, specified as $1.73V_{L-G}$ or $15kV_{rms}$. The voltage was held at this level for 10 seconds, and then reduced to $V_t$. If the detectable discharge at $V_t$ was less than 10pC, the termination passed the quality test [39]. These initial tests revealed that the slip-over type termination T-1 showed higher susceptibility to PD levels > 10pC, following installation. Figure 3-8 (a) shows the unacceptably high PD levels for T-1 following the first installation, whereas Figure 3-8 (b) the acceptable PD levels for termination T-4. Subsequent careful installations of T-1 achieved PD levels less than 10pC, as for all other termination designs.

| Discharge Magnitude | Voltage (HV Sync) | Discharge Magnitude | Voltage (HV Sync) |
| 218 pC | 12.11 kV | 2.34 pC | 24.10 kV |

(a)                                                        (b)
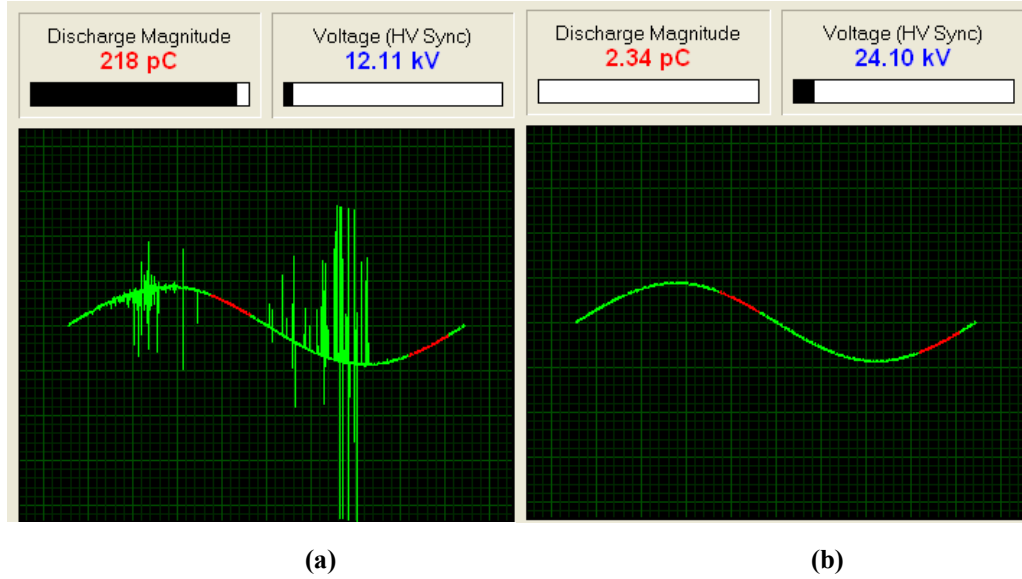
**Figure 3-8:** Example sine-wave PD plots from DDX-9101 setup, for (a) Termination T-1 and (b) Termination T-4, following initial test sample installations.

## 3.2.4. Termination Testing Experimental Procedure

The experimental setup described in Sections 3.2.1 – 3.2.3 was used to subject two samples of each of the six test terminations to power frequency, high frequency, and combined PF + HF voltage stresses, with and without additional current circulation. Table 3-4 summarizes the test conditions applied to terminations T-1 to T-6. For the tests designated as PF, HF, PF + current, and HF + current, the voltage amplitude was increased between $0.25V_{L-G}$ to $1.5V_{L-G}$, with $V_{L-G} = 8.7kV_{rms}$. This procedure was used to assess the effects of individual power frequency or high frequency stress, at ambient and elevated conductor temperatures. For the tests designated as PF + HF and PF + HF + current, the PF voltage was held constant at $13kV_{rms}$, and the HF voltage varied between $0.25V_{L-G}$ to $1.5V_{L-G}$, with $V_{L-G} = 8.7kV_{rms}$. This procedure was used to assess the effects of high frequency stress superimposed on constant power frequency voltage. Combined with a variation of conductor temperature, these conditions closely represented those of actual field HF harmonic resonance, as discussed in Chapter 1.

**Table 3-4:** Experimental conditions for testing terminations T-1 to T-6.

| Test # | Frequency | Voltage Level | Current | Test Designation |
|--------|-----------|---------------|---------|------------------|
| 1 | 60Hz | 0 - 13kV$_{rms}$ | 0 | PF |
| 2 | 7kHz | 0 - 13kV$_{rms}$ | 0 | HF |
| 3 | 60Hz + 7kHz | 13kV$_{rm(}$ (PF), 0 – 13kV$_{rms}$ (HF) | 0 | PF + HF |
| 4 | 60Hz | 0 - 13kV$_{rms}$ | ~250A$_{rms}$ (60Hz) | PF + Current |
| 5 | 7kHz | 0 - 13kV$_{rms}$ | ~250A$_{rms}$ (60Hz) | HF + Current |
| 6 | 60Hz + 7kHz | 13kV$_{rm(}$ (PF), 0 – 13kV$_{rms}$ (HF) | ~250Arms (60Hz) | PF + HF + Current |

# Chapter 4. Results

This chapter presents FEM simulation results based on COMSOL Multiphysics™, and experimental results using the PF + HF superposition setup described in Chapter 3. As detailed in Section 3.1.2, FEM simulations analyzed surface electric field, resistive heating, and maximum temperature rise in a model termination using the dimensions of test termination T-4, and simulated stress grading layers SG-A to SG-E. Parameters varied were applied voltage and frequency, SG electrical conductivity and permittivity, and SG thermal conductivity. The influence of termination geometry was also studied, using additional models representing test terminations T-2 and T-3. In experimental tests as described in Section 3.2.4, the six test terminations T-1 to T-6 were subjected to PF, HF, and superimposed PF + HF voltage stresses, with and without additional current circulation. Prior to each experiment, partial discharge measurements were conducted on each test termination. During each experiment, cable surface temperatures were continuously measured using the FLIR SC-500 infrared camera, in the stress grading region of each termination.

## 4.1. Simulation Results

### 4.1.1. Electric Field Distribution and Resistive Heating

Figures 4-1 (a) to (d) and 4-2 show the computed results for electric field (E) and resistive heating (Q) along the insulation surface, for simulated materials SG-A to SG-E. Results for field-dependent materials SG-A to D show typical 'field-limiting' regions, explained later in this section. The results for E and Q were computed along a line parallel to and a radial distance of 0.2mm from the model termination insulation surface, starting at the semi-conductive screen cutback. The calculations are shown for a conductor potential of $V_{L-G}$ = 13kV$_{rms,}$ and frequencies of 60 Hz and 7 kHz; these parameters correspond with experimental test conditions in this study.
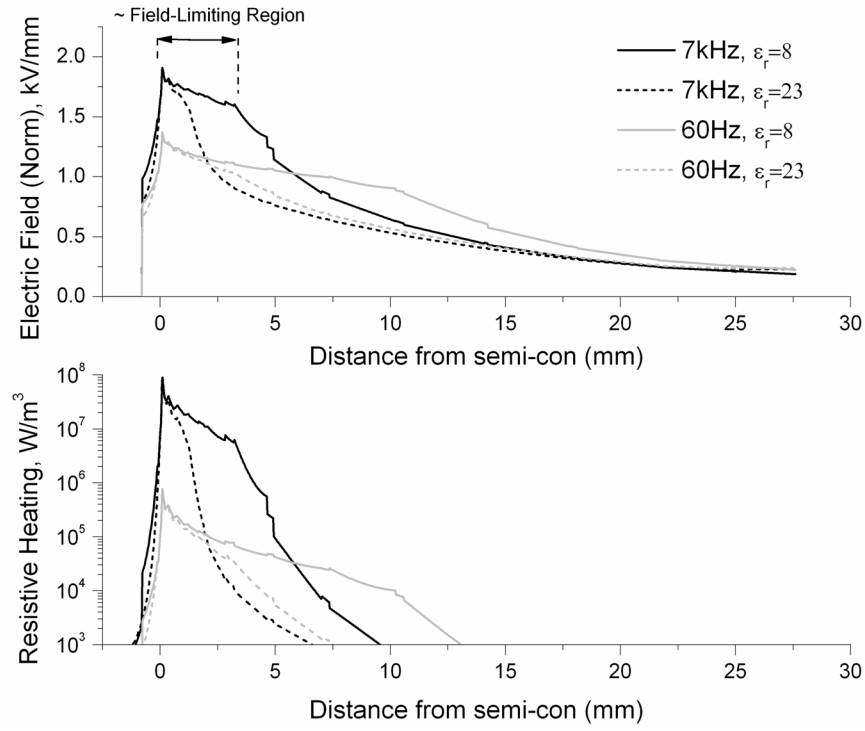
**(a)**
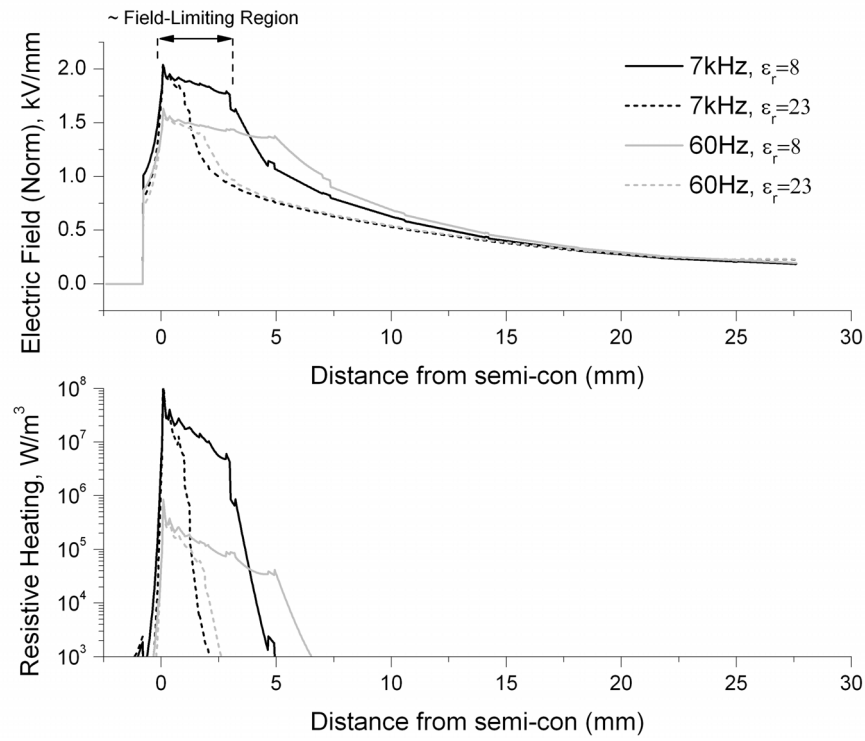


**(b)**
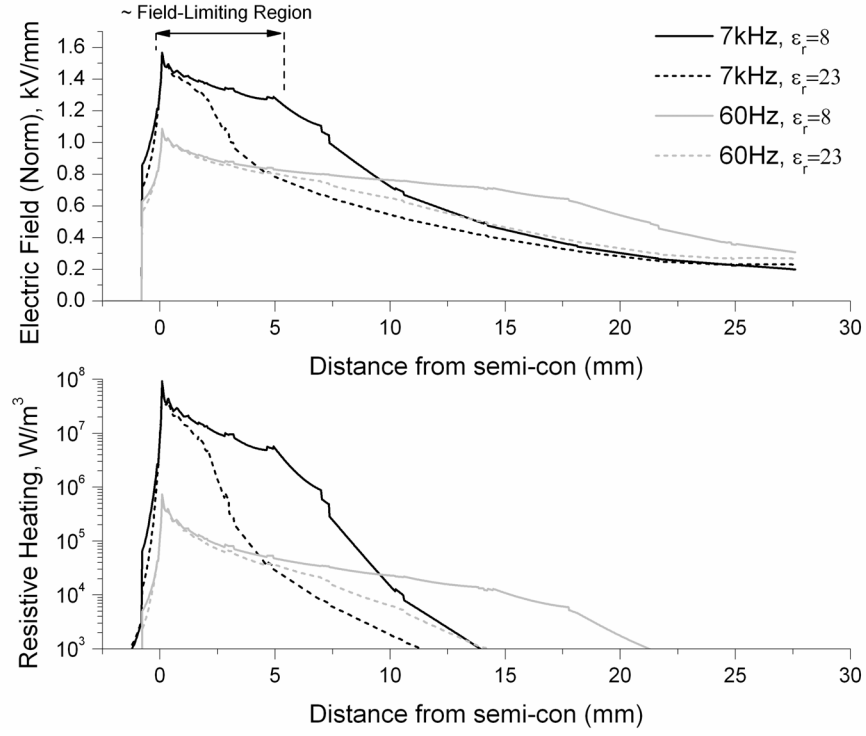
**(c)**
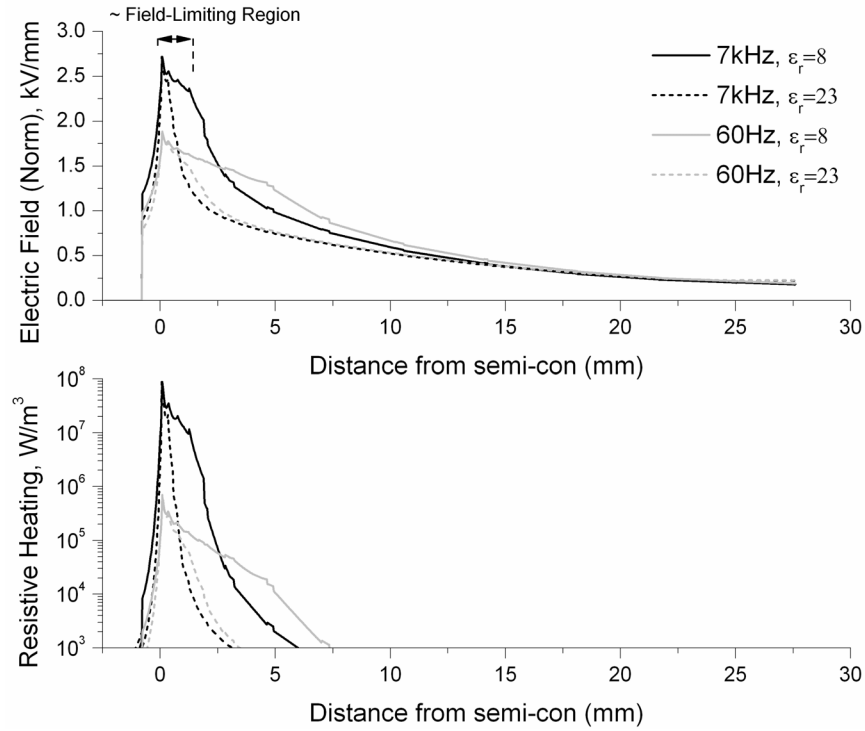


**(d)**

**Figure 4-1:** Electric field and resistive heating as a function of distance from semi-con cutback for $V_{L\text{-}G}$ = 13kV$_{rms,}$ and frequencies of 60 Hz and 7 kHz. Results computed on model FEM termination using sample field-dependent materials (a) SG-A, (b) SG-B, (c) SG-C, and (d) SG-D, with relative permittivities $\varepsilon_r$ = 8 and 23.
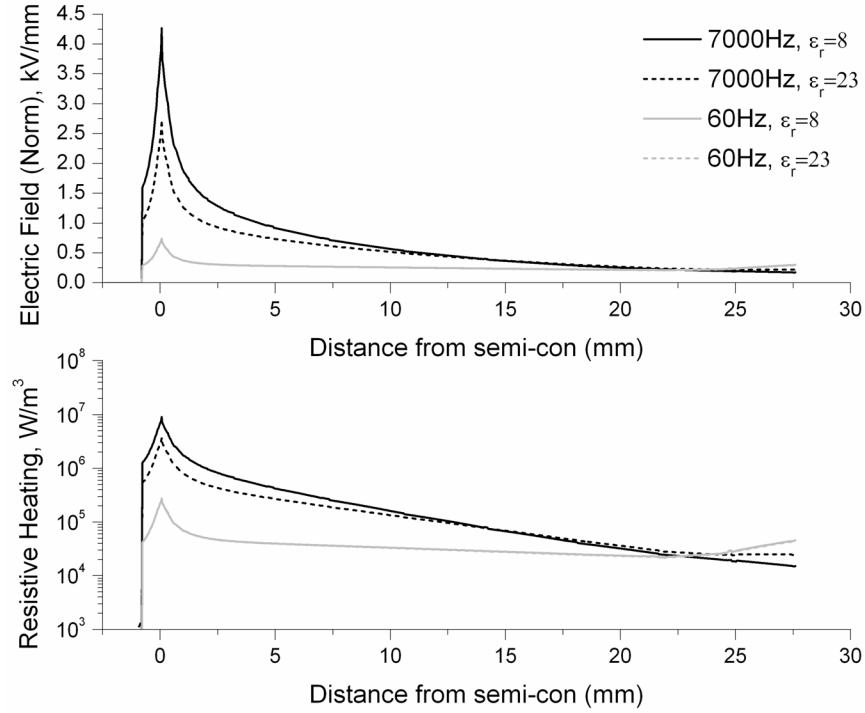
**Figure 4-2:** Electric field and resistive heating as a function of distance from semi-con cutback for $V_{L-G}$ = 13kV$_{rms,}$ and frequencies of 60 Hz and 7 kHz. Results computed on model FEM termination using sample field-independent material SG-E, with relative permittivities $\varepsilon_r$ = 8 and 23.

For field-dependent materials SG-A to SG-D, the maximum electric field $E_{max}$ at $V_{L-G}$ = 13kV$_{rms}$ and 60 kHz is seen to remain well below the ionization potential of termination air cavities. When the applied frequency is 7 kHz, $E_{max}$ increases to range between 1.6kV/mm and 2.75kV/mm, depending upon the simulated SG material. In addition to raising the maximum electric field, higher frequency increases the field concentration around the semi-con screen edge. At 7 kHz and low permittivity for example, this field concentration resembles a cut-off peak, shown in Figures 4-2 (a) to (d) as the SG 'field-limiting' region. The width and magnitude of the field-limiting region is clearly dependent upon the SG material conductivity parameters and voltage frequency. A detailed discussion on the theory of field-limiting behaviour is present in Chapter 5.

Resistive heating computations show that at 60 Hz, the maximum resistive loss ($Q_{max}$) for all field-dependent materials remains below $1 \times 10^{-6}$ W/m$^3$. At 7 kHz however, $Q_{max}$ increases by nearly two orders of magnitude for all field-dependant grading materials. Comparing the grading materials, SG-C shows the maximum area under its resistive heat curve at 7 kHz, whereas SG-D the minimum. The area under the Q curves ($Q_{av}$) represents resistive heat

generated along the termination surface; thus under HF conditions, material SG-C would be expected to reach the highest temperatures and SG-D the least.

For materials SG-A to SG-D, changing the relative permittivity between $\varepsilon_r = 8$ and 23 has minimal effect on the maximum electric field or resistive heating, holding frequency constant. $Q_{av}$ however drops with increasing permittivity; thus an increase from $\varepsilon_r = 8$ to 23 would likely reduce temperature rise in all SG materials. Further, increasing permittivity decreases the width of the field-limiting region.

The behaviour of material SG-E, which has constant conductivity, is significantly different from field-dependant materials SG-A to SG-D. From Figure 4-2 we see that for the constant conductivity material no field-limiting region exists near the semi-con edge, and $E_{max}$ is higher than in all field-dependant grading materials. SG-E is however characterized by a low $Q_{max}$, an order of magnitude lower at 7 kHz than in the field-dependant grading materials.

### 4.1.2. Maximum Surface Temperature Rise

Figures 4-3 to 4-5 show computed results for maximum surface temperature rise for materials SG-A to SG-E, both along the insulation surface ($T_{max\_in}$) and outer housing surface ($T_{max\_out}$). The conductor potential is varied between $0.25V_{L-G}$ to $1.5V_{L-G}$, where $V_{L-G} = 8.7kV_{rms}$. This range corresponds to the experimental voltage range applied to test terminations, $4.4kV_{rms} - 13kV_{rms}$. Figure 4-3 shows the temperature rise results at 60 Hz, whereas Figures 4-4 and 4-5 the results at 7 kHz. The power frequency results are shown for $T_{max\_in}$ with $\varepsilon_r = 8$ only, since there is no variation in results for $\varepsilon_r = 23$, and $T_{max\_in}$ or $T_{max\_out}$.

The influence of thermal conductivity k was studied for SG-A, by calculating the surface temperature rise with k = 0.6, 0.9, and 1.3 W/m.K respectively These k values are representative of measurements from field-dependent SG composites, reportedly between 0.58 and 1.3 W/m.K [7]. The data points shown in Figure 4-4 are for k = 0.9 W/m.K, and the results for k = 0.6 and 1.3 W/m.K are shown as the maximum and minimum error range, respectively. The results for SG-B to SG-E showed no variation, and are thus omitted.
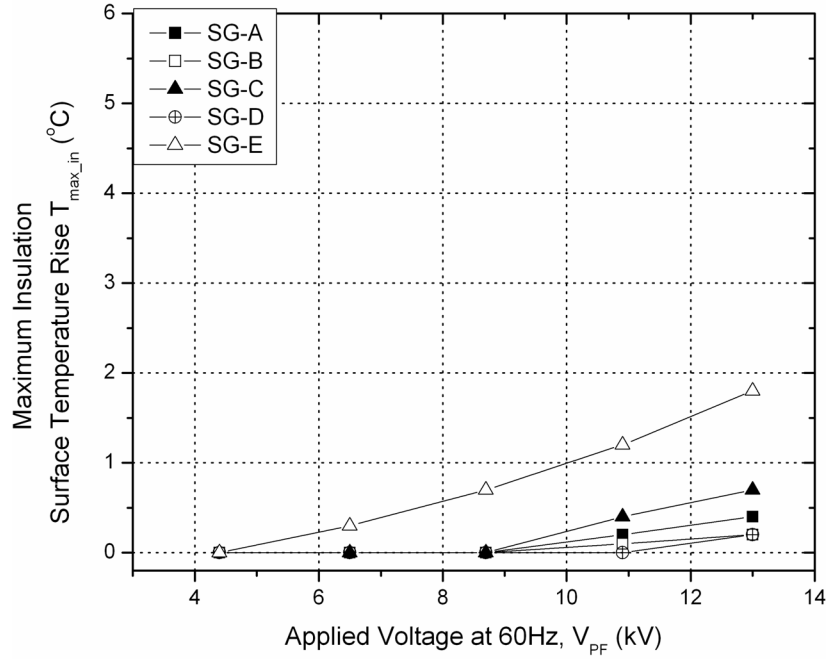
**Figure 4-3:** Maximum computed temperature rise along insulation surface ($T_{max\_in}$) for simulated materials SG-A to SG-E with $\varepsilon_r = 8$, at power frequency.
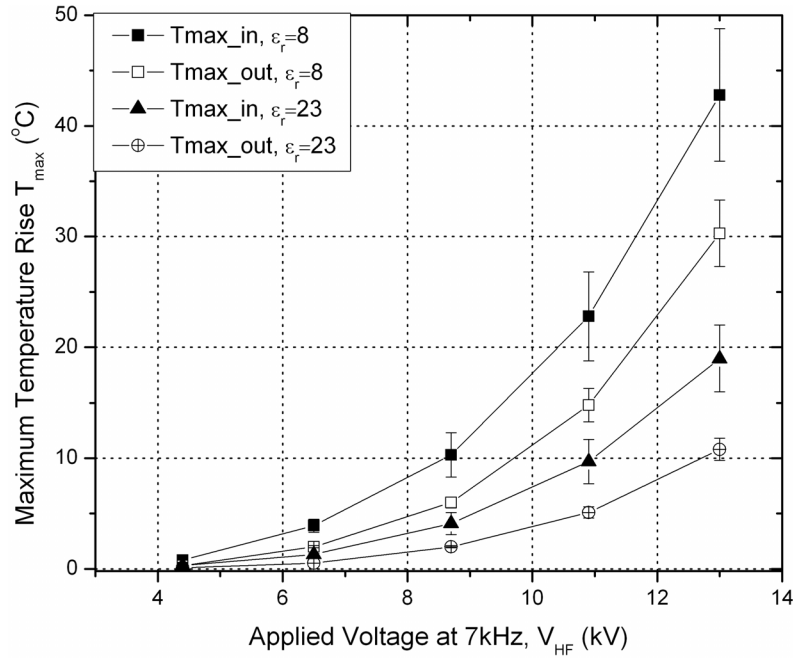


**Figure 4-4:** Maximum computed temperature rise along insulation surface ($T_{max\_in}$) and outer housing ($T_{max\_out}$) for simulated material SG-A, at 7 kHz, with two different permittivities $\varepsilon_r = 8$ and 23. Maximum and minimum error bars show $T_{max}$ results when thermal conductivity is changed between 0.6 and 1.3 W/m.K, respectively.
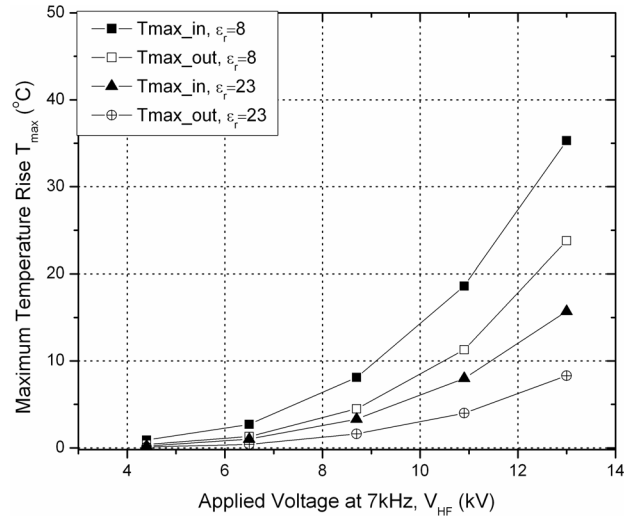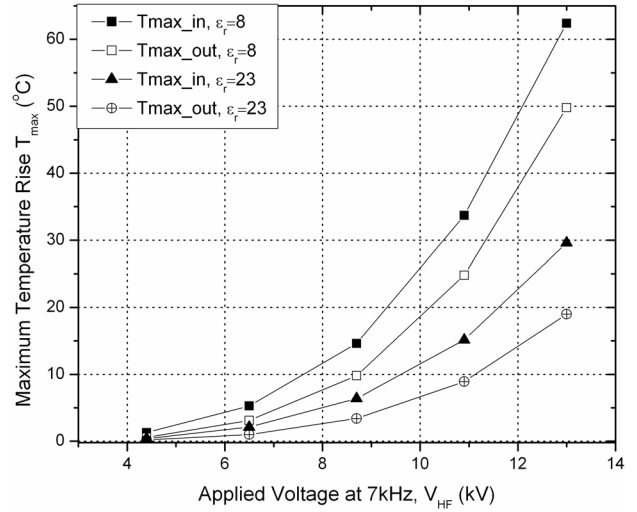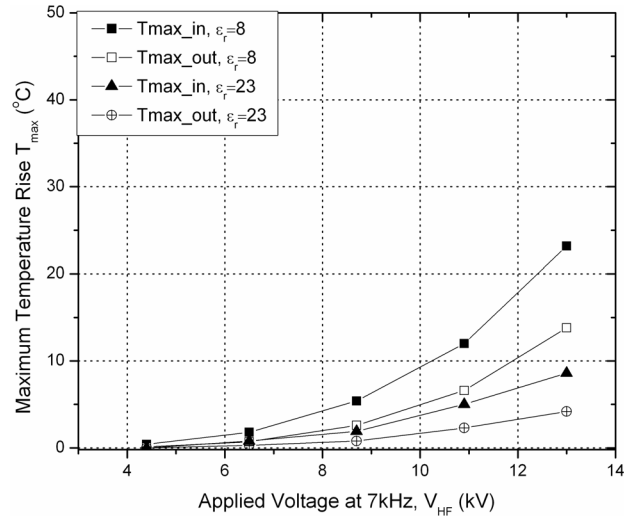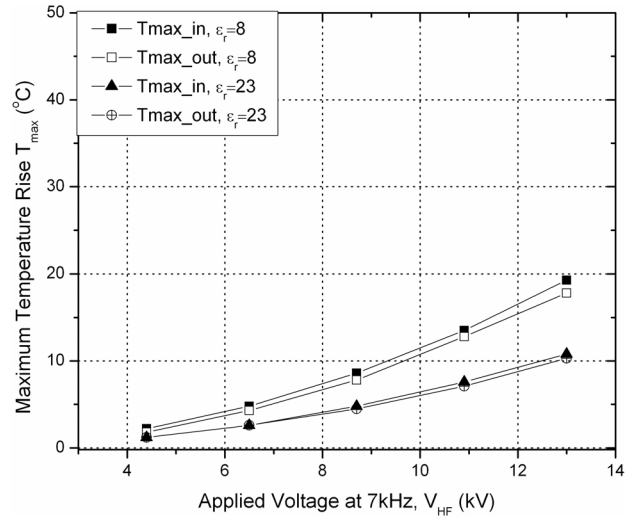
**Figure 4-5:** Maximum computed temperature rise along insulation surface ($T_{\text{max\_in}}$) and outer housing ($T_{\text{max\_out}}$) for simulated materials (a) SG-B, (b) SG-C, (c) SG-D, and (d) SG-E, at 7 kHz, with two different permittivities $\varepsilon_r = 8$ and 23.

60

The trends for insulation and outer housing surface temperature rise correspond with the resistive heating computations from Section 4.1.1. For all field-dependent materials, Figure 4-3 shows minimal $T_{max\_in}$ at 60Hz. At 7 kHz however, $T_{max\text{-}in}$ and $T_{max\_out}$ for SG-A to SG-D increase more than linearly with increasing HF voltage. The largest insulation surface temperature rise of 62°C is seen for SG-C at $\varepsilon_r = 23$, whereas the minimum $T_{max\text{-}in}$ of 9°C is computed for SG-D, at $\varepsilon_r = 8$. All field-dependent materials show a drop between insulation and outer housing surface temperature; at $\varepsilon_r = 8$ for example, materials SG-A to SG-D all show a minimum 10°C drop between $T_{max\text{-}in}$ and $T_{max\_out}$. Increasing the permittivity results in lower insulation and outer housing surface temperatures, as clearly predicted from the resistive heating computations. This effect is most significant for SG-D, where $T_{max\_out}$ drops from 62°C to 30°C with a permittivity increase from $\varepsilon_r = 8$ to 23.

For the constant conductivity material SG-E, Figure 4-3 shows a linear surface temperature rise up to 2°C at 60 Hz and $V_{L\text{-}G} = 13kV_{rms}$. Compared to the field-dependent materials, this is the highest surface temperature rise under power frequency application. At 7 kHz however, Figure 4-5 (d) for SG-E shows minimal variation between insulation and outer housing surface temperatures, and a linear relationship between surface temperature rise and applied HF voltage, as expected.

### 4.1.3. Geometry Influence

The influence of termination geometry was studied by comparing electric field and resistive heating among three termination geometries. These models were designed to represent geometric (stress cone) test termination T-2, and non-geometric test terminations T-3 and T-4. The non-geometric designs varied in length and thickness of applied SG material and outer housing, and were modeled using SG-A material with $\varepsilon_r = 8$ and k = 0.9 W/m.K. Figure 3-1 showed the meshed FEM models representing T-2, T-3, and T-4.

E and Q were computed along the inner insulation surface starting from the semi-con cutback in models T-3 and T-4, and the beginning of the capacitive stress cone in model T-2. Results are shown in Figure 4-6 (a) at 60 Hz, and (b) at 7 kHz.

61
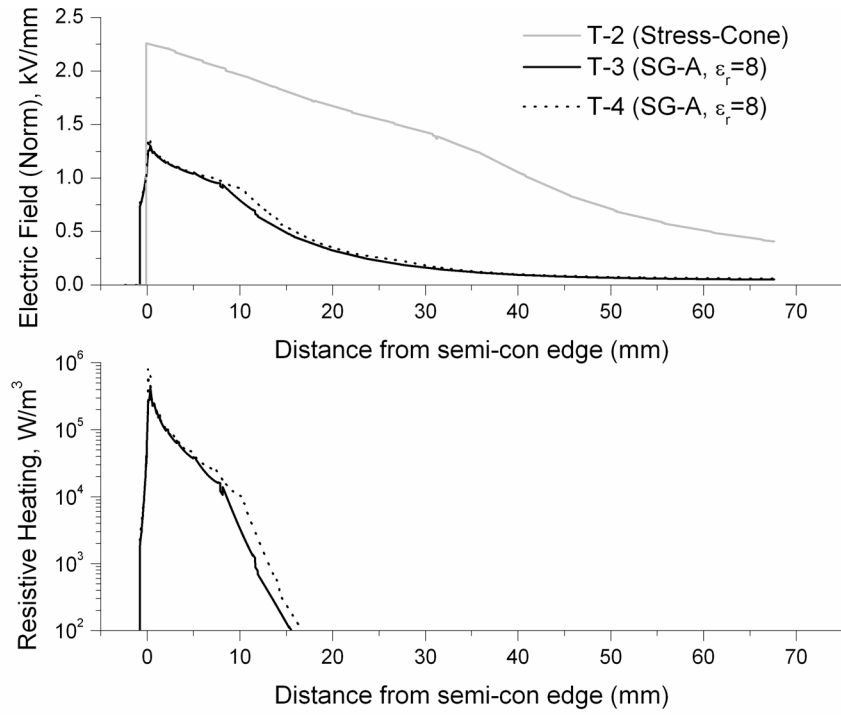
**(a)**
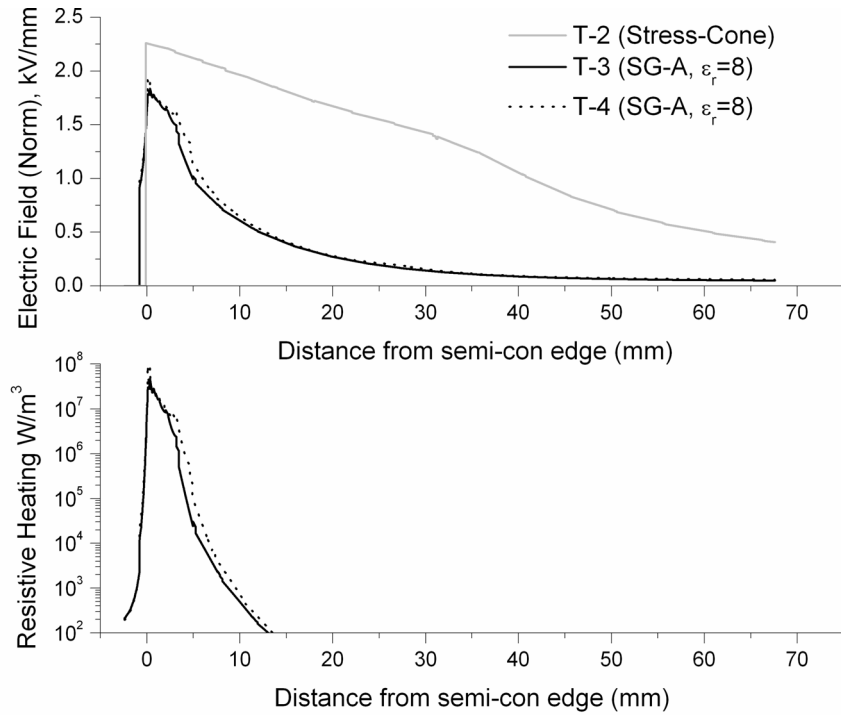


**(b)**

**Figure 4-6:** Electric field and resistive heating along the insulation surface at (a) 60 Hz and (b) 7 kHz, for FEM model terminations representing T-2, T-3, and T-4.

Figure 4-6 shows that at both 60 Hz and 7 kHz, E and Q profiles for non-geometric models T-3 and T-4 are identical.  Thus the dimensional variations between T-3 and T-4 show no effect on electric field and resistive heating, and consequently on maximum surface temperatures.  For geometric termination model T-2, the electric field results for 60 Hz and 7 kHz are identical.  Although the maximum electric field is higher for T-2 than in T-3 or T-4, it is limited to 2.25 kV/mm in both cases.  Resistive heating is non-existent for the T-2 model, thus $T_{max\_in}$ and $T_{max\_out}$ in this design would be zero.

## 4.2. Experimental Results

As discussed in Section 3.2, experimental tests were performed on two samples of each test termination T-1 to T-6 under power frequency, high frequency, and superimposed PF + HF voltage stresses, with and without current circulation.  Tests on each of the two test samples yielded identical results.  Thermal hotspots, absolute temperature, and maximum surface temperature rise ($T_{max}$) over ambient were recorded with voltage ranging between $0.25V_{L-G}$ to $1.5V_{L-G,}$ where $V_{L-G} = 8.7kV_{rms.}$  Results shown in Section 4.2.1 correspond to Table 3-4 test conditions # 1 - 3, where 60 Hz, 7 kHz, and 60 Hz + 7 kHz voltage stresses are applied without current circulation.  Results shown in Section 4.2.2 correspond to test conditions # 4 – 6, where 60 Hz, 7 kHz, and 60 Hz + 7 kHz voltage stresses are applied with approximately $250A_{rms}$ of power frequency current circulation.

### 4.2.1. Thermal Behaviour of Test Terminations, without Current Circulation

Figure 4-7 shows an example thermography image, with terminations T-3 and T-4 stressed at $13kV_{rms}$ (60 Hz) + $13kV_{rms}$ (7 kHz) voltage.  The SG hotspots are seen clearly, and the marked areas show where maximum surface temperatures were recorded over time and applied voltage.  The results of the thermal analysis for termination samples T-1 to T-6 under power frequency, high frequency, and combined PF + HF voltage application are shown in Figure 4-8.
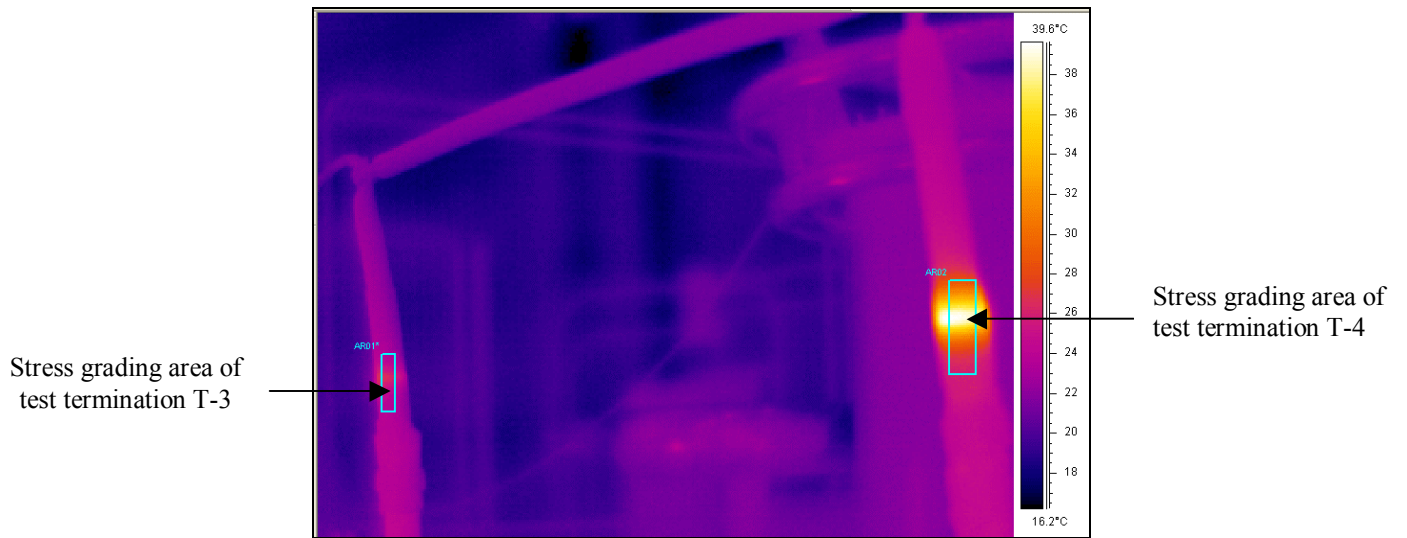
**Figure 4-7:** Example of thermography image showing terminations T-3 and T-4, subject to combined 60 Hz and 7 kHz voltage stress, without current circulation.



**Figure 4-8:** Maximum surface temperature rise ($T_{max}$) over ambient for test termination T-1, as a function of applied voltage, for power frequency, high frequency, and combined PF + HF stresses (test conditions #1 - #3).

**Figure 4-9:** Maximum surface temperature rise ($T_{max}$) over ambient for test termination T-2, as a function of applied voltage, for power frequency, high frequency, and combined PF + HF stresses (test conditions #1 - #3).



**Figure 4-10:** Maximum surface temperature rise ($T_{max}$) over ambient for test termination T-3, as a function of applied voltage, for power frequency, high frequency, and combined PF + HF stresses (test conditions #1 - #3).

**Figure 4-11:** Maximum surface temperature rise ($T_{max}$) over ambient for test termination T-4, as a function of applied voltage, for power frequency, high frequency, and combined PF + HF stresses (test conditions #1 - #3).



**Figure 4-12:** Maximum surface temperature rise ($T_{max}$) over ambient for test termination T-5, as a function of applied voltage, for power frequency, high frequency, and combined PF + HF stresses (test conditions #1 - #3).
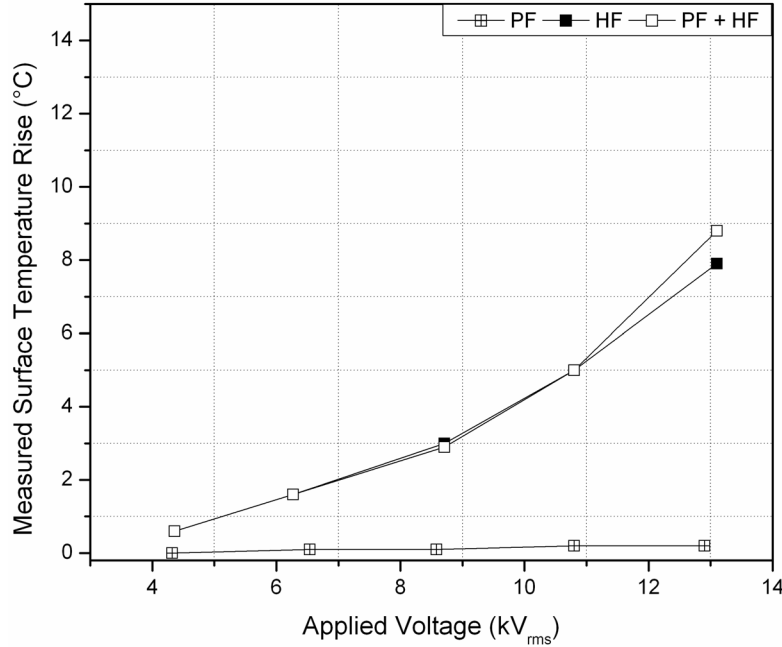
**Figure 4-13:** Maximum surface temperature rise ($T_{max}$) over ambient for test termination T-6, as a function of applied voltage, for power frequency, high frequency, and combined PF + HF stresses (test conditions #1 - #3).

From Figures 4-8 to 4-13 it can be seen that under power frequency voltage application, there are no hotspots generated in any of the termination designs tested. Under HF voltage application however, the results for T-1 to T-6 show a wide variation in maximum surface temperature rise $T_{max}$ over ambient. Geometric design T-2 remains nearly unaffected, as expected due to its capacitive grading. However, $T_{max}$ in the SG area of terminations T-1 and T-3 to T-6 increases more than linearly, with T-4 showing the largest increase of 16.6ºC at $13kV_{rms}$, 7 kHz. These results follow the surface temperature rise trends from FEM computations, using field-dependent materials SG-A to SG-D. The test results for combined PF + HF voltage application for the test terminations are consistent with the results for HF application alone, with the only exception being T-2. This means that the hotspot formation is due predominantly to the HF harmonic component, even though the peak voltage is significantly higher with PF + HF superposition (maximum $V_{peak}$ = ~37kV).

## 4.2.2. Thermal Behaviour of Test Terminations, with Current Circulation

The second set of tests incorporated current circulation within the XLPE cable conductors, to analyze SG overheating under pseudo-field current loading conditions. Figure 4-14 shows an

example thermography image of terminations T-5 and T-6, simultaneously stressed with 13kV$_{rms}$ (60Hz) and 13kV$_{rms}$ (7 kHz) voltages, as well as 250A$_{rms}$ of power frequency current. Figures 4-15 to 4-20 show the thermal analysis results from test terminations T-1 to T-6, under simultaneous voltage and current application.
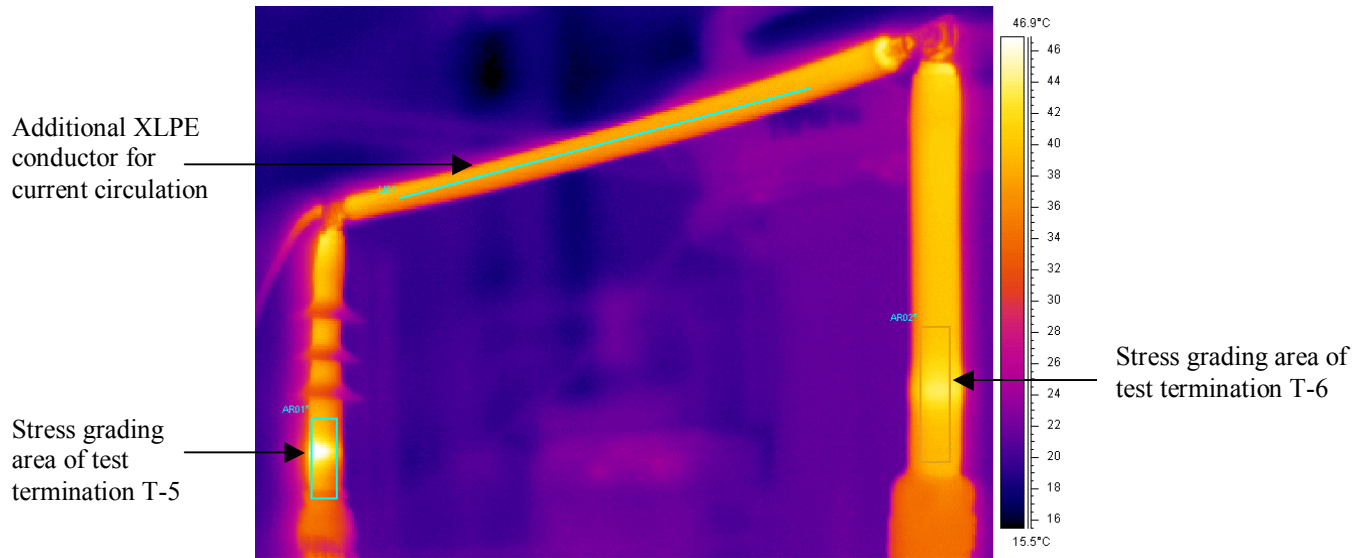


**Figure 4-14:** Example of thermography image showing terminations T-5 and T-6, subject to combined 60 Hz and 7 kHz voltage stress, with ~250A$_{rms}$ of power frequency current circulation.
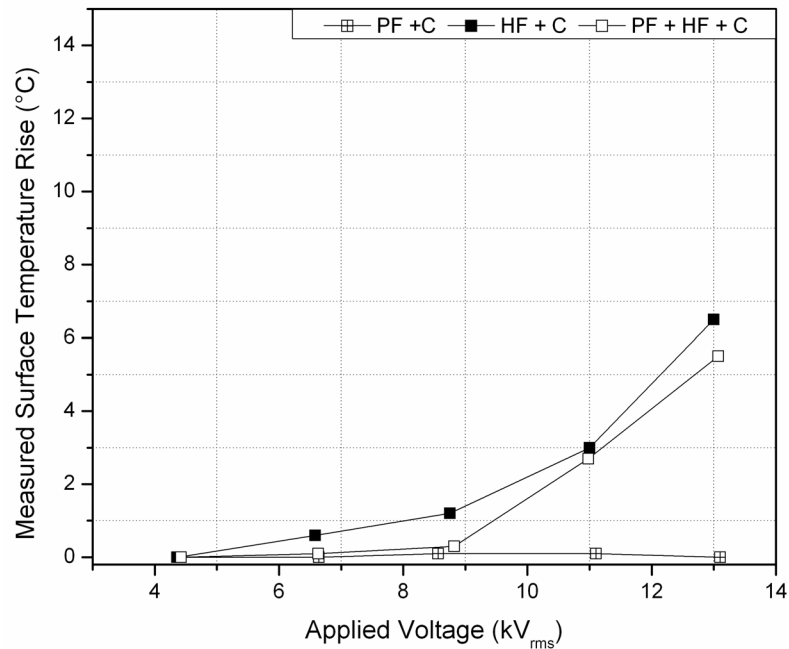


**Figure 4-15:** Maximum surface temperature rise (T$_{max}$) over ambient for test termination T-1, as a function of applied voltage, for PF, HF, and combined PF + HF stresses with current circulation (test conditions #4 - #6).
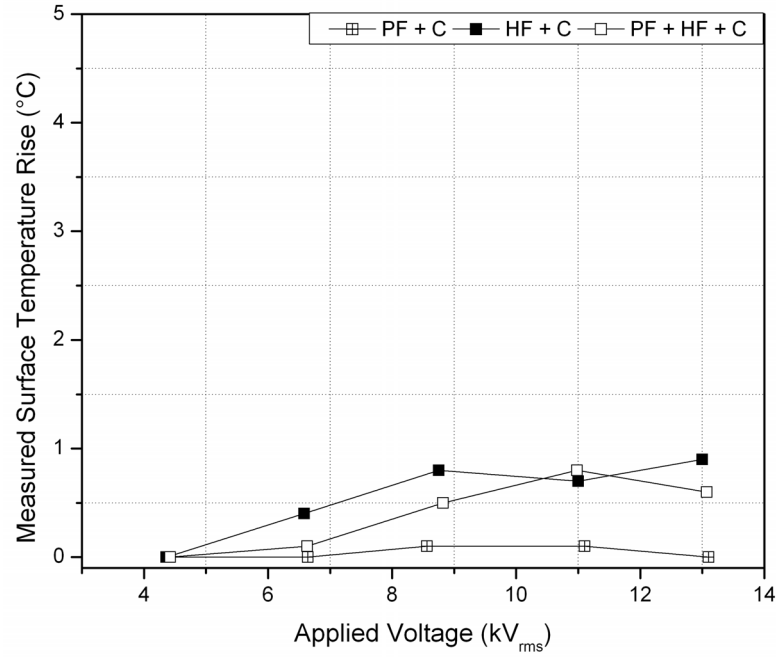
**Figure 4-16:** Maximum surface temperature rise ($T_{max}$) over ambient for test termination T-2, as a function of applied voltage, for PF, HF, and combined PF + HF stresses with current circulation (test conditions #4 - #6).
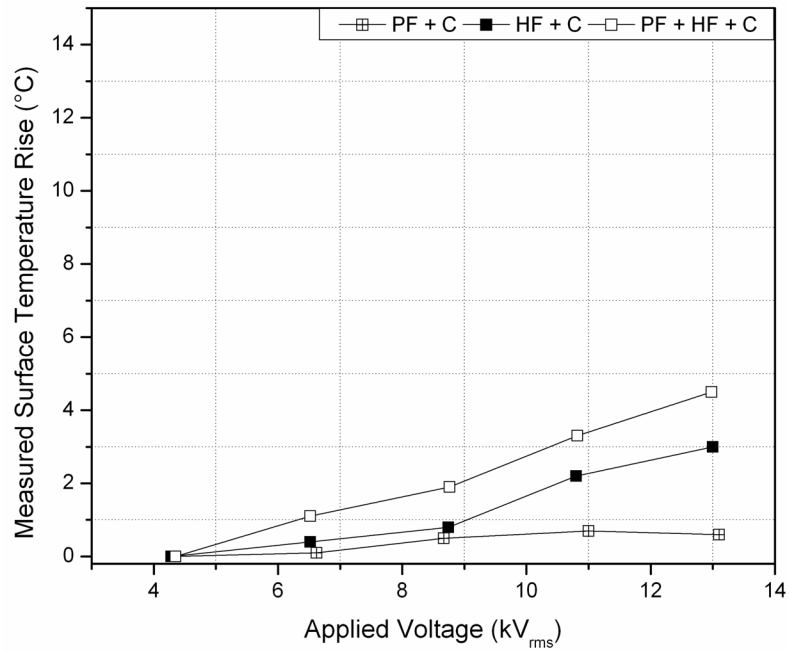


**Figure 4-17:** Maximum surface temperature rise ($T_{max}$) over ambient for test termination T-3, as a function of applied voltage, for PF, HF, and combined PF + HF stresses with current circulation (test conditions #4 - #6).

69
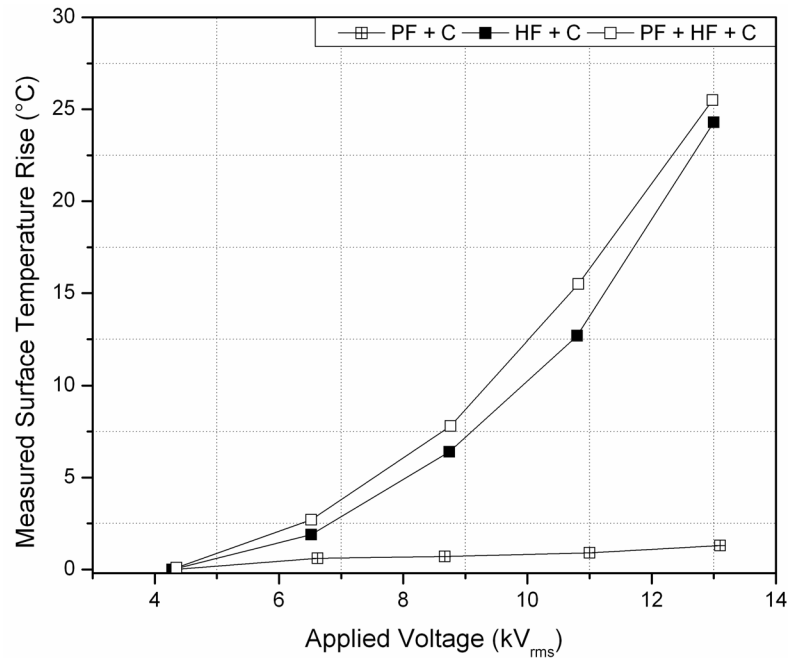
**Figure 4-18:** Maximum surface temperature rise ($T_{max}$) over ambient for test termination T-4, as a function of applied voltage, for PF, HF, and combined PF + HF stresses with current circulation (test conditions #4 - #6).
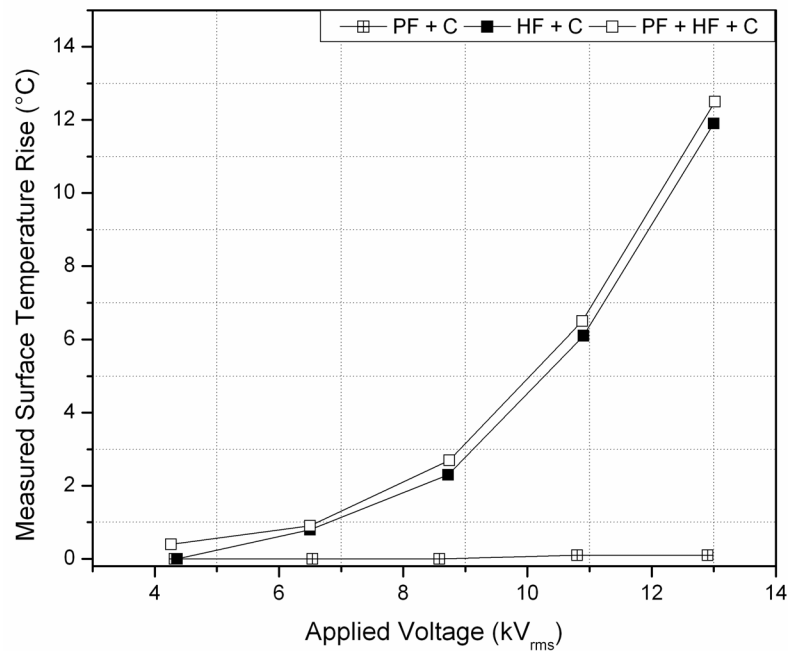


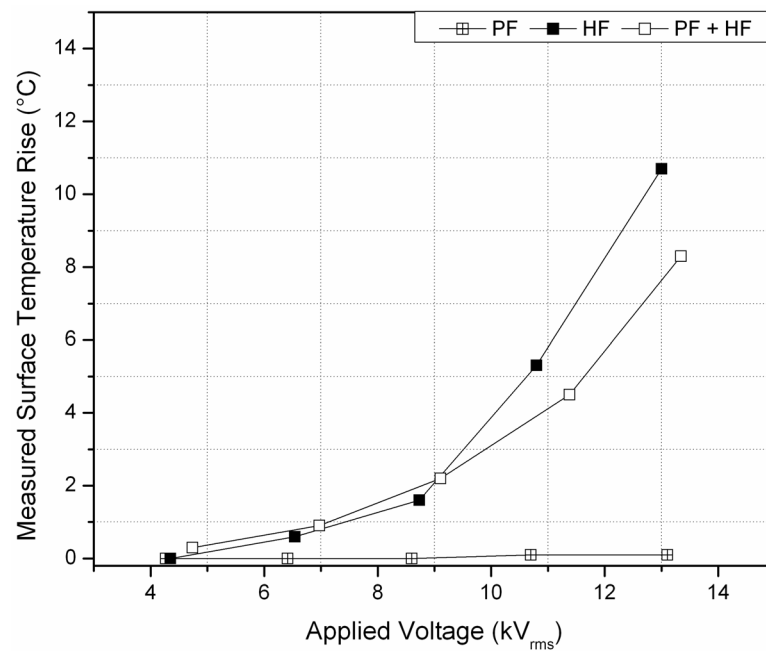**Figure 4-19:** Maximum surface temperature rise ($T_{max}$) over ambient for test termination T-5, as a function of applied voltage, for PF, HF, and combined PF + HF stresses with current circulation (test conditions #4 - #6).
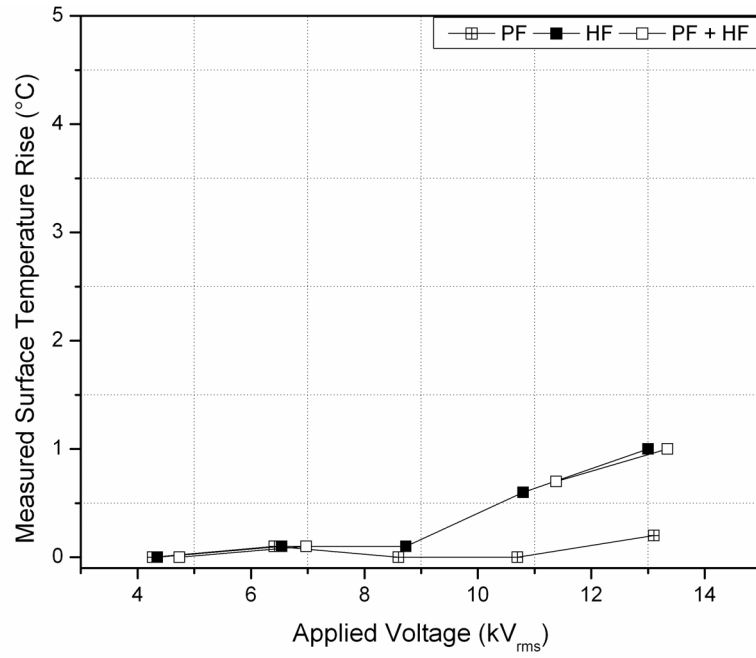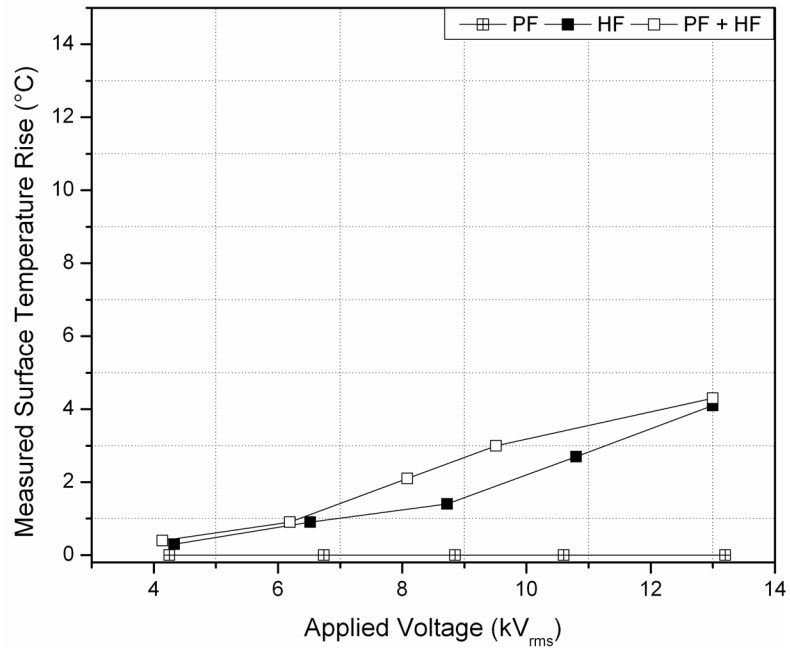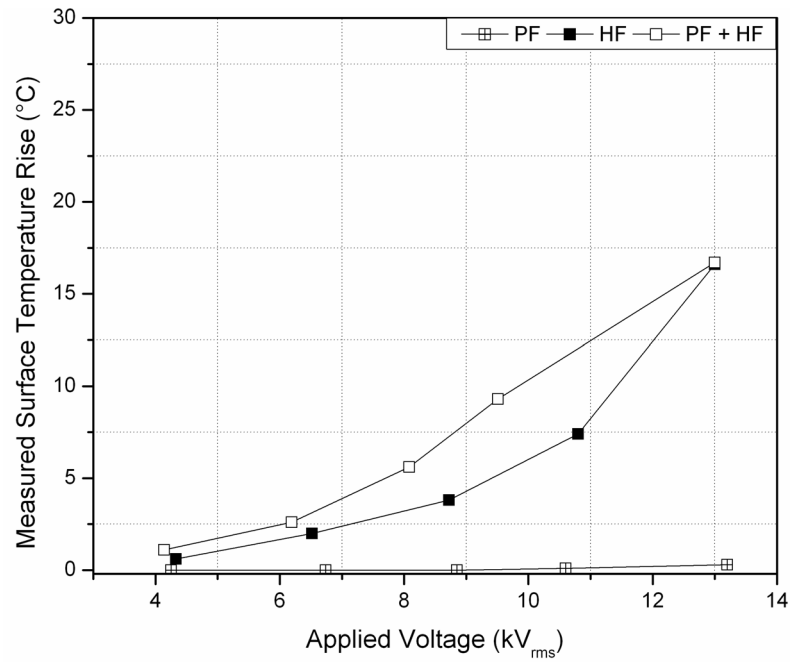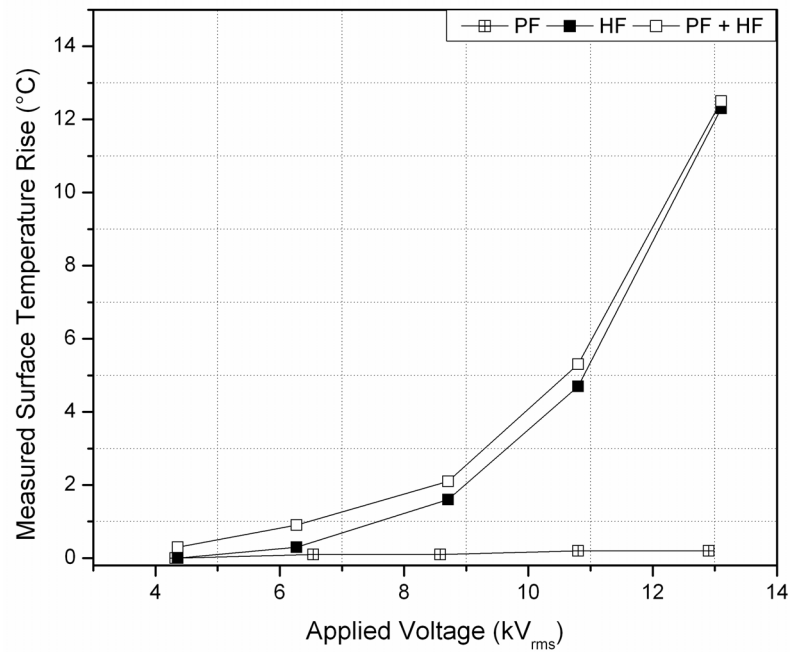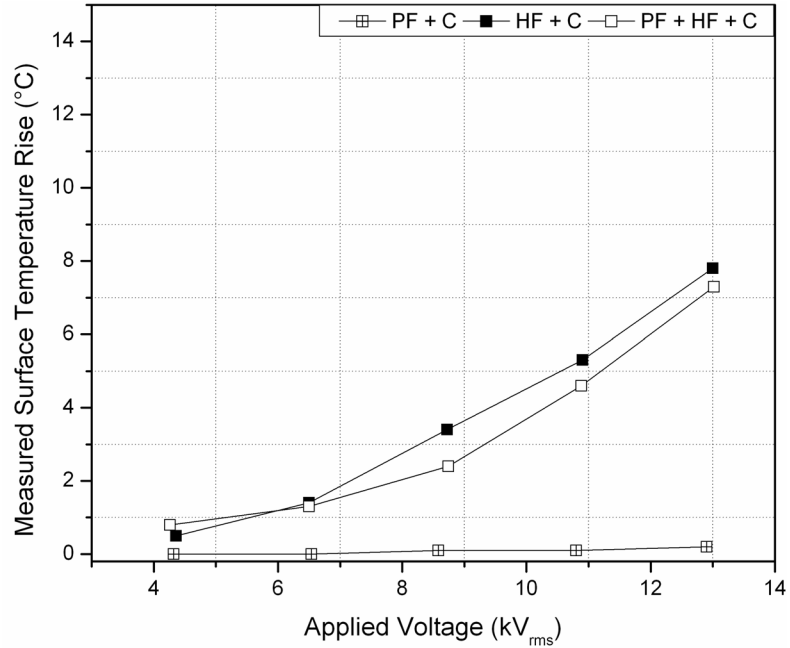
**Figure 4-20:** Maximum surface temperature rise ($T_{max}$) over ambient for test termination T-6, as a function of applied voltage, for PF, HF, and combined PF + HF stresses with current circulation (test conditions #4 - #6).

Figures 4-14 to 4-20 show that SG surface hotspots, generated during HF and PF + HF voltage application, are elevated by the increase in conductor temperature from current circulation. During PF voltage application with current circulation, Figures 4-15 to 4-20 show minimal surface temperature rise in any of the termination designs, as under PF application alone. During HF and PF + HF voltage application with current circulation, $T_{max}$ generally corresponds with measurements under voltage application alone. The primary exceptions to this are terminations T-1 and T-4. For termination T-4 above $V_{HF} = 8.7kV_{rms}$ applied voltage, $T_{max}$ is approximately 50% higher than the comparable results with voltage application alone. For T-1, the opposite is observed; $T_{max}$ above $V_{HF} = 8.7kV_{rms}$ drops by approximately 40%, as opposed to results for voltage application alone. Thus the severity of SG hotspot formation under current loading is increased in T-4, but reduced in T-1.

# Chapter 5. Discussion

This chapter discusses the FEM simulation and experimental results, presented in Chapter 4. In the first section FEM simulation results are related to theories from literature, mainly pertaining to field-dependent stress grading materials. The second part of this discussion reasons the frequency, voltage superposition, and heating effects observed in the experimental results. Lastly, an analysis of the test terminations is presented. Additional material characterization results are used to interpret the behaviour of T-3 and T-4, as these designs represent the lowest and highest recorded surface temperature rise ($T_{max}$), under high frequency stress. Details of these results, using scanning electron microscopy/energy dispersive microscopy (SEM/EDAX), are presented in Appendix D.

## 5.1. Frequency and Field-Dependent Conductivity Effects

The simulation results confirm that across all parameters studied for SG materials, high frequencies increase both electric field and resistive heating within the stress grading region. However, the maximum electric field and average resistive loss, under both PF and HF conditions, are unique and dependent on differences in the σ (E) characteristic of the SG material. Field-limiting conduction and space charge theory can be used to explain these results. Field-limiting theory has been used to explain the behaviour of non-linear dielectrics in cable termination SG materials, by Boggs et al. [40,41,42].

For a cable termination with exponential field-dependent SG conductivity, the system can be approximated with circuit theory by dividing the non-linear dielectric into cylindrical layers, assigning each layer as a capacitance and field-dependent resistance in parallel [43]. The current density flowing in the dielectric then consists of two parts, the resistive current density $J_R$ which is in phase with E, and the displacement (capacitive) current density $J_D$ which is in quadrature with E. For a sinusoidal applied voltage, the resistive current density $J_R$ is given by:

$$J_R = \sigma(E,T)E_o \sin(\omega t) = \sigma(E,T)E(t) \qquad [5.1]$$

while the displacement current density $J_D$ is given by:

$$J_D = \varepsilon(E,T)\frac{dE}{dt} = \varepsilon(E,T)\omega E_o \cos(\omega t) = j\varepsilon(E,T)\omega E(t) \qquad [5.2]$$

Although conductivity and permittivity are normally temperature dependent, within this section the dependency is not considered. Permittivity is often a weak function of field [7, 44], thus can be considered constant in equation 5.2. The remaining dependent parameter is $\sigma$ (E) which, as discussed in Section 3.1.1, can be represented as $\sigma(E)=\sigma_0\exp(\kappa*E)$.

From the above formulae, we can consider $\omega\varepsilon$ as the 'capacitive conductivity', with the same units as the resistive conductivity $\sigma$ (E) [40]. The stress grading behaviour is determined by the relative values of the resistive and capacitive current densities, thus $\omega\varepsilon$ and $\sigma$ (E). When $\omega\varepsilon$ is larger than $\sigma$ (E), the system is capacitively graded; when $\sigma$ (E) is larger than $\omega\varepsilon$, the system is resistively graded. Figure 5-1 shows a comparison between $\sigma$ (E) and E from the FEM simulations for SG-A, along with $\omega\varepsilon$ reference lines.
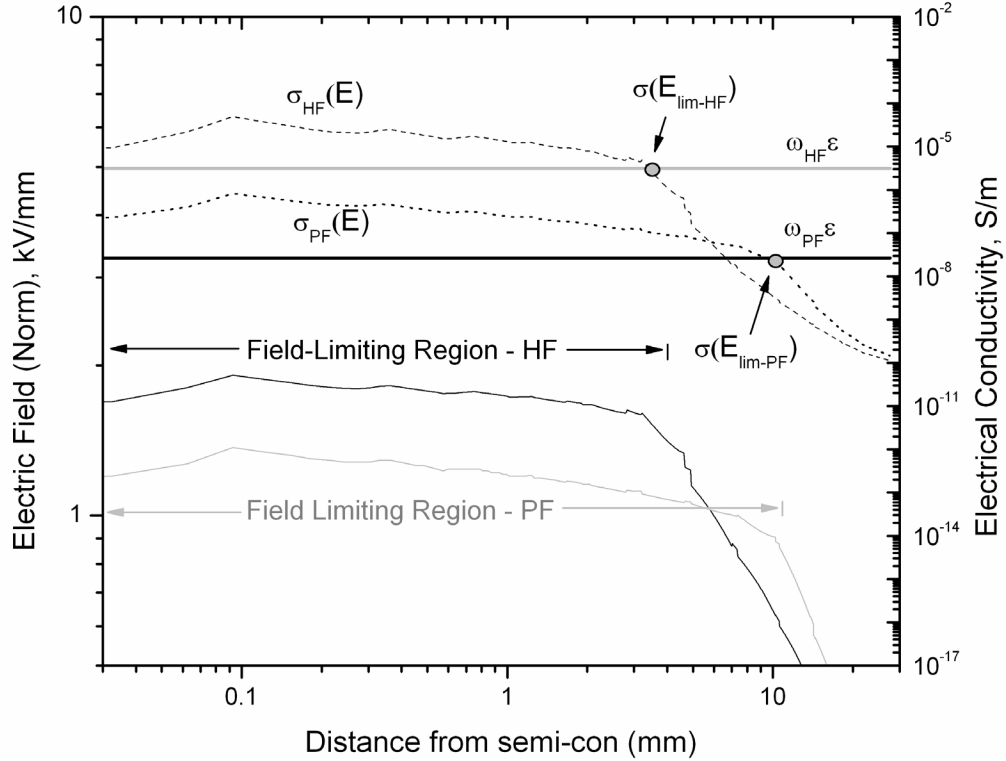


**Figure 5-1:** Comparison between $\sigma$ (E) and E, along the insulation surface. Results are from FEM simulations for SG-A with $\varepsilon_r = 8$, under $V_{L-G} = 13kV_{rms}$ and both 60 Hz and 7 kHz frequencies. Product $\omega\varepsilon$ is shown as a reference line for comparison, for 60Hz and 7 kHz.

Figure 5-1 shows that the field-dependent material SG-A has an intersection point, for each frequency, where the resistive conductivity is equal to the capacitive conductivity. This condition is expressed as $\sigma(E_{lim}) = \omega\varepsilon$, where $E_{lim}$ is the space charge limiting electric field. The basis of $E_{lim}$ is that in a highly non-uniform (Laplacian) field such as within a cable termination, space charge formation in the dielectric must limit the field because if it does not, $\sigma(E)$ will increase to an untenably high level [45]. Thus $\sigma(E)$ remains approximately constant past $\omega\varepsilon$ in the field-limiting region. The computations for SG-A in Figure 5-1 also show that $E_{lim}$ is higher for 7 kHz than 60 Hz. The reason for this increase is the need for a reduced dielectric time constant $\tau$ with increasing frequency, to promote faster redistribution of charge carriers limiting the electric field to $E_{lim}$ [43]. This condition can be formulated as $\tau = \varepsilon / \sigma(E) = 1 / \omega$, where $\omega$ is the angular frequency. Thus in order for the dielectric time constant to remain comparable to the frequency in Figure 5-1, $\sigma(E)$ must increase from $\omega_{PF}\varepsilon$ to $\omega_{HF}\varepsilon$, increasing $E_{lim}$.

Figure 5-2 shows the comparisons between $\sigma(E)$ and $\omega\varepsilon$ for sample field-dependent SG materials A to D used in this study, at both 60 Hz and 7 kHz. The exponential $\sigma(E)$ curve for each SG material clearly influences the limiting electric field, and thus $\sigma(E_{lim})$. Specifically, the exponent $\kappa$ and zero-field conductivity $\sigma_o$ shift the $\sigma(E)$ curves for each SG material. This creates a different intersection point between $\sigma(E)$ and $\omega\varepsilon$, for each SG material. From the $\omega_{HF}\varepsilon$ curve in Figure 5-2, we see in decreasing order that $E_{lim} = 2.3$, 1.8, 1.5, and 1.2 kV/mm for SG-D, B, A, and C, respectively. The results from Section 4.1.1 show that the limiting electric fields are approximately 2.5, 1.9, 1.7, and 1.4 kV/mm, for SG-D, B, A, and C, respectively. These results correspond well, especially considering the circuit theory approximations made in deriving $E_{lim}$.
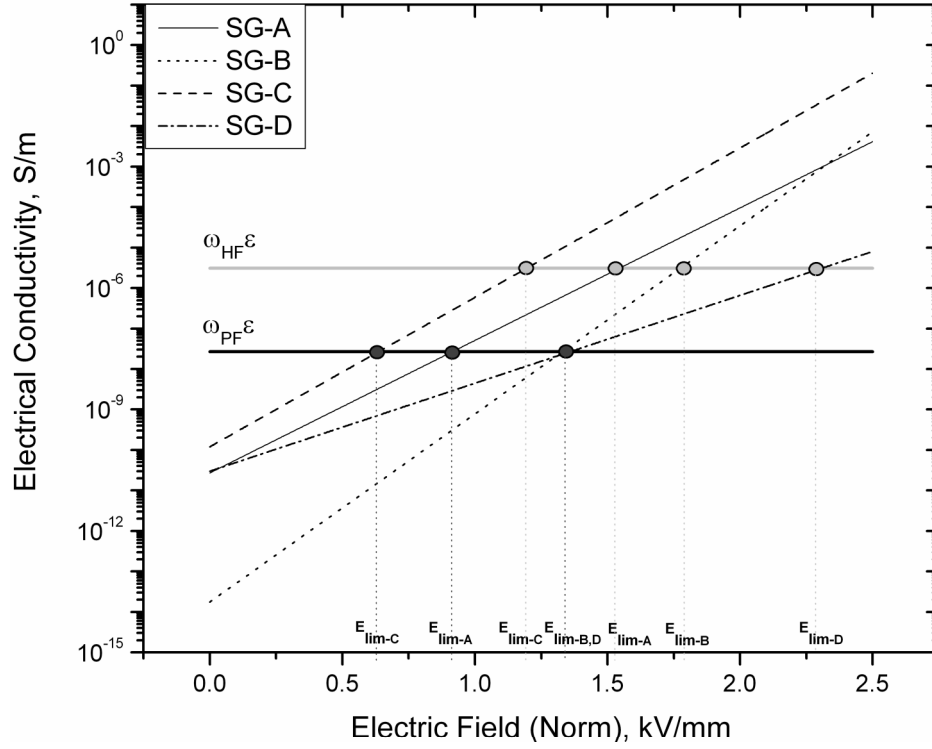
**Figure 5-2:** Comparisons between σ (E) and ωε for sample field-dependent SG materials A to D used in this study, at both 60 Hz and 7 kHz. $E_{lim}$ intersection points where σ ($E_{lim}$) = ωε are shown for each SG material.

The discussion above can be extended into resistive heating and thus termination surface temperature rise, to explain the Q and $T_{max}$ results from Section 4.1. The resistive current density $J_R$ is responsible for resistive heating in an SG material, as it is in phase with E. Since $J_R = σ(E)*E$ and the resistive power dissipation Q $= J_R E$, $Q = E^2 σ(E)$. The maximum power dissipation $Q_{max}$ thus presumably occurs at the limiting electric field, and higher $E_{lim}$ will result in higher σ (E) and $Q_{max}$. However, the average power dissipation $Q_{av} = \int Q(E,σ)ds$ determines temperature rise in the SG volume, rather than the maximum power dissipation. From the Q and $T_{max}$ simulations in Section 4.1.1, the following relationships were observed:

I. Q and $T_{max}$ for all simulated SG materials are negligible at PF, but not at HF conditions.
II. Under HF conditions, all field-dependent materials SG-A to D generate higher average power dissipation than field-independent SG-E. $T_{max}$ for SG-A to D also increases non-linearly with voltage; however, $T_{max}$ for SG-E increases linearly with voltage.

75

III. Among field-dependent materials, the highest $T_{max}$ results correspond to the material with the lowest limiting electric field and widest field-limiting region, SG-C.

Field-limiting theory can be used to explain the above relationships. Firstly, the limiting electric field and field-dependent conductivity increase with frequency, to maintain the relationship $\sigma (E_{lim}) = \omega\varepsilon$. Since $Q = E^2\sigma(E)$ an increase from PF to HF frequency increases both the maximum and average power dissipation, and ultimately $T_{max.}$ Thus for all simulated SG materials, Q and $T_{max}$ are found to be considerably high under HF conditions, but negligible at power frequencies.

Secondly, the contrasts between field-dependent materials SG-A to D and field-independent SG-E is due to the lack of field-limiting behaviour in SG-E. The field at the semi-con edge in SG-E is allowed to reach the maximum electric field determined by the applied voltage, shown in Figure 4-2 to be as high as 4.5 kV/mm. Although $E_{max}$ for SG-E is higher than in SG-A to D, the lower, constant conductivity means that the average power dissipation and $T_{max}$ will be lower for SG-E, and vary linearly with applied voltage. In the field-dependant materials, the average power dissipation and $T_{max}$ increase more than linearly with applied voltage, since the conductivity varies exponentially with E.

Lastly, Figure 5-3 shows how the average power dissipation and thus $T_{max}$ are highest for SG-C, the material with the lowest $E_{lim}$ and widest field-limiting region. At the other end, $Q_{av}$ is at a minimum for SG-D, which has the maximum limiting electric field and narrowest field-limiting region. This result shows that keeping all other parameters constant, an SG material designed to achieve a lower $E_{lim}$, using a highly non-linear $\sigma (E)$ material, will increase $Q_{av}$ and $T_{max}$ under HF stresses. Field-dependant SG design, for terminations operating in HF conditions, must thus balance between the competing objectives of limiting electric field and power dissipation.
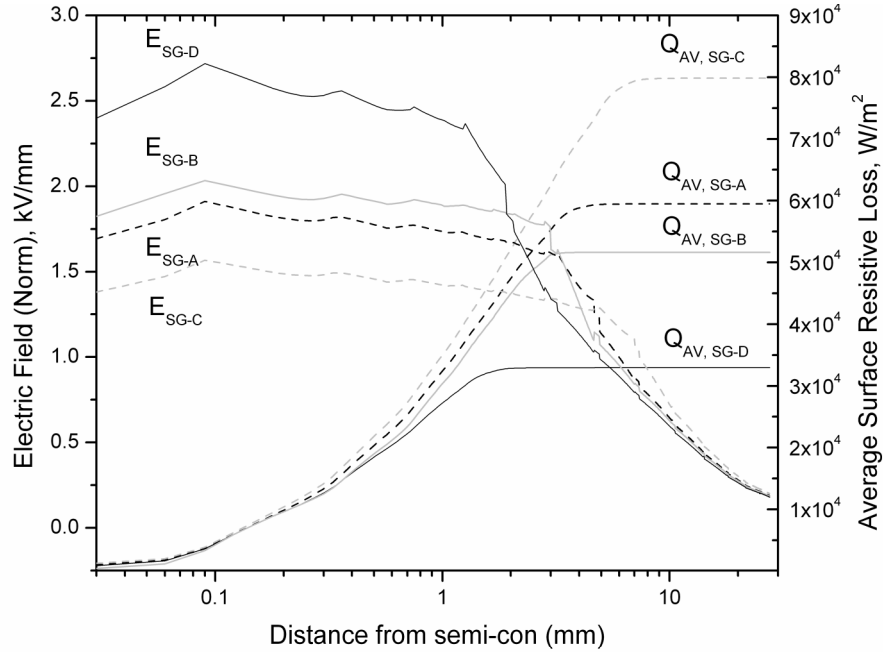
**Figure 5-3:** Electric field (E) and average resistive loss ($Q_{av}$) along the insulation surface, for simulated materials SG-A to SG-D with $\varepsilon_r = 8$, at $V_{L-G} = 13kV_{rms}$ and 7 kHz.

## 5.2. Effects of Higher Permittivity

The simulation results show that increasing the permittivity of an SG layer shortens the width of the field-limiting region; hence, reducing Q and $T_{max}$. The field limiting theory used to explain field-dependant conductivity effects cannot be applied to this phenomenon, as high-$\varepsilon$ behaviour in a multi-dielectric medium is attributable to strong dipole moments, bulk polarization, and effective relative permittivity values [12,46,47]. Increasing $\varepsilon_r$ causes linearization of the surface potential along the distance from semi-con edge (*s*), reducing *dv/ds* and thus the electric field in the same region. Figure 5-4 shows the refractive effects of changing $\varepsilon_r$ from 8 to 23 in the FEM termination model, holding all other parameters constant.
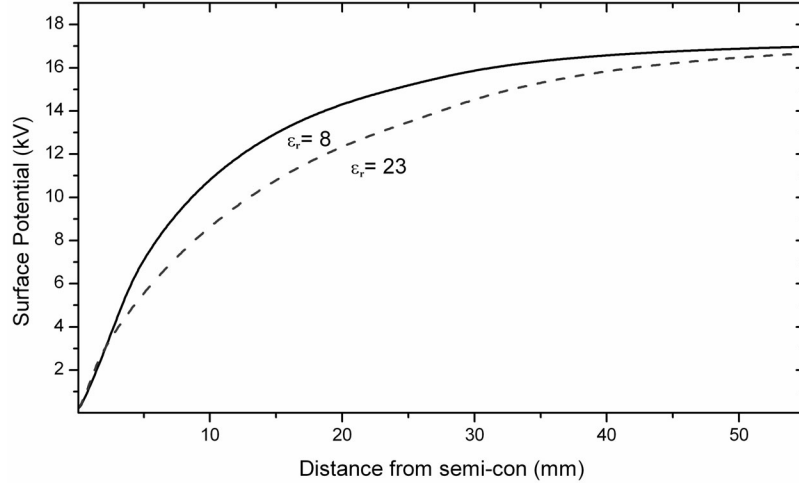
**Figure 5-4:** Effects of changing $\varepsilon_r$ from 8 to 23 in FEM model using SG-A, at $V_{L-G} = 13kV_{rms}$ and 7 kHz.

## 5.3. Geometry Effects

The results from Section 4.1.3 clearly show that the electric and thermal behaviour of geometric (stress cone) is unique from that of non-geometric (compact, field-dependant) terminations. A geometric stress cone with permittivity similar to that of XLPE capacitively grades the field, keeping $E_{max}$ at a constant level with increasing frequency, and generating negligible resistive heating and surface temperature rise. Considering electrical and thermal performance only, this type of design is thus the ideal choice for HF applications, as observed by other researchers [3,11].

Among compact designs, Figure 4-6 shows that small thickness and spatial differences have negligible effect on surface electric field, resistive heating, and temperature rise, under either power or high frequency stresses. Assuming that minimum SG lengths and thicknesses meet the power frequency and BIL design requirements, the effects of $\sigma$ (E) and $\varepsilon$ would thus be more significant than geometry variations, in compact terminations.

## 5.4. Thermal Conductivity Effects

The surface temperature simulations for SG-A show that a maximum $\pm$ 15% temperature difference, at $V_{L-G} = 13kV_{rms}$ and 7 kHz, occurs with variation of thermal conductivity between 0.6 – 1.3 W/m.K. However, the effects of k become less significant at the outer housing rather than inner insulation surface, due to the temperature drop between $T_{max\_in}$ and $T_{max\_out}$. Lastly, at a higher permittivity of $\varepsilon_r = 23$, the variability of $T_{max\_in}$ and $T_{max\_out}$ with

78

k becomes further negligible. The simulation results show that the temperature rise effects of σ (E) and ε dominate the effects of altering thermal conductivity, and should thus govern termination design for high frequency conditions.

## 5.5. Analysis of Test Results

The discussions herein assume that the non-geometric test terminations in this study, T-1 and T-3 to T-6, utilize varying degrees of non-linear field-dependant SG conductivity. The data from Table 2-2 confirms the use of non-linear conductivity fillers in designs T-1, T-5, and T-6. For T-3 and T-4 an assumption of field-dependant conductivity, in addition to their known high-permittivities, is valid due to their compact nature.

### 5.5.1. Frequency Effects

From Section 4.2, all test terminations showed negligible temperature increase under PF conditions within the test voltage range. Under HF and superimposed PF + HF conditions however, all terminations except for T-2 showed non-linearly increasing surface temperature with applied voltage. As discussed in Section 5.3, resistive heating and thus $T_{max}$ in geometric design T-2 is expected to be negligible and insensitive to frequency.

For non-geometric terminations T-1 and T-3 to T-6, the increase in surface temperature rise with frequency corresponds with the limiting electric field and resistive heating concepts presented in Section 5.1. The comparative magnitudes and non-linearity of $T_{max}$ among terminations likely vary due to the unique $\sigma(E)=\sigma_0 \exp(\kappa^* E)$ characteristic for each material, and to a lesser degree on the SG material thermal conductivity.

### 5.5.2. Effects of Superimposing Power and High Frequency Voltages

The experimental results from Section 4.2 generally show a strong similarity in surface temperature rise between high frequency and superimposed power and high frequency conditions. T-1 is the only design to show a 15 – 20% drop in $T_{max}$ between HF and PF + HF conditions, above an applied voltage of 8.7kV$_{rms}$. Without σ (E), ε (E), and thermal conductivity values for the T-1 SG material, this particular result cannot be explained.

Equal or slightly increased values of $T_{max}$ for PF + HF versus HF conditions are expected in terminations with field-dependent SG materials, despite the large increase in peak applied

voltage under PF + HF conditions. This is since $E_{lim}$ is dependant on the effective frequency ω, rather than peak value of the applied voltage [45]. The effective frequency for the superimposed PF + HF waveform is still approximately 7 kHz; hence the limiting electric field, resistive heating, and surface temperature rise under PF + HF conditions should all remain as under HF conditions, within the SG field-limiting region.

The above results have two implications: firstly, a high frequency waveform can be used independently to test components operating under potential PF + HF harmonic conditions, simplifying experimental setups. Secondly, although the high peak value of the PF + HF voltage may cause cable insulation accelerated ageing [48], the use of field-dependent SG materials will limit the electric field near the semi-con cutback, to the same levels as if the HF voltage were alone present.

## 5.5.3. Current Circulation (Heating) Effects

The current circulation tests presented in Section 4.2.2 show a range of temperature effects among designs T-1 to T-6. In cases such as T-4, $T_{max}$ increases up to 50% versus under ambient conditions, whereas in others such as T-2, $T_{max}$ decreases up to 40%. All test terminations show however that the severity of HF induced surface temperature rise is increased during actual conductor loading, since $T_{max}$ under ambient HF conditions is elevated by the increase in conductor temperature from current circulation.

From these results a temperature dependence of termination materials is proposed, which can be attributed to conductivity, thermal expansion, or permittivity changes with temperature. The temperature-dependent term in $\sigma$ (E,T) from equation 5.2 has been found to obey the relationship exp (-Φ/ ($k_B$T)), where Φ is the material activation energy, $k_B$ is Boltzmann's constant, and T is the absolute temperature [42, 49]. Thermal expansion of the material can slightly decrease thermal conductivity k for SG materials with conductive fillers [50]. This is due to the composite thermal conductivity decreasing with thermal expansion, and lower transmittance of thermal vibrations through widened polymer filler conductive chains [50]. Lastly, composite SG materials may exhibit positive temperature coefficients in permittivity, as recorded in SG materials with SiC and carbon black fillers [51].

From the above theories, positive temperature dependence of $\sigma$ (E,T) and thermal expansion may be a likely cause of experimental $T_{max}$ increase in T-4, holding frequency

constant. The temperature drop in T-2 may be attributable to a positive temperature coefficient in permittivity. In this type of SG material a temperature-induced increase in permittivity would increase the capacitive grading, decreasing resistive heating and $T_{max}$.

## 5.6. Test Termination Analysis

The experimental surface temperature rise results for test terminations T-1 to T-6 are compared in Table 5-1. The terminations are ranked with respect to $T_{max}$ when subjected to $V_{L-G} = 13kV_{rms}$ at 7 kHz, without current circulation. The results show that under the HF test conditions used in this research, terminations T-4 and T-3 exhibited the highest and lowest $T_{max}$ respectively, among tested non-geometric designs. As such, material characterization tests were conducted on the SG material of T-3 and T-4, and a comparison was made between experimental T-3 and T-4 surface temperature rise and FEM simulations.

**Table 5-1:** Comparison of surface temperature rise results for test terminations T-1 to T-6, ranked relative to $T_{max}$ at $V_{L-G} = 13kV_{rms}$ and 7 kHz, without current circulation.

| Termination | Installation Type | Maximum Surface Temperature Rise $T_{max}$, @ $1.5V_{L-G}$, 7 kHz) | Maximum Surface Temperature Rise $T_{max}$, with Current @ $1.5V_{L-G}$, 7 kHz) | Predicted Stress Grading Characteristics |
|---|---|---|---|---|
| T-4 | Cold-Shrink | 16.6°C | 24.3°C | Resistive-Capacitive |
| T-5 | Cold-Shrink | 12.3°C | 12°C | Resistive |
| T-1 | Slip-Over | 10.7°C | 6.5°C | Resistive-Capacitive |
| T-6 | Heat-Shrink | 8°C | 8°C | Resistive |
| T-3 | Cold-Shrink | 4°C | 3°C | Capacitive (Compact) |
| T-2 | Stress-Cone | 1°C | 1°C | Capacitive (Geometric) |

### 5.6.1. Stress Grading Characterization for Test Terminations T-3 and T-4

The summary of T-3 and T-4 material characterization results is listed below, and used herein to explain the unique behaviour of designs T-3 and T-4. Detailed SEM/EDAX results are presented in Appendix D.

    I.   The SG material for termination T-3 is likely barium titanate ($BaTiO_3$).

   II.   The T-4 outer SG shows the presence of pure aluminum (Al) and likely $BaTiO_3$.

  III.   The T-4 inner SG shows the presence of $BaTiO_3$.

  IV.   Any of the layers may contain carbon black filler (CB).

It is reported that ceramic fillers such as $BaTiO_3$ and metal powders have been used for increasing relative permittivity in insulating materials [12]. Furthermore, the ferroelectric ceramic $BaTiO_3$ shows varying degrees of field-dependent permittivity depending on filler particle size, shape, and concentration [52]. $BaTiO_3$ has thus been investigated for stress grading applications as an alternative to field-dependent conductive fillers, where the permittivity is instead enhanced in high fields [53,54]. Metal powder additions in polymers can also yield higher relative permittivity composites, however with a corresponding increase in conductivity; $BaTiO_3$ + Al has been listed as one such example [12].

Considering these points, it is likely that the high-permittivity characteristic of termination T-3 is due to the ferroelectric ceramic filler $BaTiO_3$, and that the low surface temperature rise of T-3 under HF stresses is due to a combination of the following:

I. High and field-dependent permittivity from $BaTiO_3$ filler, decreasing the electric field, resistive heating, and surface temperature rise in the high stress SG region. The presence of $BaTiO_3$ may achieve stress relief requirements on its own, alleviating the need for non-linear conductive fillers.

II. Low concentration of conductive filler and lower conductivity exponent $\kappa$ for the SG material, assuming the use of field-dependant conductive fillers. These characteristics would increase the limiting electric field near the semi-con screen, but reduce the average resistive heating as discussed in Section 5.1.

For termination T-4, the high surface temperature rise under HF stress may be attributable to a combination of the following:

I. Aluminum metal fillers in addition to $BaTiO_3$, to achieve a high-permittivity SG composite. In this case, the conductivity of the SG material would be much greater than that for T-3, especially if combined with fillers such as carbon black near the percolation threshold. This would create high $T_{max}$ under ambient and elevated temperature conditions, since the higher conductivity may also be more temperature dependent.

II. Lower or lack of field-dependent permittivity in SG composite. This could be due lower filler concentration or larger (coarser) grain size of $BaTiO_3$ particles [52], used to achieve high permittivity in T-3. A lower degree of field-dependent permittivity in T-3 would decrease the refractive stress relief in the SG high-field region, causing the conductive behaviour to dominate.

## 5.6.2. Comparison of Measured and Simulated Maximum Surface Temperature Rise for Terminations T-3 and T-4

Figure 5-5 shows the FEM $T_{max\_out}$ simulations for SG-C and SG-D, and the experimental $T_{max}$ measurements for terminations T-3 and T-4, respectively. Although field-dependent permittivity was not considered in the FEM simulations, Figure 5-5 shows that constant high permittivity, and highly non-linear (SG-C) versus less non-linear (SG-D) conductivity, can alone reason the experimental surface temperature results for T-3 and T-4. The good correlation between measured and simulated results lends validity to the FEM simulations, and the SG material characteristics hypothesized in Section 5.6.1 for terminations T-3 and T-4. The results also demonstrate that FEM software can be used to effectively analyze the behaviour of field-dependent and field-independent SG materials, under HF conditions. This is particularly important since no instruments exist which allow direct measurements of surface potential, electric field, or internal resistive heating, under HF or combined PF + HF stress application. Thus if accurate representations for SG material thermal conductivity, $\sigma$ (E, T), and $\varepsilon$ (E, T) are known, experimental surface temperature results can be correlated with FEM simulations for further analysis.
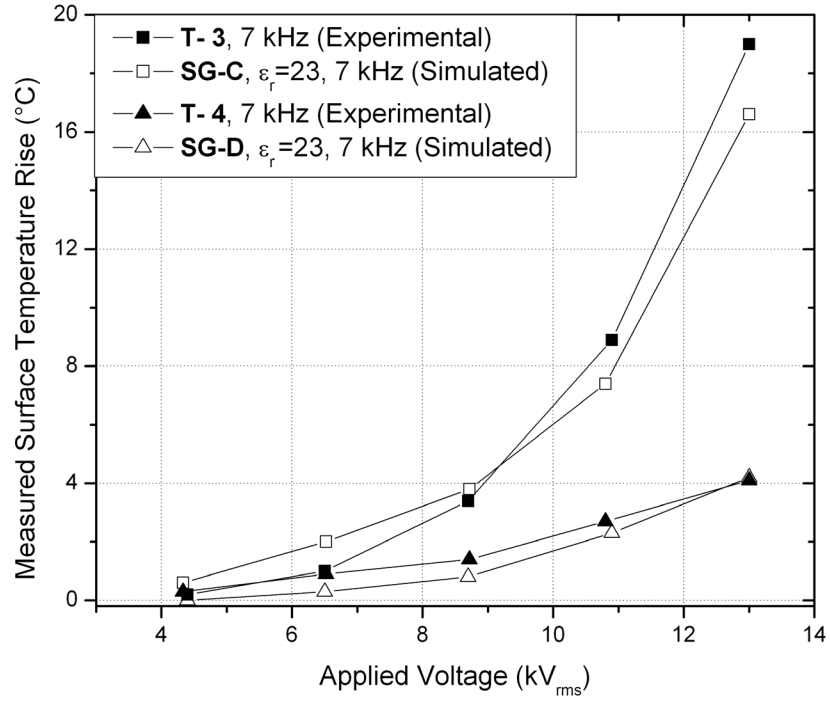
**Figure 5-5:** Comparison between FEM $T_{max\_out}$ simulations for SG-C and SG-D, and experimental $T_{max}$ measurements for terminations T-3 and T-4. Frequency is 7 kHz, and simulated SG material $\varepsilon_r = 23$.

# Chapter 6. Summary, Conclusions and Future Work

## 6.1. Summary and Conclusions

This present work was undertaken to study high frequency effects on XLPE cable terminations, and their relationship to SG design and material properties. The primary objective of this analysis was to determine optimum design characteristics for MV, compact terminations operating in environments where HF harmonics may occur.

The initial chapter reviewed knowledge to date on HF harmonics in VSC systems, MV cable terminations and their susceptibility to HF harmonics, and testing techniques to replicate HF resonance field conditions. Following this, the preparation of six MV termination samples was discussed, including an overview of known SG characteristics for the commercial test samples. The six unique designs were then experimentally analyzed for temperature increase under PF, HF, and superimposed PF + HF voltage conditions. Further analysis was carried out with current circulation, to test the additional effect of heating from load current. These analyses were conducted using a HV, HF experimental setup, designed to create test conditions representative of high frequency harmonic resonance in a VSC system. Concurrent to the experimental work, simulations were conducted using FEM methods to analyze electric field (E), resistive heating (Q), and maximum surface temperature rise ($T_{max}$) in model terminations, in response to variations in applied voltage amplitude, frequency, and SG material parameters. Finally study results were presented and discussed, which revealed a wide variation in temperature gradients among modeled and tested terminations, under HF conditions. Furthermore, these variations were found to be primarily dependent on the termination SG design method and material properties.

From the work done in this thesis, the following main conclusions can be drawn:

1. FEM software (COMSOL Multiphysics$^{TM}$) can been used to analyze the behaviour of cable terminations field-dependant and independent SG materials, under HF conditions. Computed maximum temperature rise ($T_{max}$) correspond with trends observed experimentally, and in literature.

2. Experimental waveforms replicating conditions of PF + HF harmonic resonance conditions can be suitably generated with a HV series resonance circuit, using a commercially available high frequency audio amplifier.

3. Terminations using geometric (stress-cone) SG methods are insensitive to high frequency harmonics. Among non-geometric (compact) designs, wide variations in thermal behaviour exist under HF conditions, attributable to differences in material properties of commercial SG materials. Under current circulation, thermal hotspots from HF resistive heating remain and in some cases increase; this is attributable to temperature dependencies of SG material properties.

4. High frequency voltage application increases the electric field and resistive heating in all non-geometric termination designs. Among terminations using field-dependent SG materials, the electrical conductivity $\sigma(E)$ and permittivity strongly influence the limiting electric field ($E_{lim}$), average resistive heating ($Q_{av}$) and $T_{max}$ in the SG region. Stress grading materials with higher conductivity constants $\sigma_0$ and $\kappa$ generate lower and wider field-limiting regions, higher $Q_{av}$, and thus higher $T_{max}$ under HF conditions. Field-independent materials ($\kappa = 0$) have lower, linear temperature rise, but no advantages of field-limiting behaviour. Increasing SG electrical permittivity generates lower $Q_{av}$ and $T_{max}$ under HF conditions, holding conductivity constant.

5. Thermal hotspots in cable termination SG areas may lead to material degradation, partial discharges, and eventually flashover failure, as discussed in Section 1.3.3. As such, the following recommendations are made regarding optimal non-geometric termination SG characteristics, for application in HF harmonic conditions:

   a. Stress grading materials using metal fillers to achieve high-permittivity are non-ideal candidates for application in high frequency harmonic conditions. Test termination T-4 is most likely of this type, with SEM/EDAX results showing aluminum particles in addition to high-permittivity fillers. Experimental results for T-4 show the highest $T_{max}$ under HF and PF + HF conditions, further aggravated with circulation current.

86

b. Stress grading materials using field-dependent permittivity and low conductivity fillers for field control are potentially ideal candidates for application in HF harmonic conditions. Test termination T-3 is most likely of this type, with SEM/EDAX suggesting the presence of ferroelectric filler $BaTiO_3$. Experimental results for T-3 show the lowest $T_{max}$ under HF and PF + HF conditions, with and without circulation current.

## 6.2. Suggestions for Future Work

The following section gives suggestions for future work, focusing on experimental long term studies, HF test setup improvements, SG material property measurement, optimum SG material development, and extended applications.

To study the material degradation effects of HF electric field amplifications and SG temperature rise, long-term ageing experiments are suggested for test terminations T-1 to T-6. The terminations should at minimum be subjected to the power frequency, high frequency and combined PF + HF tests, with and without circulation current, used in this research. Additionally however, the tests should include temperature cycles to initiate thermal-mechanical expansions at interfaces. As well as comparing HF degradation among designs, these studies would also reveal any lifetime differences under HF stress due to unique installation methods; for example the silicone compound applied in terminations T-1 and T-3 is susceptible to drying out in hotspot/high field regions, increasing the risk of PD and eventual failure [8].

For the experimental setup, a higher power, high frequency source is suggested to replace the commercial T8000 amplifier used in this research. The design of the new source should use the tesla resonant transformer principle or variable speed generation, as has been successfully applied by other researchers [3,27]. The generator should allow for a HF testing range up to 20 kHz. This would not only test for higher switching frequency harmonics in VSC-based transmission systems, but also accelerate long-term ageing of terminations due to increased high frequency electric field amplification and resistive heating.

A wide variation of temperature gradients in test terminations has been observed in this research, under HF conditions. To understand the fundamentals of this behaviour, experimental measurements of electrical conductivity, permittivity, and thermal conductivity

are suggested for SG materials used in commercial terminations T-1 to T-6. The electrical conductivity and permittivity measurements should account for electric field and temperature dependence, thus yielding $\sigma$ (E, T) and $\varepsilon$ (E, T). With these parameters, accurate FEM modeling can be undertaken to interpret the HF experimental behaviour for T-1 to T-6, including elevated temperature conditions. The SG material property measurements may involve developing special guarded electrode arrangements for non-uniform SG geometries, if samples are to be taken from actual terminations.

Pending the results of long-term ageing tests, SG materials should be experimentally developed for application to cable terminations operating in HF environments. The focus could be on field-dependent high permittivity and low conductivity SG materials, such as composites using ferroelectric filler $BaTiO_3$. Additionally, SG materials using conductive metal fillers to achieve high permittivity could be developed and tested under high frequency stresses, to compare against the conclusions of this thesis.

Finally, a field-dependant SG material designed for optimal thermal and electrical performance, under HF stresses, may improve impulse in addition to HF harmonic performance. Under lightning impulse conditions for example, peak voltage can be nearly 10 times greater than power frequency conditions, and effective frequency is around 300 kHz [45]. The dielectric system normally remains stable since impulses occur rarely, and the large resistive heating occurs over very short duration [43]. However, non-geometric (compact) terminations have thus far been limited to system voltages less than $V_{L-L}$ = 69kV$_{rms}$. According to a termination manufacturer, this limitation is in part to due to the over-heating of thin SG layers under high BIL. Thus an SG material optimized for HF conditions, should be studied and laboratory tested for feasibility in higher voltage (> 69kV$_{rms}$) compact termination designs.

# Appendix A: Worldwide VSC-based Transmission Installations

| Commission Date | Project | Real or Reactive Power / DC Voltage / AC Voltage(s) | Installation Type | Manufacturer | Purpose |
|---|---|---|---|---|---|
| 2010 | Trans Bay Cable, USA | 400 MW / ± 200 kVdc / 115, 230 kVac | HVDC 'Plus' | Siemens | Submarine connection for urban center supply |
| 2009 | Caprivi Link Interconnector, Namibia | 300 MW / 350 kVdc / 400, 330 kVac | HVDC 'Light' | ABB | Stabilization of weak networks, long distance O/H transmission |
| 2009 | NORD E.ON 1, Germany | 400 MW / ±150 kVdc / 154, 380 kVac | HVDC 'Light' | ABB | Long distance off-shore wind farm connection |
| 2009 | Valhall offshore, Norway | 78 MW / 150 kVdc / 300, 11 kVac | HVDC 'Light' | ABB | Offshore oil platform connection |
| 2006 | Estlink, Estonia – Finland | 350 MW / ±150 kVdc / 330, 400 kVac | HVDC 'Light' | ABB | Long-distance submarine connection of asynchronous AC systems |
| 2005 | Troll offshore, Norway | 84 MW / ±60 kVdc / 132, 56 kVac | HVDC 'Light' | ABB | Offshore gas production platform connection |
| 2004 | Holly, USA | -80 to +110 MVar / 138 kVac | SVC 'Light' | ABB | Reactive power support |
| 2003 | Kangjin, Korea | ± 40 MVar / 154 kVac | Unified Power Flow Controller (UPFC) | KEPCO, Siemens | Reactive compensation for contingency conditions |
| 2003 | Glenbrook, Conneticutt | ± 75 MVar / 115 kVac | STATCOM | ALSTOM | Reactive compensation for contingency conditions |
| 2002 | CrossSound, USA | 330 MW / ±150 kVdc / 345, 138 kVac | HVDC 'Light' | ABB | Submarine connection for controlled power exchange |
| 2002 | Murraylink, Australia | 220 MW / ±150 kVdc / 132, 220 kVac | HVDC 'Light' | ABB | Merchant land link |
| 2002 | SDG&E Talega, USA | ± 100 MVar / 138 kVac | STATCOM | Mitsubishi | Dynamic reactive compensation at peak loading |
| 2001 | Marcy, USA | ± 200 MVar / 345 kVac | STATCOM | EPRI & Siemens | Increased power transfer |
| 2001 | East Claydon, UK | ± 75 MVar / 400 or 275 kVac | STATCOM | ALSTOM | Relocatable reactive power compensation |
| 2001 | VELCO Essex, USA | -41 to +133 MVar / 115 kVac | STATCOM | Mitsubishi | Reactive compensation for contingency conditions |
| 2000 | Terranora interconnector, Australia | 180 MW / ±80 kVdc / 110, 132 kVac | HVDC 'Light' | ABB | Merchant power exchange, connection of asynchronous systems |
| 2000 | Eagle Pass, USA | 36 MW / ±15.9 kVdc / 132 kVac | HVDC 'Light' | ABB | Asynchronous back-to-back connection of weak systems |
| 2000 | Tjaereborg, Denmark | 7 MW / ±9 kVdc / 10.5 kVac | HVDC 'Light' | ABB | Demonstration for wind power connection |
| 1997 | Inez Station, USA | ± 160 Mvar / 138 kVac | UPFC | AEP, EPRI & Westinghouse | Voltage support and power flow control |
| 1997 | Hellsjön, Sweden | 3 MW / ±10 kVdc / 10 kVac | HVDC 'Light' | ABB | Test transmission |
| 1996 | Sullivan, USA | ± 100 Mvar / 161 kVAc | STATCOM | TVA, EPRI & Westinghouse | Voltage Control |
| 1991 | Inuyama, Japan | ± 80 MVar / 154 kVac | STATCOM | KEPCO & Mitsubishi | Dynamic Stability, increased transmission capacity |

**Table A-1:** Listing and main characteristics of worldwide transmission VSC installations

# Appendix B: Circuit Protection and HV Safety

The superposition experimental setup described in Section 3.3.2 incorporated protection systems and HV safety interlock systems, for use in both short-term experiments and future long-term HF insulation ageing studies. Figure B-1 shows the protection scheme incorporating the PF transformer, current transformer, HF amplifier, and HF function generator. The HF Amp U/C (under-current) relay shown was used to detect a loss of input current to the HF amplifier, signifying a shut down of the HF amplifier. In this scenario, the U/C relay (03) would switch off the 3-pole contactor and consequently the experimental setup. Although this feature was not used in this study, it enables the remote-control of future ageing experiments, through control of the network-enabled HF amplifier. Figure B-2 shows the HV safety interlock scheme, which relates the safety interlock, HF amplifier U/C, PF transformer O/C, and leakage O/C switch contacts to the main 3-phase contactor source power (02/CC).
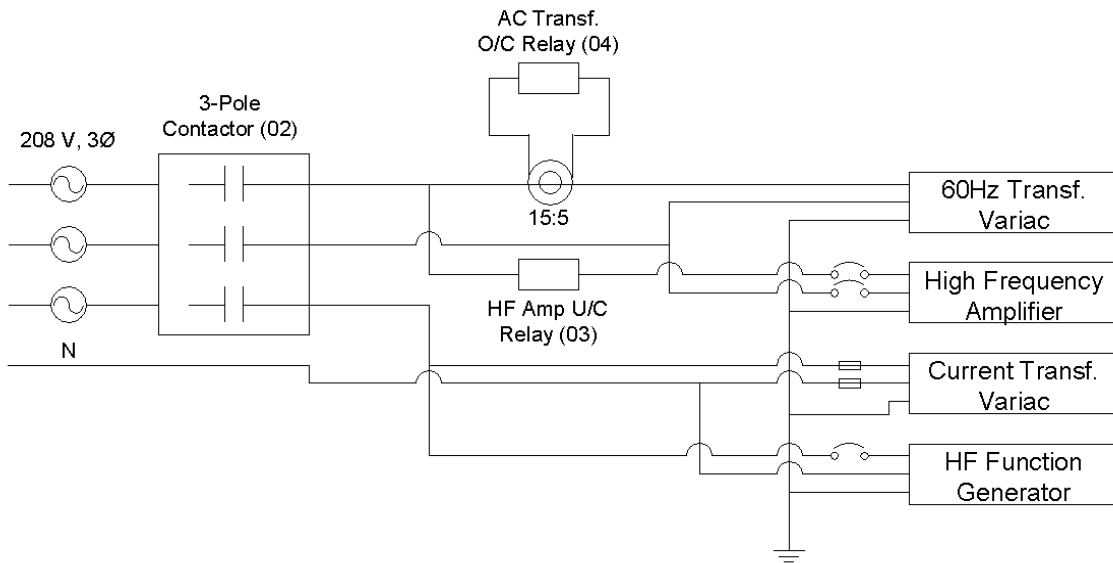


**Figure B-1:** Protection scheme for the 60Hz transformer, current transformer, HF amplifier, and HF function generator. Relay 04 detects over-current in the PF transformer, and relay 03 detects under-current in the HF amplifier. 3-pole contactor (02) shuts down superposition circuit when triggered off.
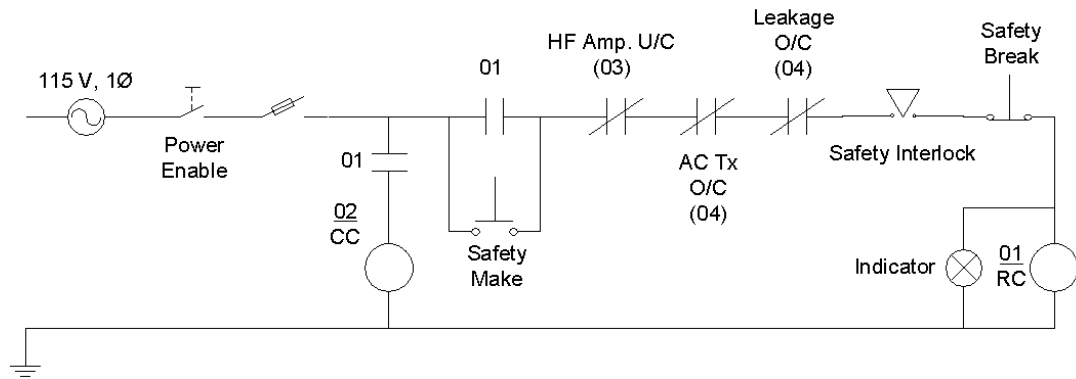
**Figure B-2:** HV safety interlock scheme for superposition circuit. Contacts 03, 04, and 02 are for corresponding relays shown in Figure B-1. Safety and leakage O/C contacts correspond to HV setup door interlock switch and leakage current relays (not shown), respectively.

# Appendix C: Leakage Current Diagnostic Measurements

Since the experimental setup was developed for both short-term testing and long-term accelerated ageing tests, shunt resistors for real-time leakage current measurement were incorporated into the design. If any degradation were to occur in either of the paralleled terminations under sustained HF stresses, monitored leakage currents would expectedly increase with ageing time. The schematic connection of the shielded, coaxially connected shunt resistors is shown in Figure 3-5, and the physical layout in Figure C-1. Despite the availability of high-frequency current transformers, shunt resistors were used due to their high sensitivity levels and availability. For example, the highest sensitivity Bergoz$^{TM}$ E5.0 CT gives a resolution of 2.5 V/A in a 50Ω oscilloscope impedance [55]. When applied to cable termination leakage currents as low as a few milliamps at 60Hz, this results in output voltages of a few millivolts. In contrast, the shunt resistors shown in Figure C-1 have calibrated resistances varying around 10Ω. This gives minimum output voltages 4x greater than for the Bergoz E5.0. Additionally, shunt resistances were available from laboratory HV impulse generators, avoiding the cost of purchasing high-sensitivity current transformers.
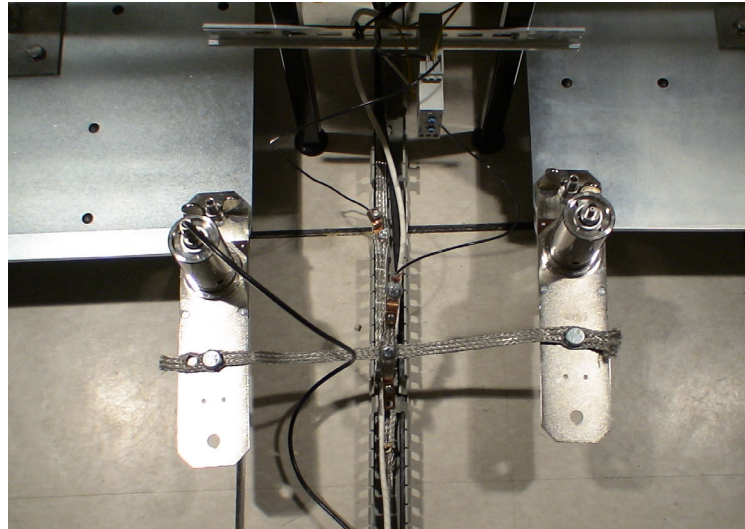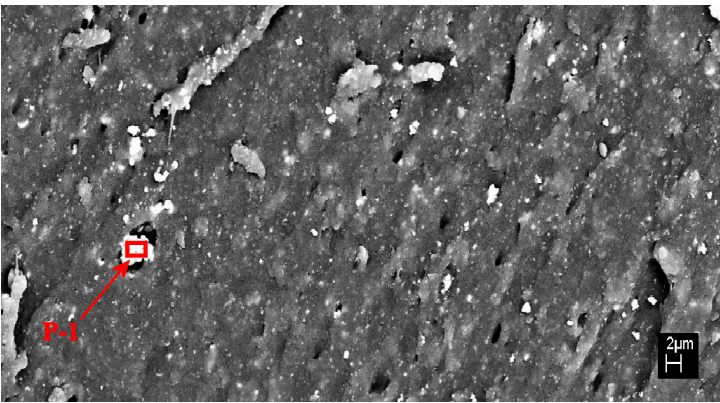


**Figure C-1:** Physical layout of shunt resistors used for leakage current measurement in test terminations; location of resistors in superposition circuit is shown in Figure 3-5.

# Appendix D: Scanning Electron Microscopy / Energy Dispersive Spectroscopy (SEM/EDAX) Characterization of Stress Grading Materials

## D.1. Characterization of Termination T-3 Stress Grading Material

Figure D-1 (a) shows an SEM image of the termination T-3 stress grading material. The corresponding EDAX results for the whole material and P-1 particle (marked) are shown in Figures D-1 (b) and (c), respectively. The sole known characteristic of this SG material is that it is 'high permittivity,' however the exact value of $\varepsilon_r$ is not known. It is notable that since gold is used in the preparation of samples for SEM, the presence of gold (Au) in the EDAX emission spectra is due to sample preparation, rather than material composition.



(a)



| Element | Wt% | At% |
|---------|-------|-------|
| C K | 75.51 | 90.50 |
| O K | 5.76 | 5.19 |
| AlK | 0.50 | 0.27 |
| SiK | 3.24 | 1.66 |
| AuM | 8.62 | 0.63 |
| TiK | 4.46 | 1.34 |
| ZnK | 1.91 | 0.42 |

(b)

93
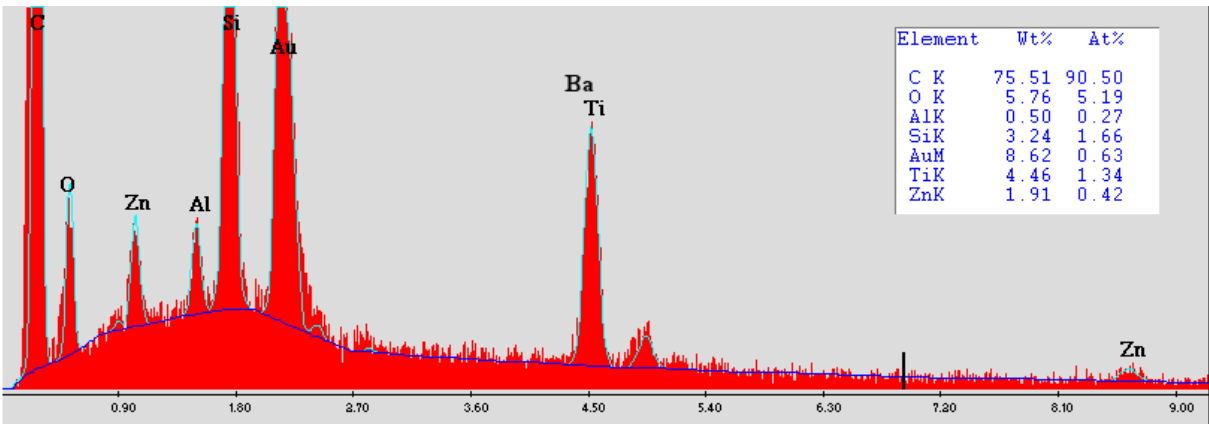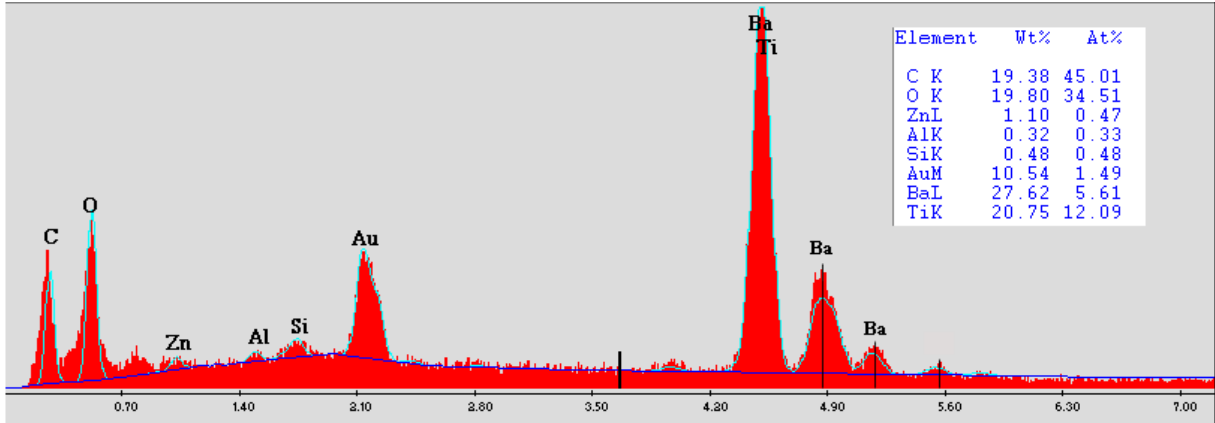
**(c)**

**Figure D-1:** (a) SEM image for termination T-3 stress grading material, (b) EDAX results for termination T-3 stress grading material**,** and (c) EDAX results for particle P-1, shown in T-3 SEM image

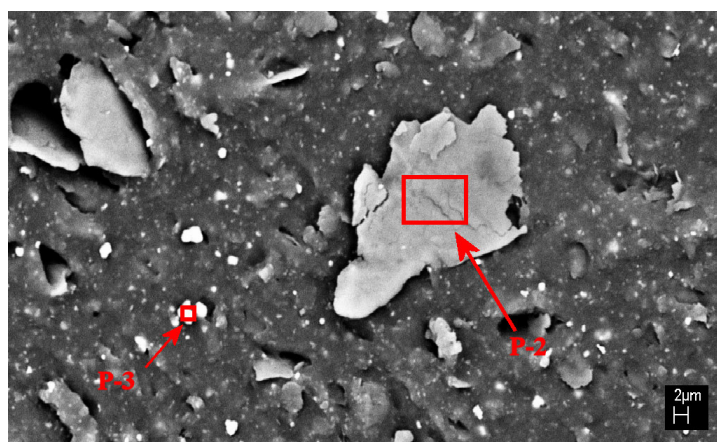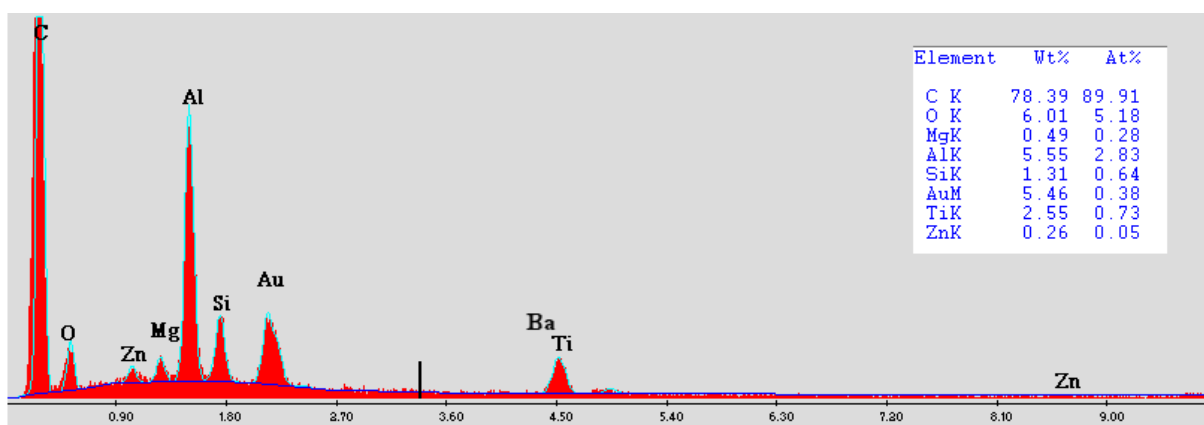The results from Figure D-1 (b) show that carbon is dominant in the T-3 SG material, with minimal silicon present; this suggests that the base material is a hydrocarbon, and may be EPDM.   There is also the possibility that some of the carbon content could be from carbon black fillers, however this cannot be determined from the EDAX results.  The results from Figure D-1 (c) are for particle P-1, one of many similar particles within the SG material. The dominant emission lines clearly belong to either barium and/or titanium.   Since the material is classified as high-permittivity, the particles are very likely barium titanate ($BaTiO_3$), used in SG composites for its high permittivity values and field-dependant permittivity [12,52,53].

## D.2. Characterization of Termination T-4 Stress Grading Material

The results from SEM/EDAX analysis of the termination T-4 grading material are discussed in this section.  The stress grading material of T-4 is comprised of two concentric layers herein referred to as $T4_{inner}$ and $T-4_{outer}$, reported by its manufacturer as having permittivities of 25 and 22, respectively.  The SEM image for $T4_{inner}$ is shown in Figure D-2 (a), and the EDAX results for the whole material, particle P-2, and particle P-3 in Figures D-2 (b), (c), and (d), respectively.  The SEM image for $T4_{outer}$ is shown in Figure D-3 (a), and the EDAX results for the whole material and particle P-4 in Figures D-2 (b) and (c), respectively.

94

**(a)**



**(b)**



**(c)**

| Element | Wt% | At% |
|---------|-------|-------|
| C K | 58.01 | 78.29 |
| O K | 14.11 | 14.30 |
| MgK | 0.31 | 0.21 |
| AlK | 0.54 | 0.32 |
| SiK | 0.53 | 0.31 |
| AuM | 7.57 | 0.62 |
| TiK | 13.85 | 4.69 |
| ZnK | 5.08 | 1.26 |
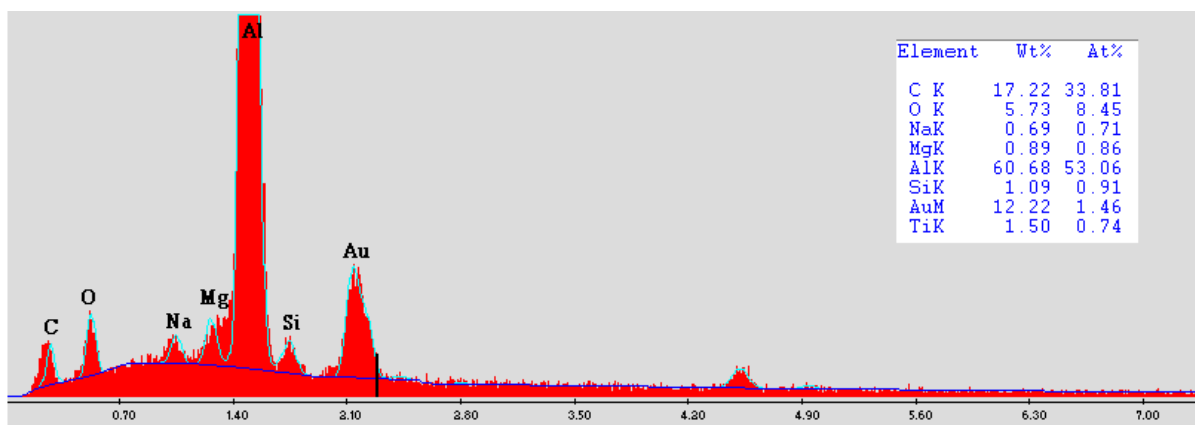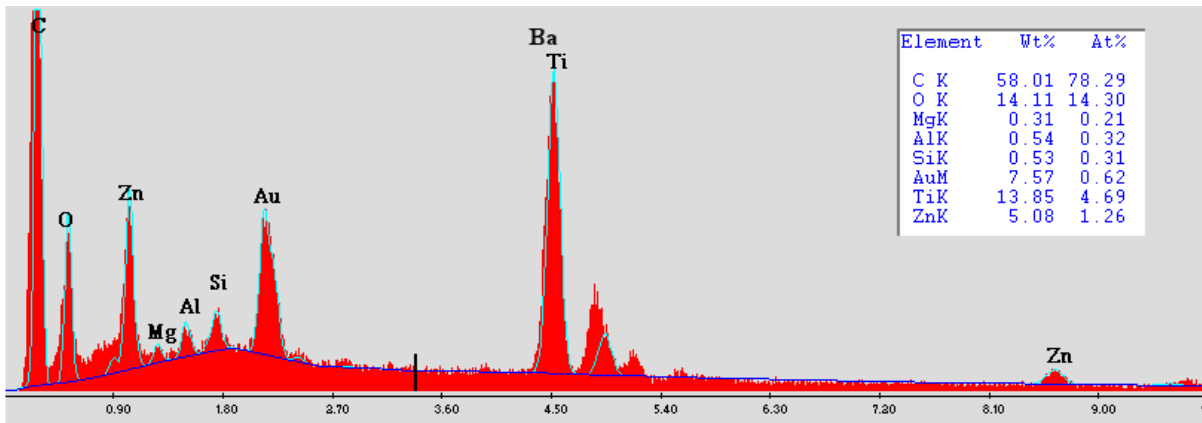
**(d)**

**Figure D-2:** (a) SEM image for T4$_{inner}$ stress grading material, and EDAX results for (b) T4$_{inner}$ stress grading material, (c) Particle P-2 shown in T-4 SEM image, and (d) Particle P-3 shown in T-4 SEM image.



**(a)**



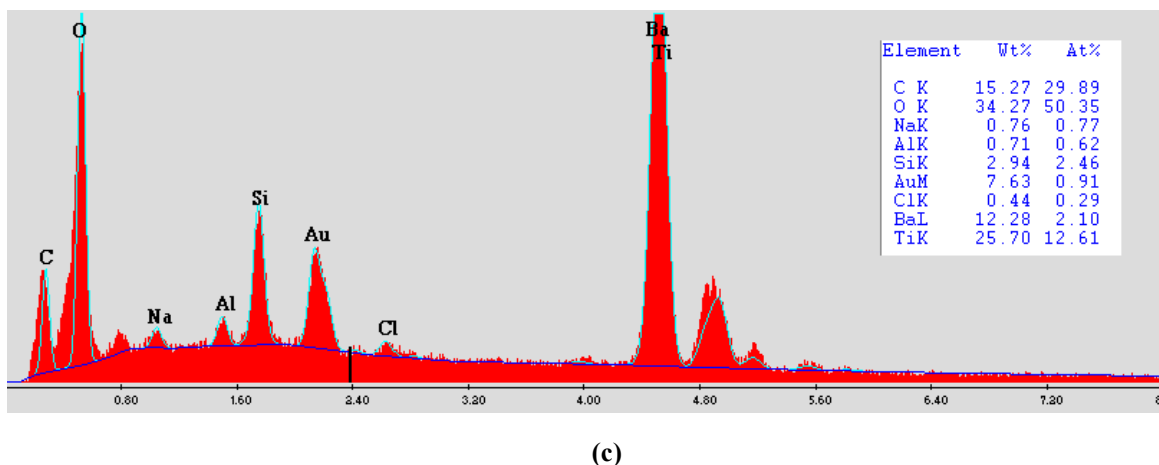| Element | Wt% | At% |
|---------|-------|-------|
| C K | 37.03 | 56.64 |
| O K | 24.65 | 28.30 |
| NaK | 0.15 | 0.12 |
| AlK | 0.43 | 0.29 |
| SiK | 14.96 | 9.78 |
| AuM | 6.76 | 0.63 |
| ClK | 2.04 | 1.06 |
| BaL | 8.71 | 1.16 |
| TiK | 5.26 | 2.02 |

**(b)**

**(c)**
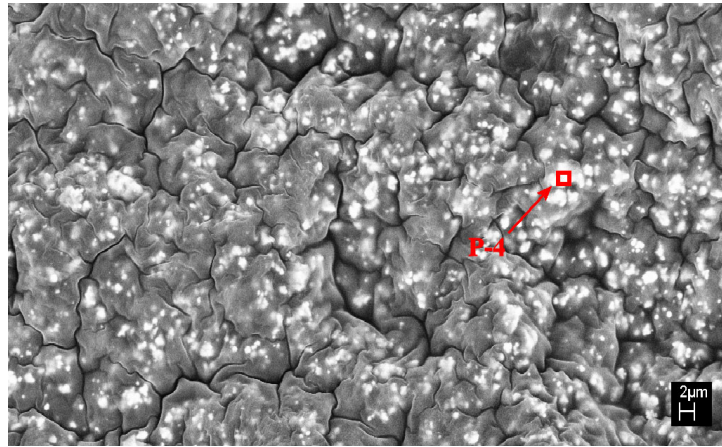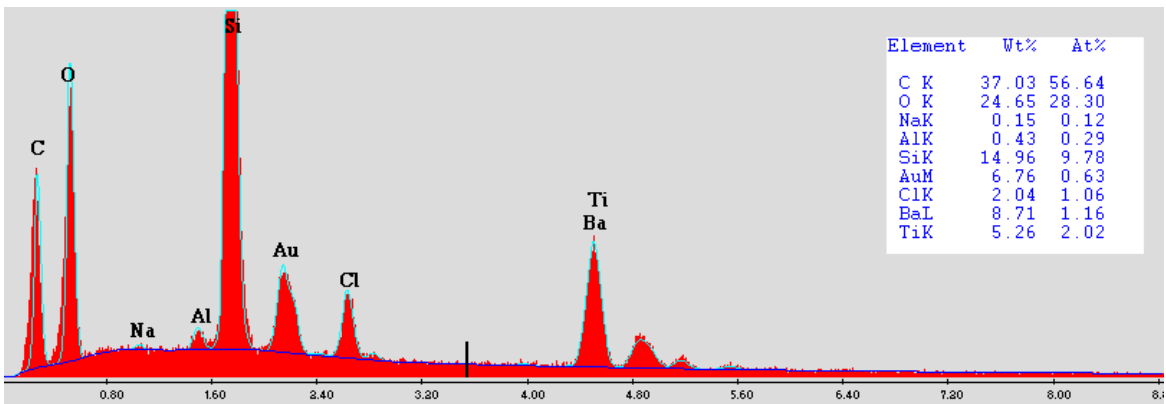
**Figure D-3:** (a) SEM image for T4$_{outer}$ stress grading material, (b) EDAX results for T4$_{outer}$ stress grading material, and (c) EDAX results for particle P-4, shown in T-4 SEM image

The results from Figure D-2 (b) again show that carbon is dominant in the T4$_{inner}$ grading material, with minimal silicon present. As such, it is possible that the polymeric base material is EPDM, and that carbon black filler may be present. The results from Figure D-2 (c) show that particle P-2, one of many with the SG material, is aluminum. Particle P-3 results in Figure D-2 (d) show the presence of barium, titanium, and oxygen, however in less concentration than in termination T-3. The SG layer T4$_{inner}$ thus likely uses aluminum metal fillers added to barium titanate, in order to achieve higher permittivities [12].

The results from Figure D-3 (b) show that although carbon is present in the T4$_{outer}$ grading material, silicon and oxygen are dominant. Thus the composite base material in T4$_{outer}$ is most likely silicon rubber. Figure D-3 (c) shows no presence of aluminum particles in the T-4 outer stress grading layer; however, barium, titanium, and oxygen are present in higher concentration than in T4$_{inner}$. The layer T4$_{outer}$ thus also uses BaTiO$_3$ filler for increasing permittivity; however, the overall refractive effects in termination T-4 arise from the combined relative permittivity between concentric layers T4$_{outer}$ and T4$_{inner}$, as well as the conductive effects of the aluminum filler particles.

# References

[1]     V.K. Sood, HVDC and FACTS Controllers: Applications of Static Converters in Power Systems.  Norwell: Kluwer Academic Publishers, 2004.

[2]     L. Gyugi and  N. Hingorani, Understanding FACTS: Concepts and Technology of Flexible AC Transmission Systems.  New York: IEEE, 2000.

[3]     L. Paulsson, B. Ekehov, S. Halen, T. Larsson, L. Palmqvist, A.-A. Edris, D. Kidd, A.J.F. Keri and B. Mehraban., "High-frequency impacts in a converter-based back-to-back tie; the Eagle Pass installation", IEEE Trans. on Power Delivery, Vol. 18, pp. 1410 – 1415, 2003.

[4]     M. Nagel, T. Leibfried., "Investigation of the high frequency, high voltage insulation properties of mineral transformer-oil", IEEE Conference on Electrical Insulation and Dielectric Phenomena, pp. 226 – 228, 2006.

[5]     F. Guastavino, L. Centurioni, A. Dardano, E. Torello., "Electrical treeing inception and growth in XLPE in presence of harmonics", IEEE International Conference on Solid Dielectrics, 2004.

[6]     H. Suzuki, Y. Ohki, Y. Nakamichi, K.Ajiki., "Water tree characteristics in low-density polyethylene under power-frequency voltages with high-frequency components", IEEE  Conference on Electrical Insulation and Dielectric Phenomena, pp. 742- 745, 1996.

[7]     F.P. Espino-Cortés, "A Study of Field-Dependent Stress Grading Systems Working under Fast Rise Time Pulses", Ph.D. Thesis University of Waterloo, 2007.

[8]     L. Ming, F. Sahlen, S. Halen, G. Brosig, L. Palmqvist., "Impacts of high frequency voltage on Cable-Terminations with Resistive Stressgrading", IEEE International Conference on Solid Dielectrics (ICSD), Vol. 1 pp. 300-301, 2004.

[9]     IEEE 48, "IEEE Standard Test Procedures and Requirements for Alternating-Current Cable Terminations 2.5kV through 765kV", New York: IEEE, 1996.

[10]    B. Taylor, G. Morrison., "Evaluating Medium Voltage Cable Splices and Terminations", IEEE Pulp & Paper Industry Technical Conference, pp. 188 – 194, 2000.

[11]    ABB Data Sheet, Kabeldon terminations for XLPE-insulated cable for extremely high demands.  Alingsås: ABB Kabeldon, 2003.

[12]  E.A. Cherney, "Silicone Rubber Dielectrics Modified by Inorganic fillers for Outdoor High Voltage Insulation Applications", IEEE Trans. On Dielectrics and Electrical Insulation, Vol. 12, pp.1108 – 1115, 2005.

[13]  R. Strobl, W. Haverkamp, G. Malin, F. Fitzgerald, "Evolution of Stress Control Systems in Medium Voltage Cable Accessories", IEEE/PES Transmission and Distribution Conference and Exposition, pp. 843-848, 2001.

[14]  S. Nakamura, K. Saito, G. Sawa, and K. Kitagawa, "Percolation Threshold of Carbon Black-Polyethylene Composites", Japan Journal of App. Phys. Vol. 36, pp. 5163-5168, 1997.

[15]  ABB Data Sheet, It's Time to Connect – Technical Description of HVDC Light Technology.  Ludvika: ABB Power Technologies AB, 2006.

[16]   B. R. Andersen, L. Xu, P.J. Horton, P. Cartwright., "Topologies for VSC Transmission", IEE Power Engineering Journal, Vol. 16, pp. 142-150, 2002.

[17]  L. Xu, V.G. Agelidis, "A VSC Transmission System using Flying Capacitor Multilevel Converters and Selective Harmonic Elimination PWM Control", IEEE Trans. On Power Delivery, Vol. 22,  pp. 693 – 702, 2007.

[18]  K. Temma, F. Ishiguro, N. Toki, I. Iyoda, and J. Paserba, "Clarification and Measurements of High Frequency Harmonic Resonance by a Voltage Sourced Converter", IEEE Trans. On Power Delivery, vol. 20, pp. 450-457, 2005.

[19]  S. Banerjee, "High Frequency Harmonic Resonance in Voltage Sourced Converter Transmission Systems", ECE 663 Term Paper University of Waterloo, 2006.

[20]  S. Meier, "Novel Voltage Source Converter based HVDC Transmission System for Offshore Wind Farms", M.Sc. Thesis Kungl Tekniska Högskolan (KTH), 2005.

[21]  A.H. Bonnett, "Analysis of the Impact of Pulse-Width Modulated Inverter Voltage Waveforms on AC Induction Motors", IEEE Trans. on Industry Applications, Vol. 32, 1996.

[22]  J.C.G. Wheeler, "Effects of converter pulses on the electrical insulation in low and medium voltage motors", IEEE Electrical Insulation Magazine, Vol. 21, pp. 22 – 29, 2005.

[23]  S.U. Haq, S.H. Jayaram, and E.A. Cherney, "Aging Characterization of Medium Voltage Groundwall Insulation Intended for PWM Applications", IEEE Symposium on Electrical Insulation, pp. 143 – 146, 2006.

[24]   F.P. Cortes, E.A.  Cherney, and S.H. Jayaram, "Effectiveness of Stress Grading Coating on Form Wound Stator Coil Groundwall Insulation Under Fast Rise Time Pulse Voltages", IEEE Trans. On Energy Conversion, Vol. 20, pp. 844 – 851, 2005.

[25]   L. Ming, F. Sahlen, S. Halen, G. Brosig, and L. Palmqvist, "Insulation Performance of Cable terminations with Resistive Stress-grading under High Frequency Voltages", XIVth International Symposium on High Voltage Engineering, Paper I-18, pp. 1 – 4, 2005.

[26]   F.P. Cortes, E.A.  Cherney, and S.H. Jayaram, "Stress Grading Materials for Cable Terminations under Fast Rise Time Pulses", IEEE Trans. On Dielectrics and Electrical Insulation, Vol. 13, pp. 430 – 435, 2006.

[27]   M. Nagel, C. Herold, T. Wenzel, and T. Leibfried, "Combined high frequency and high voltage insulation system investigation", IEEE International  Symposium on Electrical Insulation, pp. 440 - 443, 2006.

[28]   M.S. Naidu, High Voltage Engineering.  New York: Mcgraw-Hill, 1999.

[29]   N. Hardt, D. Koenig, "Testing of Insulating Materials at High Frequencies and High Voltage based on the Tesla Transformer Principle", IEEE International Symposium on Electrical Insulation, pp. 517 – 520.

[30]   G.C. Montanari, D. Fabiani, "The Effect of Non-Sinusoidal Voltage on Intrinsic Aging of Cable and Capacitor Insulating Materials", IEEE Trans. On Dielectrics and Electrical Insulation,  Vol. 6, pp. 798 – 802

[31]   IEC 61442, "Test methods for accessories for power cables with rated voltages from 6 kV (Um = 7.2 kV) up to 30 kV (Um = 36 kV).  Geneva: International Electrotechnical Commission, 2001.

[32]   R. Strobl, W. Haverkamp, G. Malin, F. Fitzgerald, "Evolution of Stress Control Systems in Medium Voltage Cable Accessories", IEEE/PES Transmission and Distribution Conference and Exposition, pp. 843-848, 2001.

[33]   Haefely Data Sheet, KEV-50 cable test terminations. Basel: Haefely High Voltage Test, 1997.

[34]   Shell Product Data Sheet, Diala AX lubricants.  Toronto: Shell Canada Limited, 2006.

[35]   Imperial Oil (Esso) Product Data Sheet, Voltesso electrical insulating oils.  Toronto: Imperial Oil Limited, 2003.

[36]   COMSOL Multiphysics AC/DC Module Documentation. Stockholm: COMSOL AB, 2006.

[37]  FLIR SC-500 Infrared Camera, ThermaCAM Researcher Documentation.  Boston: FLIR Systems, 2001.

[38]  PD Detector Type DDX-9101 Operating Manual.  Brewster: Hipotronics, 2003.

[39]  IEC 60502-4, "Test requirements on accessories for cables with rated voltages from 6 kV ($U$m = 7,2 kV) up to 30 kV ($U$m = 36 kV)." Geneva: International Electrotechnical Commission, 2005.

[40]  S.A. Boggs, "Theory of a Field-Limiting Dielectric", IEEE Trans. on Power Delivery, Vol. 9, pp. 1391 – 1397, 1994.

[41]  S.A. Boggs, "Thermal Stability of a Defect-Tolerant Dielectric", IEEE Trans. on Power Delivery, Vol. 9, pp. 1459 – 1465, 2004.

[42]  Z. Zheng and S.A. Boggs, "Defect Tolerance of Solid Dielectric Transmission Class Cable," IEEE Electrical Insulation Magazine, Vol. 21, pp. 35 – 41, 2005.

[43]  S.A. Boggs and J. Kuang, "High Field Effects in Solid Dielectrics", IEEE Electrical Insulation Magazine, Vol. 14, pp. 5 – 12, 1998.

[44]  S.A. Boggs and J.Y. Zhou, "Dielectric Property Measurement of Non-Linear Grading Materials ", IEEE Conference on Electric Insulation and Dielectric Phenomena, pp. 764 – 767, 2000.

[45]  X. Qi, Z. Zheng, S.A. Boggs, "Engineering with Non-Linear Dielectrics," IEEE Electrical Insulation Magazine, Vol. 20, pp. 27 – 34, 2004.

[46]  G. Raju, Dielectrics in Electric Fields.  New York: Marcel Dekker, Inc., 2003.

[47]  A. Helgeson, "Analysis of Dielectric Response Measurement Methods and Dielectric Properties of Resin-Rich Insulation During Processing," Ph.D. Thesis Kungl Tekniska Högskolan (KTH), 2000.

[48]  G.C. Montanari and D. Fabiani, "The Effect of Non-sinusoidal Voltage on Intrinsic Aging of Cable and Capacitor Insulating Materials", IEEE Trans. On Dielectrics and Electrical Insulation, Vol. 6, pp. 798 – 802, 1999.

[49]  L.A. Dissado and J.C. Fothergill, Electrical Breakdown and Degradation in Polymers. London: Peter Peregrinus Ltd., 1992.

[50]  Q. Mu, S. Feng, and G. Diao, "Thermal Conductivity of Silicone Rubber filled with ZnO", Polymer Composites, Wiley InterScience, 2007.

[51]     E. Martensson, B. Nettelblad, U. Gafvert, L. Palmqvist, 'Electrical Properties of Field Grading Materials with Silicon Carbide and Carbon Black", IEEE, 6th International Conference on Conduction and Breakdown in Solid Dielectrics, pp. 548-552, 1998.

[52]     J. Robertson and B.R. Varlow, "Non-linear Ferroelectric Composite Dielectric Materials," IEEE Trans. On Dielectrics and Electrical Insulation, Vol. 12, pp. 779 – 790, 2005.

[53]     J. Robertson and B.R. Varlow, "The Use of Non Linear Permittivity Fillers for the Purposes of Stress Grading within Cables", 7th International Conference on Properties and Applications of Dielectric Materials, 2003.

[54]     B.R. Varlow et. al, "Nonlinear fillers in electrical insulating materials", IET Science Measurement and Technology, Vol. 1,  pp. 96 – 102, 2007.

[55]     Bergoz Current Transformer Data Sheet.  Saint Genis Pouilly: Bergoz Instrumentation, 2006.